

Non-Invasive Reconstruction of Electrical Heart Activity

Looking into your heart



by

Matthijs Cluitmans

MASTER THESIS

**Non-Invasive Reconstruction of Electrical Heart
Activity**

M.J.M. Cluitmans

Master Thesis DKE 10-04

Thesis submitted in partial fulfillment of the requirements
for the degree of Master of Science of Operations Research
at the Department of Knowledge Engineering of the
Maastricht University

Thesis Committee:

Ronald Westra

Jordi Heijman

Ralf Peeters

Paul Volders

Maastricht University
Faculty of Humanities and Sciences
Department of Knowledge Engineering
Operations Research

February 2010

“Imagination is more important than knowledge.”

Albert Einstein

Abstract

Electric heart activity is a major determinant of the functioning of the heart. The inverse problem of electrocardiography tries to reconstruct heart-surface potentials from body-surface potentials, with the use of a patient-specific anatomical geometry. Under well-specified, not too unrealistic conditions, a linear relation between these potentials can be found and methods to obtain this for a specific geometry were implemented. However, the underlying mathematical problem is ill-posed, meaning that little variation in the input data yields considerable, erroneous variations in the solution. To deal with this, two methods were implemented: Tikhonov regularization, and Generalized Minimal Residual (GMRes) regularization.

In several experiments, we describe similar results between the reconstructions of those two methods. Nobody will doubt that the reconstructions are sensitive to geometrical uncertainty, but more severe is the presence of noise. Noise severely reduces the resolution of the reconstruction.

At real-world noise levels, and with the assumptions made, we will have a challenge obtaining useful reconstructions. However, first reconstructions of human heart-surface potentials, based on recordings of body-surface potentials of a test person, show some interesting resemblance with findings described in literature.

Acknowledgements

This thesis could not have developed to its current form without the extensive support of many people. First of all, I would like to thank Ronald Westra, whose everlasting enthusiasm has been a great inspiration. No matter how busy his schedule, Ronald can always find time for his students and has always some compliments available. Jordi Heijman has also been of great help. His thoughts and remarks attributed considerably to this thesis. I look forward working with them in the coming years.

I should also thank Paul Volders for recognizing the power of the imaging technique that forms a central part of this thesis. He also made it possible to obtain the first human body-surface potential measurements, which form the basis of our first human heart-surface reconstructions. I am him and Ralf Peeters grateful for giving me the opportunity to continue this research in the coming years.

To reformulate a popular saying of Ronald, for some people, science is their first and most important love. Therefore, I would like to thank my parents, who have forged this love considerably, and apologize to my girlfriend, who indeed must have felt second at certain times, but never complained.

Contents

Abstract	ii
Acknowledgements	iii
Abbreviations and Terms	vii
Symbols	viii
Preface	x
I General background	1
1 The Heart	3
1.1 The human heart	3
1.2 Electrical conduction	4
1.3 Electrical abnormalities can be lethal	5
1.3.1 Cardiac arrhythmias	6
1.4 Imaging electrical activity	7
2 Electromagnetism	9
2.1 Electromagnetic fields	9
2.2 Self-preservation of electromagnetic waves	10
2.3 Describing electromagnetism	11
II A general Framework for Simultaneous Endocardial and Epicardial Recordings	13
3 The need for a framework	14
3.1 Previous studies of simultaneous endocardial and epicardial recordings . .	16
4 Prerequisites for transmural analysis	17
4.1 Endocardial recordings	17
4.2 Epicardial recordings	18

5	Endocardial recordings	21
5.1	Achievements and problems	22
6	CT as anatomical basis	25
6.1	Achievements and problems	26
6.1.1	Projection of electrocardiographic measurements	28
7	Epicardial recordings	29
III Noninvasive Electrocardiographic Imaging		31
8	The forward and inverse problem of electrocardiography	34
8.1	Formulation of the forward problem	36
8.1.1	Derivation of Laplace's equation with the quasi-static assumption	37
8.1.2	Finding the electrical potential	39
8.1.3	Finding the transfer matrix	44
8.2	Measuring errors	44
9	Data and model description	46
9.1	The concentric spheres model	47
9.2	Eccentric spheres model	48
9.3	ECGsim model	49
9.4	Geometrical and practical issues	49
10	Implementation of the forward method	51
10.1	Finding the coefficients of the transfer matrix	54
10.1.1	Computation of the solid angle	55
10.1.2	Computation of the gradient integral	56
10.2	Implementation	56
11	Validation of the forward implementation	58
11.1	Concentric spheres model	58
11.1.1	Investigation of the scaling defect	60
11.2	Eccentric spheres model	63
11.3	ECGsim model	64
11.4	Conclusion on the validation of the forward method	66
12	Regularization of the inverse problem	69
12.1	The inverse problem is indeed ill-posed	70
12.2	Selected regularization methods	72
12.2.1	Tikhonov regularization	73
12.2.1.1	Applying Tikhonov to our case	74
12.2.2	Generalized minimal residual regularization	75
12.2.2.1	Applying GMRes to our case	77
12.3	The L-curve method for selecting optimal parameters	77
12.3.1	Applying the L-curve method to GMRes regularization	79
12.4	Implementation	81

13 Regularization experiments	82
13.1 Tikhonov reconstructions	82
13.2 GMRes reconstructions	86
13.3 Reasons underlying the inability to reconstruct ECGsim model data . . .	89
13.4 Detection of maxima	90
13.5 Detection of several maxima	93
13.6 Summarizing the first results	95
13.7 Sensitivity to translation errors	97
13.8 Sensitivity to size errors	100
13.9 Sensitivity to noise in the body-surface potentials	102
13.9.1 Significance of these findings	103
13.10 Short summary	105
14 Reconstructions with our own data	106
14.1 Generating body surface potential maps	107
14.2 Tailoring the geometry	108
14.3 Reconstruction of heart-surface potentials	110
14.4 Discussion	116
IV Summary and Conclusions	118
15 Summary	119
16 Conclusions	122
17 Further discussion and future work	124
A Data	126
Bibliography	127

Abbreviations and Terms

cardiac	of the heart
atrium	auxiliary pump of the right or left heart
ventricle	primary pump of the right or left heart
AV node	atrioventricular node of the cardiac conduction system
SA node	sinoatrial node of the cardiac conduction system
epicardial	the outer heart wall
endocardial	the inner heart wall
transmural	through the heart wall
action potential	the change in electric potential in a heart cell that initiates contraction
automaticity	electrical self-excitation of heart cells
arrhythmia	condition with abnormal electrical cardiac activity
ill-posed	the solution to a mathematical problem does not depend continuously on the data
ill-conditioned	the numerical instability of a matrix associated with an ill-posed problem
regularization	using additional constraints to find a solution to an ill-posed problem
CT	Computed Tomography
MRI	Magnetic Resonance Imaging
ECGI	electrocardiographic imaging

Symbols

- Φ electric potential
- Φ_H electric potentials at the outer heart surface (the epicardium)
- Φ_B electric potentials at the body or torso surface
- A the transfer matrix, capturing the geometrical and conductivity relationship between the heart-surface potentials and the body-surface potentials

*To my parents,
for their everlasting support
and for planting a sprout of science in me*

Preface

This thesis is dedicated to our hearts. The human heart is a very fascinating subject; it is for apparent reasons that we associate the heart with life. Without it, we would not be able to exist. But also without electricity, life would not be possible in its current form. The heart pumps due to electrical waves that travel through the heart, initiating contraction and resulting in blood flow.

Therefore, knowledge about the electrical functioning of the heart, provides insight into the state and disease of that heart. Cardiologists have known this for about a century now, but still, the future has a lot to bring. This thesis attempts to give a glimpse of the possibilities that have become available recently. Reconstructing the electrical heart activity from data from electrodes on the body will be the main topic of this research.

This topic, the reconstruction of electrical heart activity, may require some introduction in either heart physiology or the physics of electricity. The first part of this thesis is dedicated to these basics. In the second part, a framework is introduced that explains how we want to investigate electrical heart activity at different levels. The third part is the main piece of this thesis: it explains how we can reconstruct electrical events at the heart surface with measurements from electrical currents at the body surface, and some geometrical information. Experiments will be performed, showing the capacity and limitations of the techniques used. This will come together in the last part, where we provide the main conclusions and discuss some of the future possibilities.

Enjoy reading!

Part I

General background

Introduction to Part 1

This thesis considers a topic that connects several domains of research: medicine, physics and mathematics. Readers might not be familiar with one or more of these subjects, which prevents them from full comprehension of the thesis.

Therefore, this first part provides some general information that is necessary to understand the basic principles that are the foundation of the work performed for this thesis. Feel free to skip any introductory chapters of this first part if you are familiar with their contents.

This thesis starts with a general consideration of the functioning of the human heart, as this is the topic all the mathematical theory is about. Surely, only when we understand what we are imaging exactly, we are able to understand the relevance of what we are doing.

After this physiological introduction, we will dive into the physics of electromagnetism, as this is necessary to understand why some mathematical principles can (and should) be applied to our model of body and heart. Again, full comprehension of the physical background improves understanding of the impact of our actions.

After these introductory chapters, a more detailed approach is possible in the subsequent chapters.

Chapter 1

The Heart

The human heart is a muscle that continuously performs a cycle of contraction and relaxation to fulfill its goal: pumping blood into the circulatory system. A constant flow of blood is required to achieve homeostasis in the human body and is essential to life.

1.1 The human heart

Mechanically speaking, the human heart consists of two separate pumps connected in series: the right heart that pumps blood through the lungs, and the left heart that pumps blood to the other organs. The smaller circulation, that is powered by the right heart, ensures that oxygen is replenished and carbon dioxide is removed in the lungs. This oxygen-rich blood is subsequently pumped by the left heart through the greater circulation: the rest of the body. Here, oxygen is used, fuel is absorbed and put to use, and waste products are generated and removed; all to attain a stable environment (called *homeostasis*) that is needed to sustain life.

Both the left heart pump and the right heart pump can be divided in two compartments: an atrium and a ventricle, see Figure 1.1. Each atrium is a weak auxiliary pump that pumps blood in the larger ventricle, which is the strong primary pump. Both atrial and ventricular muscle contract in much the same way as other (skeletal) human muscles. The primary difference is the duration of contraction: this is prolonged, to allow the pumps to function optimally.

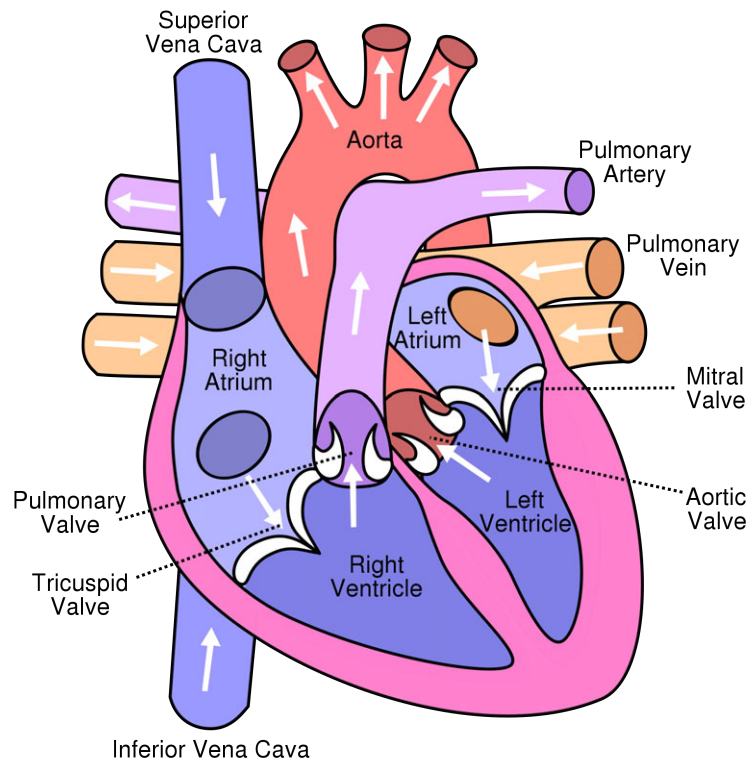


FIGURE 1.1: The structure of the human heart. The heart consists of two separate pumps (left and right), each consisting of an atrium and a ventricle. Blood enters the right atrium and is pumped into the right ventricle. The right ventricle pumps the blood through the lungs and to the left atrium and left ventricle. The left ventricle then pumps the blood through the remaining organs to the left atrium again. (Image taken from Wikimedia Commons)

1.2 Electrical conduction

Contraction of the cardiac muscle is required for the pumping function of the heart: the synchronized shortening of all muscle fibers results in pushing the blood out of the heart cavities. This contraction is initiated by an electrical potential, the *action potential*, that spreads over the cardiac tissue. When this impulse travels over a muscle fiber, the changes in electrical potential over the cell wall induce a cascade of events, in the end leading to fast contraction and slow relaxation of the fiber. Correct timing of the individually contracting and relaxing fibers results in pumping and refilling of the whole heart.

Contraction and relaxation of local cardiac muscle should occur in the correct order. First, the atria should contract to optimally fill the ventricles, and only then the ventricles should contract. On the other hand, all ventricular muscle cells should contract almost simultaneously to achieve optimal performance. Thus, the electrical wave that initiates individual fiber contraction should be delayed between the atria and the ventricles, while within the atria and within the ventricles it should be conducted as fast as

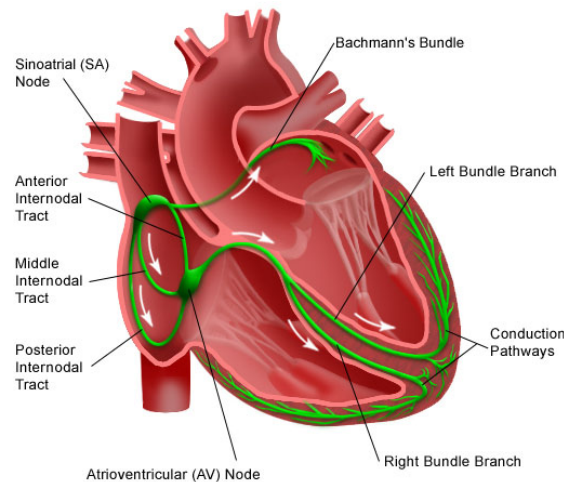


FIGURE 1.2: The electrical conduction system of the heart.

possible. To achieve this, the heart has a specialized conduction system, which is shown in Figure 1.2.

This figure also shows the origin of the electrical wave: the sinoatrial (SA) node or sinus node in the right atrium. This node has an intrinsic frequency at which it generates electrical waves due to self-excitation, for which it needs no input whatsoever - this principle is called *automaticity*. However, the intrinsic frequency at which electrical waves are induced can be influenced by nervous input from the rest of the body, such that the pumping frequency can be adjusted as needed.

When an electrical impulse is generated by the SA node, the conduction system leads the resulting electrical wave at high speed through the atria (both left and right), such that all atrial fibers can contract more or less simultaneously. Then the wave arrives at the atrioventricular (AV) node, at which a necessary delay is induced to allow the ventricles to fill with blood. After this, the left and right bundle branches of Purkinje fibers quickly conduct the wave to all parts of the ventricles, which results in their synchronous contraction and thereby the pumping function of the heart.

1.3 Electrical abnormalities can be lethal

The conduction system as described above is quite reliable: an average person has some billion heart beats during his life, with a failure rate that is exceptionally low. However, erroneous situations do occur, with little or great consequences depending on the exact cause and compensating capacity. Electrical abnormalities in the heart directly influence the functioning of the heart, due to the induction of contraction by electrical waves. For example, the heart could pump less efficient or even stop contracting at all.

An impulse or electrical wave that originates from the SA node at a rate of 60 to 100 beats per minute (bpm) is called *normal sinus rhythm*. When the SA node fails, the AV node, located between the atria and ventricles, can take over at a slower rate, due to the automaticity principle that also (although at a lower rate) is expressed in this cardiac tissue.

However, impulses can also originate from other locations in the heart, for example from a ventricular focus. This can happen since all cardiac cells from the conduction system possess the property of automaticity: self-excitation, by which the cell generates an action potential at its own will. Self-excitation normally only kicks in at rates that are abnormally slow. In this form, self-excitation can take over a failing sinus node or a blocked conduction system.

On the other hand, when an individual cell or group of cells self-excite abnormally, this can result in abnormal origination and dispersion of the electrical wave. Each cardiac cell can transmit impulses in any direction, also in a direction that is opposite to the normal direction when the sinus node fires. Therefore, focal impulses, with corresponding abnormally spreading waves, can result in cardiac disfunctioning. Conditions with abnormal electrical cardiac activity are called *cardiac arrhythmias* and can cause sudden death, syncope, heart failure or have no symptoms at all.

1.3.1 Cardiac arrhythmias

Cardiac arrhythmias are many and complex. Some of the most important ones are discussed briefly here, to stress the need for an imaging modality that is able to show what is happening electrically in the heart.

Electrically speaking, the heart can beat slower than normal (< 60 bpm). This is called *bradycardia* and can have several causes, e.g. *AV block* in which the AV node blocks the incoming electrical impulse. On the other hand, the heart can also beat faster (> 100 bpm), called *tachycardia*, although this can also be a normal situation (e.g. exercising). In abnormal cases, it can be induced by spontaneous focal impulses.

When, due to abnormal automaticity, a part of the heart generates an action potential without being activated by the sinus node, this location is called an *ectopic focus*. Ectopic foci can induce a single premature beat, or, when they fire more rapidly than the sinus node, a sustained abnormal rhythm. This can reduce the efficiency of the pumping mechanism.

Normally, the electrical impulse travels from one side of the heart (top of the atria) to the other side of the heart and then dies out. However, it is possible for an electrical

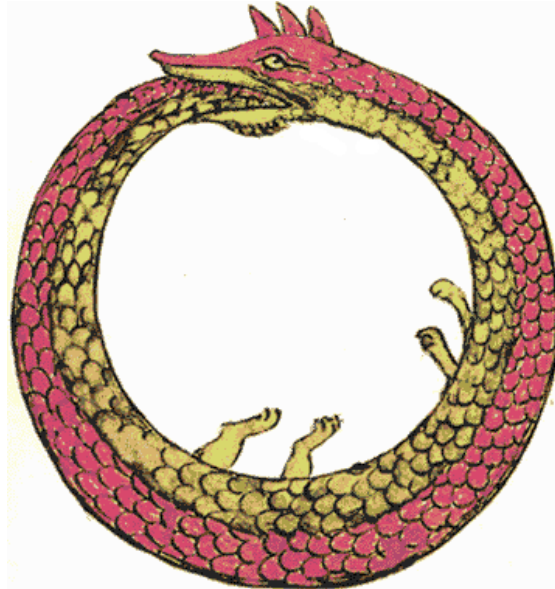


FIGURE 1.3: The Ouroboros: an ancient symbol, representing cyclicality, of a snake swallowing its own tail and forming a circle. A re-entry can be thought of as the same: an electrical impulse travels around some non-excitable tissue and keeps running after its own tail, as long as the tissue in front of it is still excitable.

impulse to travel in tight circles within the heart, as a snake that bites its own tail, see Figure 1.3. This arrhythmia is called *re-entry*, as it allows the impulse to re-enter cardiac tissue that it already visited.

A special case of re-entry is *fibrillation*: an entire atrium or ventricle is involved in continuous, rapid activation by multiple meandering re-entry waves. The atria or ventricles respond electrically, but no coordinated mechanical action is performed: the contraction is local and chaotic, without any synchronization. This greatly reduces the pumping efficiency of the heart. For ventricular fibrillation, the pumping function is compromised to such an extent that this condition is deadly.

1.4 Imaging electrical activity

The above stresses the need for an imaging modality that enables us to assess the electrical functioning of a patient's heart. Many electrical abnormalities in the human heart result in symptoms, some of which can be quite severe, and detailed information about the exact electrical functioning of the heart is essential for a correct diagnosis. Furthermore, fast and accurate imaging of cardiac electrical activity can not only help to provide a diagnosis, but is also a method to evaluate the treatment a patient receives.

Certainly in the western countries, where cardiac disease still is number one in death causes, imaging of cardiac electrical abnormalities can be very helpful. The well known

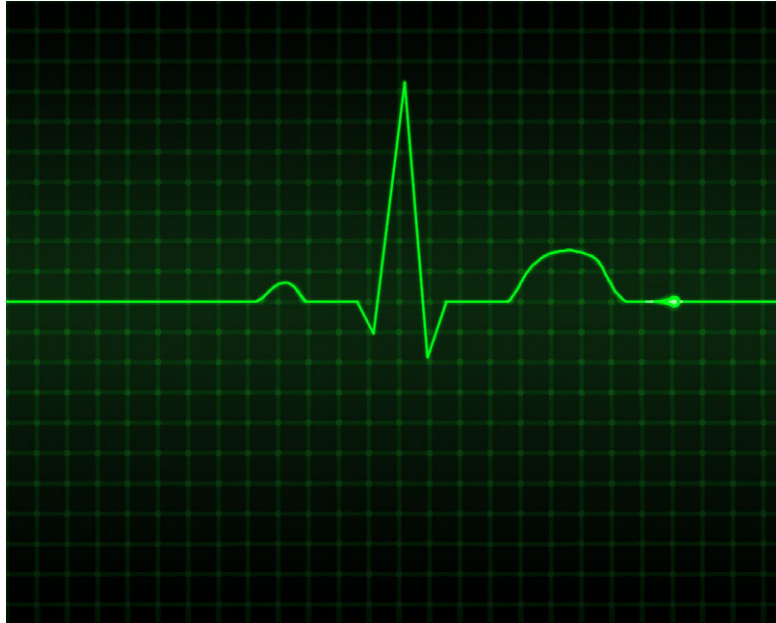


FIGURE 1.4: Schematic representation of an electrocardiogram (ECG).

electrocardiogram (ECG, see Figure 1.4) is extensively used and a powerful starting point to visualize the electrical activity. However, it lacks information that specifies the location of the abnormality in detail. More detailed information can be obtained by intravenous approaches (that is, with a measuring catheter in a patient's vein), but such an invasive approach is often considered too drastic for a possible diagnosis.

To understand how we can construct ECG-like images with just electrodes on the body surface, we first have to introduce some of the physical laws that explain the conduction of electrical currents. The next chapter will provide these basics.

Chapter 2

Electromagnetism

Electricity has existed since the beginning of the universe, but it only became a serious area of research in the beginning of the nineteenth century, when the first practical applications came to use and its impact on society became more and more apparent. The electric engine, for example, provided an alternative for human power and for the bulky steam engines. The comparison between the electric engine and the human heart is not that far off, as both will not function without electromagnetic force.

Although advances in electromagnetism have only been developed in the last few centuries, Chinese documents suggest that magnetism was observed as early as 2000 B.C., and the ancient Greeks already observed electric and magnetic phenomena in 700 B.C. In the early nineteenth century, it was discovered that electricity and magnetism are related and the term electromagnetism was coined. James Clerk Maxwell developed the fundamental laws of electromagnetism, Heinrich Hertz produced electromagnetic waves in his laboratory and quickly new applications were developed that fundamentally changed the world. [1]

2.1 Electromagnetic fields

The electromagnetic field is invisible, just like gravity. Gravity becomes visible when a mass is present in the gravitational field. Since in our daily world, masses are always present and therefore, the gravitational force is apparent at all times. Likewise, we can only see the electromagnetic force when an *electric charge* is present in an electromagnetic field. As gravity is pulling masses to its center, electromagnetic fields pull electric charges in its direction. There is, however, one big difference compared to gravity: there is only one type of mass, which results in “pulling the mass” in a gravitational field.



FIGURE 2.1: Black children playing leapfrog in a Harlem street, ca. 1930. A child jumps over the other children's stooped backs, and when at the first position takes the same pose. An electromagnetic field is like playing leapfrog: a "wave" (kid) dies out by reaching the first position. At that moment, another wave (the kid at the last position) takes over and generates a "new field".

However, electric charges can be either *positive* or *negative*, resulting in either "pulling" or "pushing" the electric charges. This has the important implication that, although charged particles are present everywhere, they often are of opposite kind and therefore often cancel out, without any apparent results on macroscopic level, whereas gravity is always pulling and attracting and thus visible.

2.2 Self-preservation of electromagnetic waves

The electromagnetic field actually consists of two fields: an electric field and a magnetic field. James Clerk Maxwell (1831-1879) had an important understanding of this combination. Each electrically charged particle in the universe is the center of its own electrical field, that spreads out over the whole universe. This field is like a wave: it ripples and spreads out in all directions. Like a water wave, it would die out quickly, if it were not for the fact that *a changing electric field* (i.e. an electric field dying out) *generates a magnetic field*. Thus, the electric field is continued as a magnetic field. But quickly again, this magnetic field is also going to die out. Then something interesting happens: *a changing magnetic field generates an electric field*. As such, the dying magnetic field generates an electrical field again.

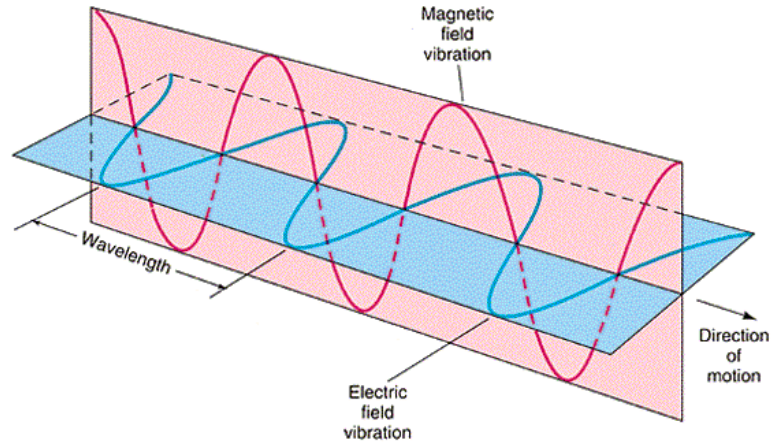


FIGURE 2.2: An electromagnetic field consists of two parts: an electric field (blue) and a magnetic field (red), that travel perpendicular to each other and feed each other with energy.

Thus, the original electrical field switches to a magnetic field, which drives again an electrical field, that dies out and with its death generates a magnetic field and so on and so forth. This goes on for ever, like a row of children playing leapfrog, as in Figure 2.1. The child at the last position jumps over all other children and takes the first position. This snake of children continues to travel forward for ever, if the children would not get bored. Well, electric and magnetic fields do not get bored and will continue their journey into infinity.

Thus, a long story short, electric and magnetic fields continuously feed each other with energy and thus are coupled “in life and death”, hence the name for their alliance: electromagnetism. This is visualized in Figure 2.2.

2.3 Describing electromagnetism

Everything in electromagnetism is contained in the Maxwell equations [2]. These are set of partial differential equations relating electric and magnetic fields to their sources, charge density and current density:

$$\nabla \cdot \bar{E} = \frac{\rho}{\epsilon_0} \quad (2.1)$$

$$\nabla \cdot \bar{B} = 0 \quad (2.2)$$

$$\nabla \times \bar{E} = -\frac{\partial \bar{B}}{\partial t} \quad (2.3)$$

$$c^2 \nabla \times \bar{B} = \frac{\bar{J}}{\epsilon_0} + \frac{\partial \bar{E}}{\partial t} \quad (2.4)$$

The first equation is Gauss' law and describes how an electric field \vec{E} is generated by electrical charges ρ . The second equation is Gauss' law for magnetism, stating that there are no magnetic charges. The third is Faraday's law, describing how a changing magnetic field \vec{B} can induce an electric field \vec{E} . This third law can be seen as "the rules for playing leapfrog", explaining how an electromagnetic field can keep itself alive. The fourth equation is Ampere's law with Maxwell's correction, stating that magnetic fields \vec{B} can be generated by either a changing electric field \vec{E} , or by electrical current \vec{J} .

For this research, we can assume that the electric events can be described independent of time. That is, they are *static*: charges are fixed, or move in a steady flow. This results in a set of simplified equations, the static Maxwell' equations. For electrostatics, these are:

$$\nabla \cdot \vec{E} = \frac{\rho}{\epsilon_0} \quad (2.5)$$

$$\nabla \times \vec{E} = 0 \quad (2.6)$$

These equations will be used in chapter 8, where we find a way to relate electric potentials at the heart to electric potentials at the body surface.

Part II

A general Framework for Simultaneous Endocardial and Epicardial Recordings

Chapter 3

The need for a framework

The introductory part of this thesis informed us about the basic principles of the hearts physiology and about electromagnetism. We saw that the heart pumps out blood due to the mechanical contraction of its muscle fibers. This contraction is initiated by an electrical wave, called the action potential, which originates from a time-triggered firing station in the heart's right atrium. This action potential spreads out over the whole heart and generates an electromagnetic field that can be measured at the body surface with electrodes, resulting in an electrocardiogram (ECG).

In this part of the thesis we will describe the framework that was developed for obtaining information about electrical events within the heart wall. The structure of the heart wall is shown in Figure 3.1. The goal of this framework is to facilitate simultaneous epicardial and endocardial recordings in the human heart. These are simultaneous recordings of electrical activity both at the inner (endocardial) and the outer (epicardial) surface of the heart.

In some syndromes, it might be useful to investigate this transmural electrical conduction from inner heart surface (endocardium) to outer surface (epicardium). For example, in the Brugada syndrome [3], it is suggested that discontinuous transmural conduction is the cause of typical Brugada ECG findings [4], see Figure 3.2. Therefore, a framework that enables the analysis of both endocardial and epicardial recordings can provide insight in hypotheses as these. Especially the analysis of *simultaneous* recordings of epicardial and endocardial electrical properties can be useful.

This part of the thesis describes the development of a software framework for transmural analysis of simultaneous endocardial and epicardial recordings. First, we will focus on previous studies that simultaneously recorded endocardial and epicardial signals in the human heart. Then we will describe how we can obtain endocardial recordings, and

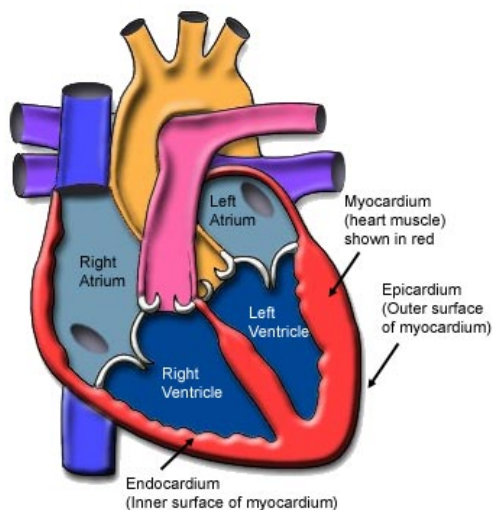


FIGURE 3.1: The structure of the heart. The inner heart wall is called the endocardium, the outer heart wall the epicardium. Electrical waves that initiate contraction travel from endocardium to epicardium.

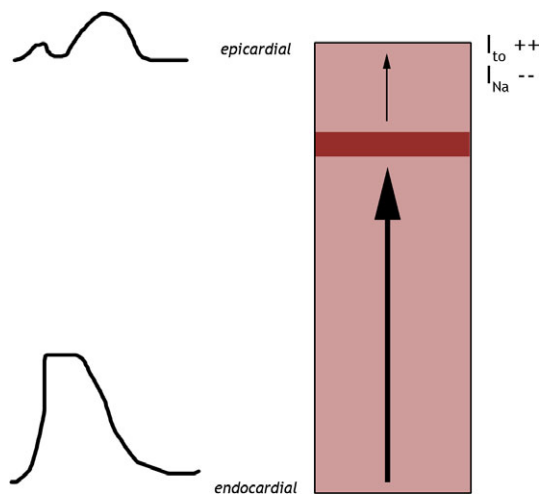


FIGURE 3.2: A theorem suggested by [4], explaining right precordial ST-segment elevation in the Brugada syndrome on the basis of right ventricular transmural gradients of membrane potentials during early repolarization caused by discontinuous conduction, as visualized here.

how computed tomography (CT) can serve as an anatomical basis. Obtaining epicardial recordings is the main focus of this thesis and will be described in a separate part.

3.1 Previous studies of simultaneous endocardial and epicardial recordings

Simultaneous recording of epicardial and endocardial electrical signals in the heart is a complex process. Extensive analysis of simultaneous epicardial and endocardial electrophysiological recordings has rarely been described. One of the first studies that simultaneously recorded epicardial and endocardial electrical signals in humans was published in 1987 by Harris et al. [5].

They investigated the activation sequence of ventricular tissue in patients with ventricular tachycardia. In twenty patients, simultaneous recording of epicardial and endocardial ventricular tissue took place. An endocardial balloon with 110 electrodes was used in the left ventricle, and an epicardial sock with 110 electrodes covered both ventricles. During the procedure, the patients were in cardiopulmonary bypass, experienced ventricular tachycardia and can hardly be said to be in physiological conditions.

Similar studies, that simultaneously record epicardial and endocardial signals in the human heart, are limited. In 1991, Kaltenbrunner et al. [6] published a study in which they analyzed epicardial and left ventricular endocardial isochronal maps in 28 patients with ventricular tachycardia due to myocardial infarction. The epicardial signals were recorded with an epicardial sock (with 64 electrodes) covering both ventricle surfaces. Endocardial recordings were performed with an inflatable balloon (also with 64 electrodes) in the left ventricle only.

The least invasive human study to date is conducted with two new imaging techniques, simultaneously applied in patients by Shannon et al. [7] in 2007. For epicardial recordings, they used the novel technique of Electrocardiographic Imaging (ECGI, discussed extensively in Part 3) to reconstruct epicardial signals from body surface potentials measured with an 80-electrode vest. Endocardial recordings were obtained by noncontact mapping (EnSite). Thus, these conditions are far more physiological than the other studies described above. The recorded endocardial signals were used to validate the reconstructed epicardial signals (during pacing).

Thus, simultaneous endocardial and epicardial recordings have not been performed often. In the next chapters, we will look at the requirements for obtaining such measurements and develop methods to do so.

Chapter 4

Prerequisites for transmural analysis

For analysis of transmural conduction of action potentials, we need:

- endocardial recordings of electrograms (thus, electrical recordings at the inner heart wall)
- epicardial recordings of electrograms (thus, electrical recordings at the outer heart wall)
- information about the anatomical relation between endocardium and epicardium

When we have endocardial and epicardial recordings, and the spatial relation between the recorded points at the endocardium and the epicardium is known, we can investigate changes in conduction that for example occur when sodium channels are compromised.

Figure 4.1 shows our approach for obtaining these endocardial and epicardial electrograms. Endocardial electrograms will be measured with a catheter, while epicardial electrograms will be mathematically reconstructed from recorded body surface potentials.

4.1 Endocardial recordings

For endocardial recordings, the CARTO system can be used. This system, developed by Biosense Webster, uses mapping catheters to intracardially measure electrograms [8]. A catheter is introduced into the heart cavity by intravascular means. The catheter

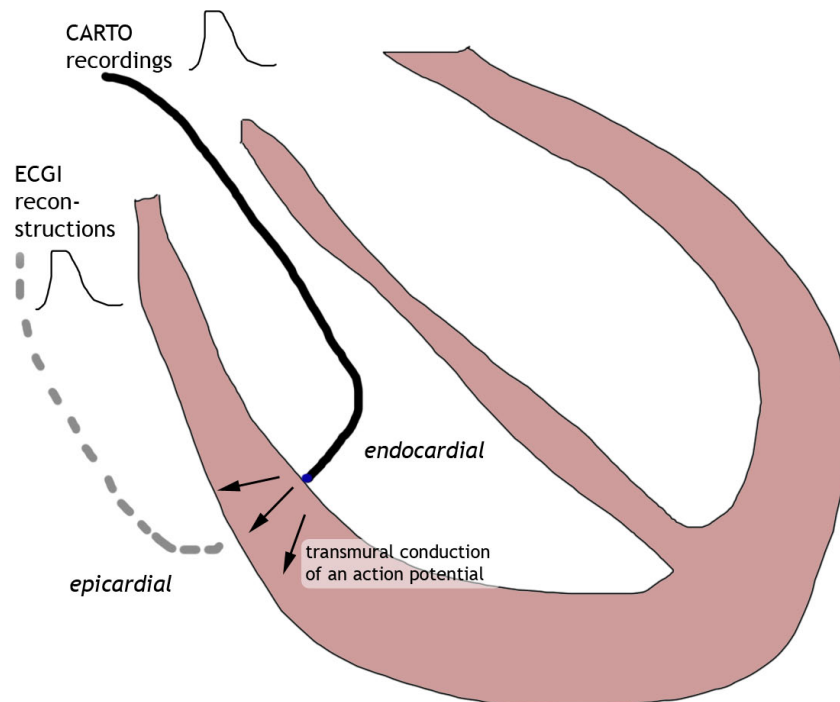


FIGURE 4.1: The Maastricht approach for obtaining simultaneous endocardial and epicardial recordings of electrical heart activity. The endocardial electrograms will be obtained with a recording catheter (the CARTO system), while epicardial electrograms will be reconstructed from measured body surface potentials (ECGI reconstructions).

tip, when pressed against the endocardium, measures electrograms, representing local electrical activity.

The location of the catheter tip is also determined. The tip measures a varying external magnetic field, created by a device placed beneath the patient. This magnetic field has different properties at different spatial locations, such that the location of the catheter can uniquely be determined by measuring the magnetic field at the tip. Since the heart is a dynamical organ, constantly moving during a heartbeat, the location is taken during a relative relaxed period of the heartbeat, usually at the R peak of an ECG. [9]

The combination of local electrograms and their anatomical position allows for an electroanatomical map, which displays the anatomical endocardium (according to the location of the measured points), visually superimposed with electrical properties (according to the measured electrograms) by using color for these values. See Figure 4.2 for an example.

4.2 Epicardial recordings

For epicardial recordings, the novel technique of Electrocardiographic Imaging (ECGI) is used. ECGI uses measurements of body surface potentials and geometric information

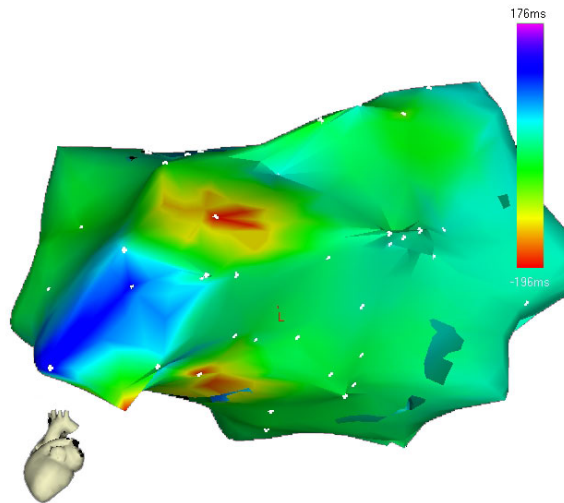


FIGURE 4.2: Electroanatomical map of a left atrium produced by the CARTO system, showing the anatomical structure of the left atrium and the local activation time (LAT) color-coded on top of the structure. The LAT is the time instant at which the underlying tissue is electrically activated.

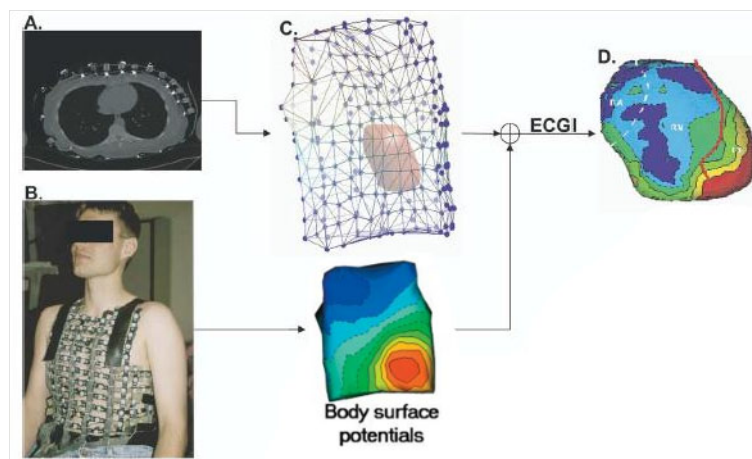


FIGURE 4.3: The ECGI procedure. Body surface potentials are measured with many electrodes, usually 200-300. A Computed Tomography (CT) scan provides geometrical information about the shape and positioning of the heart in the torso. Using the body surface potentials and the geometrical information, ECGI mathematically solves the so called "inverse solution" to reconstruct epicardial electrical potentials.

on the torso and heart shape to solve the inverse solution of electrocardiography, resulting in reconstructed heart surface (epicardial) potentials [10], see Figure 4.3. These reconstructed epicardial potentials than can be used to reconstruct activation maps (isochrones) and electrograms on the epicardium.

The body surface potentials are measured using more electrodes (usually two to three hundred) than in a normal 12-lead ECG, providing a much more detailed recording of the projection of electrical heart activity on the torso surface.

A Computed Tomography (CT) scan provides the anatomical relation between the body

surface and the outer heart surface. This geometrical information is needed to reconstruct the epicardial potentials from the measured body surface potentials. This mathematically complex procedure is the main focus of this thesis and will be described in Part 3. But first, we will look at the endocardial recordings and CT scan in more detail.

Chapter 5

Endocardial recordings

The first step in developing a framework is to acquire endocardial recordings. These data can be measured in patients at the Maastricht University Medical Centre (MUMC+). This hospital routinely uses the CARTO XP system as a diagnostic tool for complex arrhythmias.

The CARTO data can be exported from the CARTO workstation as a list of points. These points were at the time of the procedure accepted by the physician or an assistant as relevant mapping points. Each point has several characteristics, of which the most important are its coordinates (X,Y,Z position) and some relevant electrical measurements as Local Activation Time (i.e. the time an electrical activation wave passed the tissue at that point) and a bipolar and unipolar value.

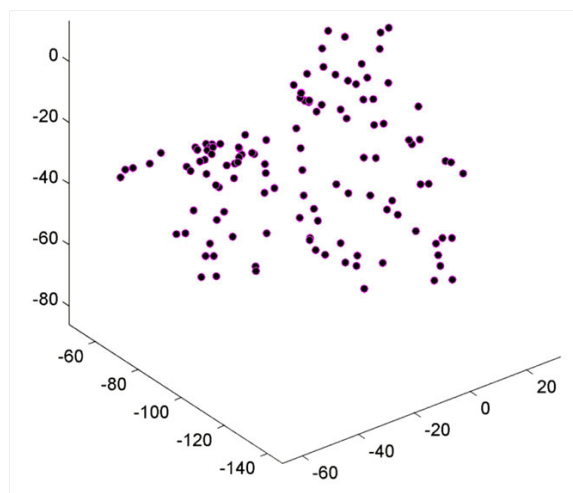


FIGURE 5.1: CARTO points plotted in a three-dimensional space, in this case taken in a left atrium in a human patient.

The first thing that can be done with such a collection of points, is visually represent their location by plotting each point at its correct coordinates in a three-dimensional space, as in Figure 5.1. This view, however, is of little use, as we are not able to mentally visualize the anatomical structure or electrophysiological characteristics of this particular patient's left atrium. However, we know that each point lies at the endocardium, since a point is only registered when the catheter tip is pressed against the inner heart surface and has good electroanatomical contact. Therefore, we can create a surface over all points, representing the endocardium.

Surface reconstruction from a set of points is a difficult issue [11], certainly with as little sample points as generally is the case in CARTO data (typically no more than 200 points are taken during a procedure). We used methods based on an algorithm by Amenta [12]. First, the normals of all points are determined [13]. Then the points and their normals are used as input to a water-tight surface reconstructor [14] or an adaptive moving least squares (AMLS) surface reconstructor [15]. In essence, these algorithms create a triangulation: each point is connected to one or more of its neighbors, such that small triangles between these points are created.

This yields results as shown in Figure 5.2. Now, it is clearer that this is an anatomical structure (in this case a left atrium). However, the above mentioned algorithms sometimes fail to reconstruct correct surfaces, as Figure 5.3 demonstrates. This can be explained by the low number of CARTO points, typically less than 150-200, which makes it hard for surface reconstructors to fit a correct surface. This problem will be addressed and solved further on in this report.

For now, let us assume that we can create a correct surface over (most) CARTO points, as in Figure 5.2. Then it is useful to project the electrophysiological measurements that are associated with each point at this surface. This can be done by coloring the surface, as shown in Figure 5.4. At each point, the surface color represents the value measured at that specific point. At areas between these measured values, an approximated value is determined by linear interpolation between the measured values at surrounding points.

5.1 Achievements and problems

Using the aforementioned techniques, we are able to read points that are created and exported with the CARTO system. These points can be visualized, and a surface can be reconstructed to fit this points as good as possible. Next, coloring the surface visualizes the measured electrical properties of the cardiac structure. Thus, after a CARTO procedure, we are able to handle the CARTO data in our own software environment, with

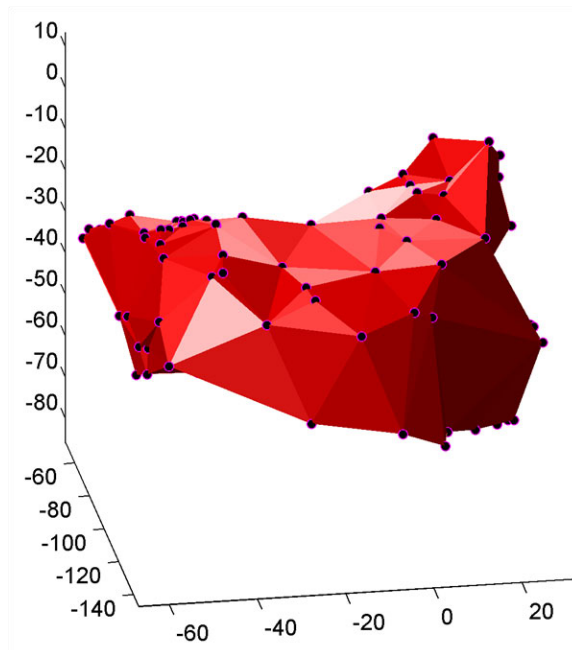


FIGURE 5.2: A reconstructed surface from CARTO points. The CARTO points are blue dots and are the same as in figure 5.1, only from a slightly changed viewpoint. Note that this surface is triangulated: it consists of only triangles between the points.

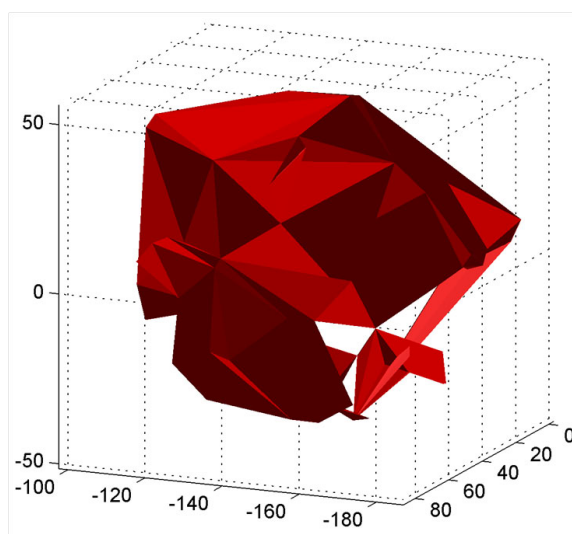


FIGURE 5.3: Surface reconstructed of another set of CARTO points, showing the sometime erroneous reconstruction.

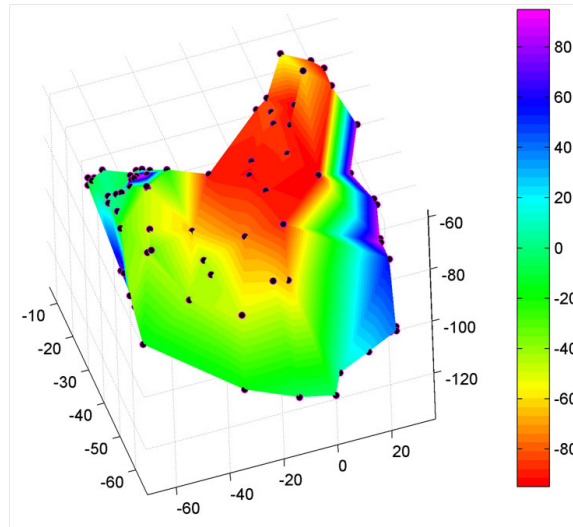


FIGURE 5.4: A colored surface, reconstructed from CARTO points. The coloring represents an electrophysiological measurement, in this case the Local Activation Time (LAT). The LAT represents the time (relative to some chosen reference point in an ECG) that the corresponding tissue is electrically activated. In this figure, the time ranges from about -90ms (red) to approximately +90ms (purple). Thus, the red colored tissue activates first. The activation pattern then spreads via the green and blue colored parts to the purple shaded tissue. In this case, this is a normal activation pattern of a left atrium. The heart's electrical activation front originates in the right atrium, and travels via Bachman's Bundle to the left atrium. This explains the focal entry of the activation front (red) in this left atrium.

algorithms that we choose to use or develop. This gives us great freedom in analyzing data for research purposes, such as the transmural analyses we want to perform after obtaining simultaneous endocardial and epicardial data.

However, there are some problems that require attention. First, the surface reconstruction from the set of points is not always as good as it could be. Also, this surface often lacks detail. It would be very useful to have a more detailed and accurate surface.

Second, there is no information about the relation between all these endocardial data, and the corresponding epicardium. We now know where the endocardium is, thanks to our CARTO points and the associated endocardial surface, but there is no information about the epicardial structure. The local wall thickness and exact positioning of the epicardium relative to the endocardium are unknown.

Both these problems can be solved by means of a CT image. By using a CT image, we can reconstruct an accurate endocardial surface, that has much more detail than our reconstructed CARTO surfaces. Furthermore, from the same CT image, an epicardial surface can be reconstructed. This means that with one medium, we can extract both surfaces that are required, which ensures a great anatomical correlation between the two reconstructed structures. Wall thickness and relative positioning can then be extracted quite precisely. The next section describes the use of CT scans to achieve these goals.

Chapter 6

CT as anatomical basis

The advantage of using a Computed Tomography (CT) scan as anatomical reference is the availability of existing algorithms that are able to reconstruct endocardial and epicardial heart surfaces from one scan. This allows for detailed anatomical reconstruction of these surfaces, with much higher spatial resolution than the surfaces reconstructed from CARTO points.

Another advantage of using a CT scan is the good correlation between the endocardial and epicardial surface. That is, by using one medium, accurate estimates of the positioning of the endocardium relative to the epicardium, as well as of the local wall thickness, can be made. These properties are very important when analyzing endocardial and epicardial recordings, since the local endocardial electrograms have to be matched to the corresponding (i.e., the closest) epicardial electrograms. On top of that, wall thickness probably has a significant influence on conduction of the action potential in for example the Brugada syndrome [4].

For this purpose, cardiac multislice CTs are used. Software is readily available to segment the endocardium and epicardium from these CT scans. Endocardial surface reconstruction is routinely performed at this hospital, and also epicardial surface reconstruction (although more cumbersome) is possible. After the construction of both surfaces, these can be imported into our software framework.

Our framework then allows for visualization of the surfaces. For example, Figure 6.1 shows two endocardial surfaces: a left ventricle and a corresponding left atrium. It can be seen that the spatial resolution of these surfaces is much higher than the resolution of the surface reconstructed from CARTO points.

Figure 6.2 shows the endocardial surface of a left ventricle within the epicardial surface of the whole heart. This projection shows the relative positioning of the endocardium

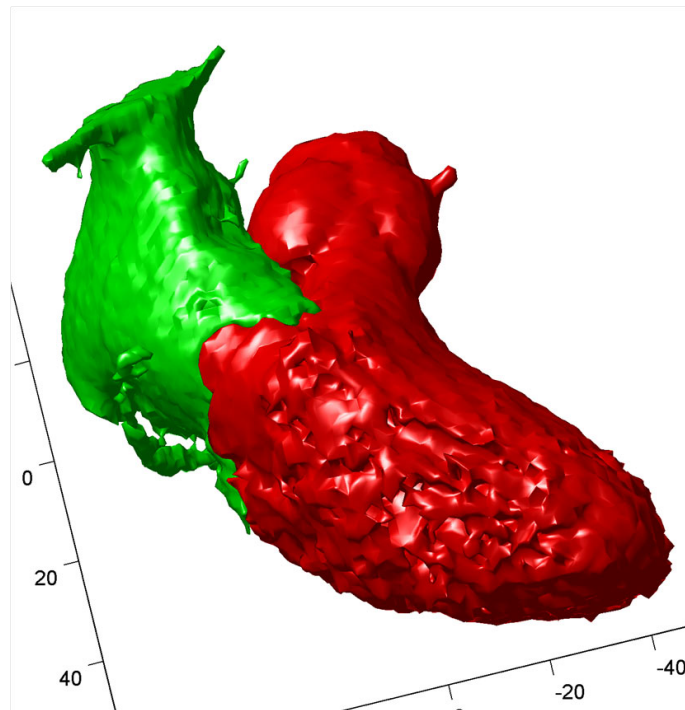


FIGURE 6.1: Reconstructed endocardial surfaces of the left ventricle (red) and left atrium (green) of a patient, reconstructed from a cardiac multislice CT scan. Note that both surfaces are endocardial.

of the left ventricle in the surrounding epicardial structure. High correlation is ensured by using one medium for reconstruction of both surfaces.

Additional functionality of the tool we developed allows visualization of cross-sections through the heart, as shown in Figure 6.3. These allow for easy visualization of wall thickness and positioning of endocardium relative to epicardium.

6.1 Achievements and problems

As described, our framework enables importing surfaces that are segmented from a cardiac CT scan using existing software. These surfaces (whether endocardial, epicardial or both) can be used as anatomical basis for analysis of electrophysiological measurements. By using our custom-made framework, great freedom in implementing mathematical algorithms is ensured.

However, several problems that need further consideration have arisen. First of all, although endocardial segmentation is routinely performed at our hospital, epicardial reconstruction is more complex. When segmenting epicardial structures, pericardial structures and surrounding tissue are quite easily merged with the epicardium. The epicardium then has to be cut free of the non-epicardial structures, which is a difficult

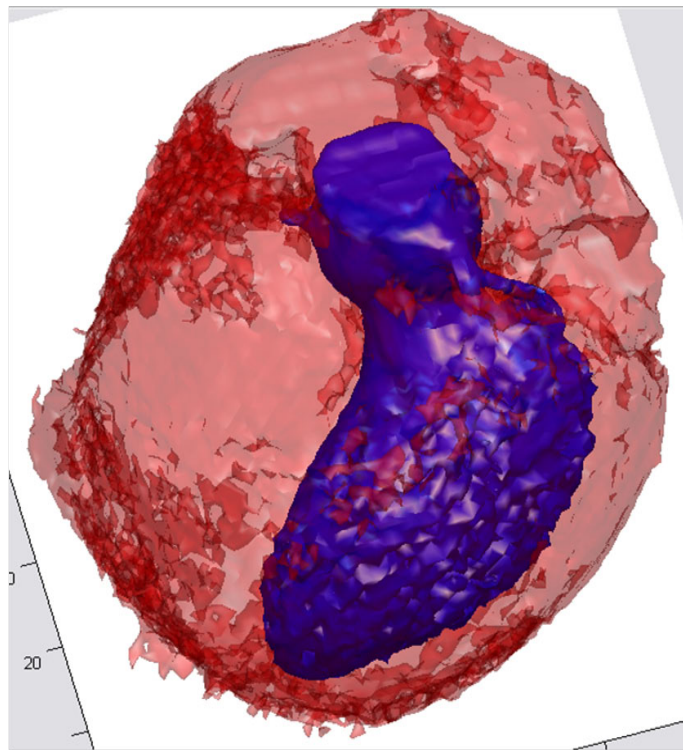


FIGURE 6.2: A reconstructed endocardial surface of the left ventricle (blue) projected within the reconstructed epicardial (red) surface of the whole heart. Both surfaces are reconstructed from a cardiac multislice CT scan.

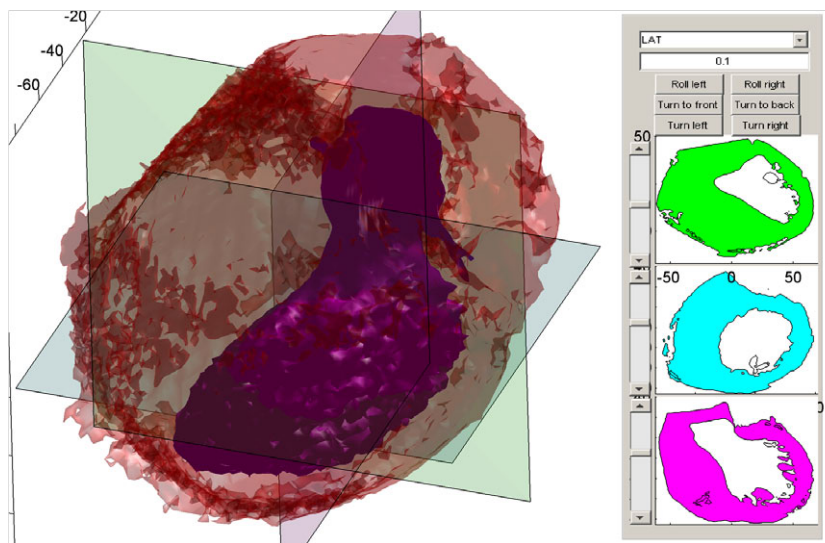


FIGURE 6.3: A reconstructed endocardial surface of the left ventricle (blue) projected within the reconstructed epicardial (red) surface of the whole heart. Superimposed are slices that visualize cross-sections. The panels on the right show the corresponding cross-section. The inner contour on such cross-section represents the endocardium (in this case of the left ventricle only), while the outer contour represents the epicardium of the whole heart. Note that the filled area between those contours actually also contains other blood filled volumes, such as the left and right atria and the right ventricle. These are omitted in this view. Note also that the ventricular wall thickness can easily be measured, and that structures as detailed as papillary muscles are visible.

process in which "wishful cutting" can easily produce faulty results. This issue can probably be controlled by experimenting more with segmenting epicardial structures and gaining experience in this field.

6.1.1 Projection of electrocardiographic measurements

Another issue that needs to be solved is the projection of electrocardiographic measurements (e.g. the values measured with CARTO) onto the reconstructed endocardial or epicardial surface. When using CARTO points as basis for surface reconstruction, each vertex of the triangulated surface had a measured electrophysiological value. When using the CT-reconstructed surfaces, however, we have many more vertices (typically many thousands) for each triangulated surface than was the case with CARTO (typically less than two hundred). We therefore have to project the few measured CARTO values onto the many CT-reconstructed vertices.

One approach to achieve this is as follows: for each CARTO point, find the closest CT-reconstructed vertex and assign that vertex the corresponding CARTO value. Next, for each vertex with a value assigned, find the closest non-valued vertex and the closest vertex with an assigned value that has the non-valued vertex on its geodesic line (shortest path) with the first vertex. Then, linearly interpolate all points between the two (value assigned) vertices. This process is described in [16]. It is, however, a computationally very demanding process, certainly when the number of vertices is some tens of thousands.

Therefore, a less demanding algorithm has to be developed. Approximation or linear interpolation should be applicable, although we have to adapt the existing 1D algorithms to our two-dimensional surface in three dimensions.

To correctly project the CARTO point data onto the segmented CT surface, we need an anatomical reference in both the CT-reconstructed surface and the CARTO data, to anatomically align both data sets. Image integration of electroanatomical mapping (such as CARTO) with CT/MRI imaging has been shown to be feasible [17]. It has been shown that the pulmonary veins entering the left atrium can be such an anatomical reference location, but also the descending aorta can serve as a good reference point.

Chapter 7

Epicardial recordings

Now we have a good anatomical basis and have endocardial recordings, the next step is to implement the analysis of epicardial recordings. These recordings will be obtained by solving the so called inverse problem of electrocardiography.

Standard electrocardiographic imaging techniques infer information about the cardiac electrical activity from electrocardiograms (ECGs) recorded on the body surface, far away from the heart. These methods are limited in their ability to detect and localize electrophysiological processes in the heart. Increasing the number of measured ECGs on the body surface from twelve (as in the default twelve lead ECG) to several hundreds provides more detailed information in the form of body surface potential maps (BSPM). These BSPMs contain more detailed information than the standard ECG, but still provide a very low-resolution projection of cardiac electrical processes, due to the smoothing effect of the torso volume conductor. On top of that, each body surface ECG incorporates the electrical activity of the whole heart, thereby rendering exact location of electrical processes in the heart more difficult. In contrast, measurements directly on the heart surface provide a high-resolution representation of electrical heart activity, with accurate localization. The novel method of electrocardiographic imaging (ECGI) is able to reconstruct this electrical heart activity on the outer heart surface in a non-invasive way. ECGI reconstructs epicardial electrograms from body surface potential measurements, thereby obtaining local information about cardiac events. [18]

To perform reconstruction of epicardial electrograms as done in ECGI, we need a CT scan and body surface potentials. These body surface potentials are measured with 256 electrodes attached to the body surface. The measured body surface potentials are the result of electrical heart activity (and perhaps some interfering electrical sources like other muscles). The so called *inverse solution of electrocardiography* uses these body surface potentials to mathematically reconstruct the associated epicardial potentials

(and the corresponding electrograms), as described in [19]. This method is developed and validated by Rudy and others [10, 20–22] and is routinely applied in their lab.

The remaining part of this thesis is dedicated to the problem of obtaining epicardial recordings by means of solving the inverse problem of electrocardiography.

Part III

Noninvasive Electrocardiographic Imaging

Introduction to Part 3

In the previous chapters we saw why it is important to obtain heart-surface potentials in patients. Obtaining these is not easy. One way is open heart surgery, but this is a very invasive and severe procedure. A non-invasive method would be preferable, and one possible way is reconstructing heart-surface potentials from many measurements of potentials at the body surface. However, mathematically and technically, this is quite a challenge.

That means that we have arrived at the major topic of this research: the reconstruction of heart-surface potentials from body-surface potentials. The idea behind our approach is illustrated in Figure 7.1. We start with a patient, of whom we take computed tomography images to obtain a geometrical relation between his heart and torso. We also take many, typically 256, recordings of body-surface potentials. These are aligned with the obtained geometry, such that we have a nice view of the potentials distributed at

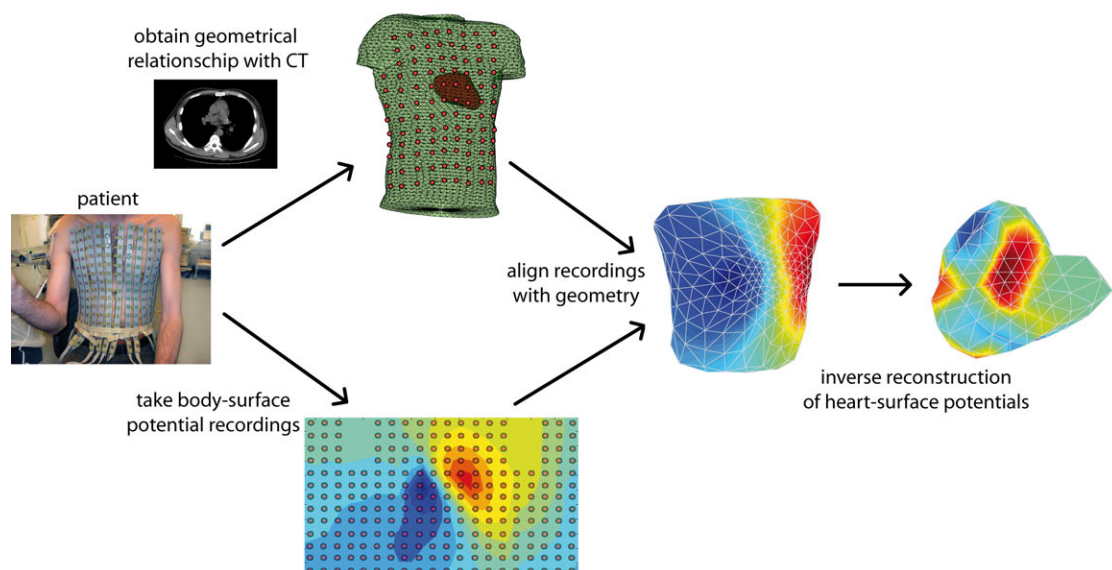


FIGURE 7.1: Our procedure for obtaining inverse reconstructions of human heart-surface potentials.

the body-surface. Next, we can try to mathematically reconstruct the corresponding heart-surface potentials.

For this, we need to derive a method for relating heart-surface potentials to body-surface potentials. We will also look at the inverse of this problem, and discover that it is ill-posed. In order to obtain realistic solutions, regularization techniques are required. Many experiments are performed to validate our implementation and the characteristics of the methods used.

Chapter 8

The forward and inverse problem of electrocardiography

As we have seen in earlier introductory chapters, electrical currents flow through the heart, initiating contraction of the heart muscle. Electrical currents generate an electromagnetic field, which spreads throughout the body and results in potentials at the body surface. In that sense, electrical activity of the heart is reflected at the body surface. This fact has been recognized for more than a century now, starting with the development of the electrocardiogram (ECG) by Willem Einthoven. An extensive knowledge base has been build around ECGs, but they do lack the capacity to localize events on the heart surface. Current diagnoses based on ECG are based more on empirical pattern recognition than on biophysical modeling [23].

Ultimately, the goal of electrocardiography would be to describe the electrochemical activity of each cell in the heart, based on body-surface electrocardiograms. Of course, this goal still is far way, if not utopian, but we can certainly improve on the ECGs used in everyday practice. To do this, we must find an answer to the question: how do electrical currents on the heart generate body-surface potentials? This is the so called *forward problem of electrocardiography* and has been a subject of research for a long time.

If we want to figure out how to investigate electrical activity on the heart, we first need a way to represent this electrical activity. A good way is to use heart-surface potentials, by which we mean the electrical potentials at the outer surface of the heart (i.e., potentials at the *epicardium*). These heart-surface potentials of course reflect the heart activity quite well, as they directly reflect the action potential traveling through the heart.

Thus, to make the forward problem more concrete, we want to relate heart-surface potentials to body-surface potentials. We will see that we are able to find a linear relation between those, in the form of

$$\Phi_B = A\Phi_H \quad (8.1)$$

where Φ_B represents the vector of body-surface potentials, Φ_H the vector of heart-surface potentials, and A the geometry and conductivity transfer matrix reflecting the properties of the volume conductor between the epicardial surface (that is, the outer heart surface) and the body surface. In other words, Φ_B contains the potentials at various locations at the body surface, and Φ_H those at the outer heart surface, and the matrix A somehow describes the relation between those two sets of potentials.

The forward problem can now be reformulated as: how do we find the transfer matrix A for a certain situation? We will derive methods to determine this transfer matrix in the following section and we will see that this transfer matrix, under some well-specified conditions, indeed only depends on the geometry of heart and torso. In other words, if we know the position and shape of the heart and body surface, and make some accompanying assumptions, we can determine the transfer matrix A and compute body-surface potentials from given heart-surface potentials.

If we have reached this state, we have solved the forward problem of electrocardiography. However, in real life, we will not have the desire to calculate body-surface potentials from heart-surface potentials. In fact, we want to do the opposite, as this is medically much more relevant: we want to reconstruct heart-surface potentials from body-surface potentials. Indeed, the heart-surface potentials can inform cardiologists in detail about the functioning and disfunctioning of the heart, and we can much more easily obtain body-surface potentials than direct heart-surface potentials. For the latter, we would need open heart surgery and place electrodes on the heart surface, methods too drastic for almost all cases.

The problem of reconstructing heart-surface potentials from body-surface potentials is called the *inverse problem of electrocardiography*, as it is exactly the opposite of the forward problem. This could be done by inverting the transfer matrix A to obtain the following relation:

$$\Phi_H = A^{-1}\Phi_B \quad (8.2)$$

After all, if A specifies the relation from heart- to body-surface potentials, then its inverse, denoted A^{-1} , would give the relation from body- to heart-surface potentials according to formula 8.2.

The problem is not so much inverting A , but reducing the influence of noise. The inverse problem of electrocardiography is so called “ill-posed”. This means that little disturbances in measurement data will yield unconstrained errors in the solution, thereby making the solution useless. Since noise is always present in real world measurements, its influence should somehow be controlled or *regularized*. Equation 8.2 will therefore not be sufficient to get reliable heart potentials. The regularization methods we used to obtain a realistic solution are discussed in chapter 12.

The ill-posed character of the inverse problem results from attenuation (due to dispersion) and smoothing (due to spatial superposition) of the electrical fields between the heart surface and body surface [23]. Reconstruction of heart-surface potentials thus should involve amplification and unsmoothing. When applied to real-world measurements, in which noise is always present, the resulting solution can be erroneous in a large, nonlinear and even discontinuous way [23].

8.1 Formulation of the forward problem

But first back to the forward problem. The forward problem of electrocardiography tries to specify the electrical relation from the heart to the body surface. One formulation of the problem represents the actual intra-cardiac sources in terms of the distribution of electrical potential on a closed surface that completely contains the electrical sources of the heart [23]. Or, in other words, the epicardial surface S_H contains all bioelectric sources in the heart region H . The field on any other enclosing surface (such as the body surface S_B) has, in principle, a one-to-one relation with the potential distribution on the inner (epicardial) surface. Thus, we can relate the potentials at the heart surface S_H with a body surface S_B , assuming that the medium in between is homogeneous, as in Figure 8.1. This homogeneous assumption can be eliminated, but research has shown that it does not make a lot of difference in the end [24].

Let’s define the potentials at n locations at the heart surface as $\Phi_H = (\Phi_H^1, \Phi_H^2, \dots, \Phi_H^n)$ and the potentials at m locations at the body surface as $\Phi_B = (\Phi_B^1, \Phi_B^2, \dots, \Phi_B^m)$, then our goal is to find a transfer matrix A such that $\Phi_B = A\Phi_H$.

The equations needed to calculate the potential distribution within volume V , the homogeneous and source-free volume between S_H and S_B , are Maxwell’s equations, mentioned in chapter 2. However, the human torso has the following properties [25]:

- The highest significant frequency in bioelectrical systems is approximately 1 kHz;
- There are nearly no magnetic materials in the thoracic region;

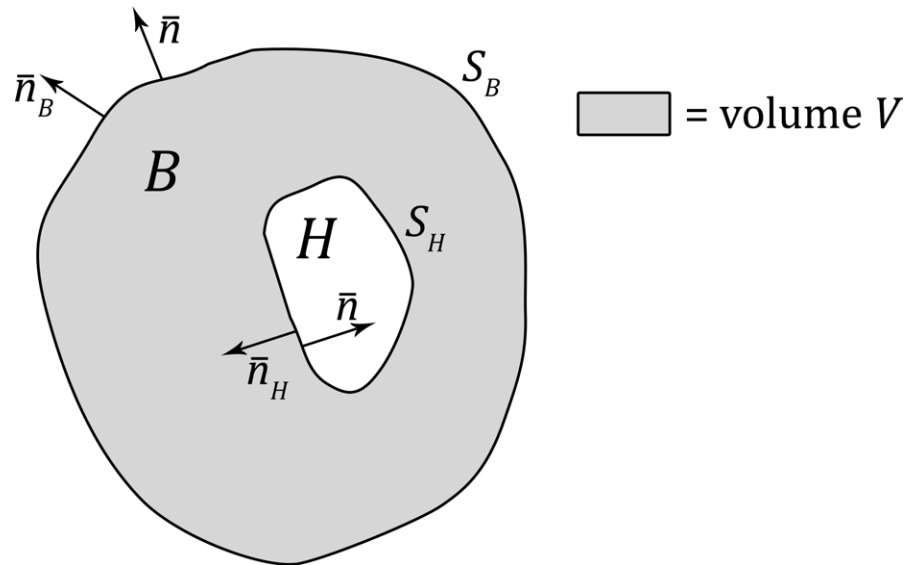


FIGURE 8.1: A schematic torso B and heart H , with corresponding surfaces S_B and S_H , and their normals n_B and n_H . The heart contains all bioelectrical sources, thus the volume between S_B and S_H is source-free.

- The conductivities of blood, lung, fat and muscle tissue range from 0.0004 to 0.006 siemens/cm, while a typical body has an approximated size of 1 meter.

These properties allow us to make the following assumptions:

- Gross capacitive effects in the human torso are negligible, that is, no electrical charges are stored and the medium is essentially resistive;
- Gross inductive effects are also negligible. In other words, there is a potential field due to changing magnetic fields;
- Boundary conditions reduce to those of static electric fields;
- And propagation effects are negligible.

That means, that these electromagnetic fields are *quasi-static*, which allows us to simplify our model.

8.1.1 Derivation of Laplace's equation with the quasi-static assumption

When currents flow through a volume conductor, this implies the presence of an electric field \vec{E} , as electrical fields move charges, and the definition of current involves moving charges (see chapter 2). In the human body, time-varying conditions can be broken

down at each time instant, and \bar{E} will behave static at each instant of time. This is called *quasi-static*, and the result is that we can apply the static version of Maxwell's equation describing an electrical field: $\nabla \times \bar{E} = 0$ (see equation 2.6). This means that we can describe \bar{E} from the negative gradient of a scalar potential Φ , that is [26–28]:

$$\bar{E} = -\nabla\Phi \quad (8.3)$$

The presence of an electric field means that any charge in this field has a force working on it. In a conducting medium, such as our volume V , this means that an electric field results in the flow of charge, that is, it results in a current. The current density \bar{J} is related to the electric field \bar{E} by Ohm's law:

$$\bar{J} = \sigma\bar{E} \quad (8.4)$$

in which σ is the conductivity of the volume conductor (expressing how easy charge can flow through the medium). When we assume, as here, that the conductivity is identical in all directions, σ is a scalar and consequently, the current density \bar{J} is directed in the same direction as the electric field \bar{E} . That is, current will flow in the direction of the electric field. Then, substituting equation 8.3 into 8.4 yields:

$$\bar{J} = -\sigma\nabla\Phi \quad (8.5)$$

Since our homogeneous volume V is source-free (all electrical sources lie within H and not V), conservation of current requires that:

$$\nabla \cdot \bar{J} = 0 \quad (8.6)$$

Due to 8.5, $\nabla \cdot \bar{J} = -\sigma\nabla^2\Phi$, and combining this with 8.6 yields:

$$-\sigma\nabla^2\Phi = 0 \quad (8.7)$$

Since $\sigma \neq 0$, this yields the following result:

$$\nabla^2\Phi = 0 \text{ in volume } V \quad (8.8)$$

This equation is called *Laplace's equation*.

Laplace's equation is accompanied by some boundary conditions. These are applied to the body surface and result from the assumption that the air surrounding the body has zero conductivity [26]. The resulting "zero normal flux" boundary condition states that

the potential field will not change when leaving the body surface and can be written as:

$$(\sigma \nabla \Phi) \cdot \bar{n}_B = 0 \text{ on body surface } S_B \quad (8.9)$$

with \bar{n}_B a unit vector outwardly normal to the body surface.

Together, equation 8.8 for the source-free body volume V and equation 8.9 for the body surface constitute the boundary-value problem for electrocardiography. This problem can be solved for an arbitrarily shaped volume conductor only by means of numerical computation, using either the finite element method or the boundary element method [29].

The finite element method (FEM) is based on minimizing an energy function within the volume. The volume itself is discretized into tetrahedral (or similar) shapes. The electric potential can then be expressed as a sum of piecewise continuous polynomial functions. The finite element method can be very useful, but it has some disadvantages compared to the boundary element method (BEM). In the BEM, only the boundary surface is discretized, often into triangles. Again, each triangle (or similar element) is associated with piecewise polynomial basis functions. A great computational advantage of BEM is that, as only boundaries are discretized, much fewer elements are needed to represent the same geometry as with FEM. Furthermore, with BEM, a geometry can be adapted more easily as only the boundary elements have to be relocated, while in FEM all elements in the volume have to be relocated. For these reasons, the boundary element method is the method of choice to solve Laplace's equation.

Application of either method to the potential fields in the torso volume conductor results in a set of simultaneous linear equations, relating the body-surface elements to the heart-surface elements. The final form for the numerical solution to Laplace's equation is the earlier stated equation:

$$\Phi_B = A\Phi_H \quad (8.10)$$

and will be derived in the following sections.

8.1.2 Finding the electrical potential

Now, with the model of Figure 8.1, we want to know the potential at a certain location within the volume V and in this section, we will derive a formula with this goal. First, let us restate the problem of electrocardiography as we have defined it in the previous

section, consisting of Laplace's equation and the accompanying boundary condition:

$$\begin{aligned}\nabla^2\Phi &= 0 \text{ in volume } V \\ (\sigma\nabla\Phi) \cdot \bar{n}_B &= 0 \text{ on body surface } S_B\end{aligned}$$

We will now solve this problem and obtain the linear relation $\Phi_B = A\Phi_H$.

First, we start with Green's second identity. This is a relation holding for any two scalars A and B :

$$\int_S (A\nabla B - B\nabla A) \cdot \bar{n} dS = \int_V (A\nabla^2 B - B\nabla^2 A) \cdot dV \quad (8.11)$$

for a certain volume V , bounded by a surface S with normals \bar{n} . For the derivation of this identity, see for example [27]. Surface S may consist of more than one part. In our situation, it will consist of a heart surface and a body surface, as in Figure 8.1.

No special conditions are required for A and B to hold, so let's take $A = \Phi$, the scalar electric potential, and $B = 1/r$, with r the distance from an observation point o (located in the volume V) to the element of integration.

We can substitute this into equation 8.11, obtaining

$$\int_S \left(\Phi \nabla \left(\frac{1}{r} \right) - \left(\frac{1}{r} \right) \nabla \Phi \right) \cdot \bar{n} dS = \int_V \left(\Phi \nabla^2 \left(\frac{1}{r} \right) - \left(\frac{1}{r} \right) \nabla^2 \Phi \right) dV \quad (8.12)$$

Since the potential Φ satisfies the Laplace equation $\nabla^2\Phi = 0$ (see equation 8.8), the second term of the integral disappears, giving:

$$\int_V \Phi \nabla^2 \left(\frac{1}{r} \right) dV = \int_S \left(\Phi \nabla \left(\frac{1}{r} \right) - \left(\frac{1}{r} \right) \nabla \Phi \right) \cdot \bar{n} dS \quad (8.13)$$

where we switched the left-hand side of the previous equation with the right-hand side.

Next, we can split the integral of terms into two terms of integrals and subsequently split each integral over a heart surface and a body surface, as in the following steps:

$$\begin{aligned}\int_V \Phi \nabla^2 \left(\frac{1}{r} \right) dV &= \int_S \Phi \nabla \left(\frac{1}{r} \right) \cdot \bar{n} dS - \int_S \frac{\nabla \Phi \cdot \bar{n} dS}{r} \\ &= \int_{S_H} \Phi_H \nabla \left(\frac{1}{r} \right) \cdot (-\bar{n}_H) dS_H - \int_{S_H} \frac{\nabla \Phi_H \cdot (-\bar{n}_H) dS_H}{r} + \\ &\quad \int_{S_B} \Phi_B \nabla \left(\frac{1}{r} \right) \cdot \bar{n}_B dS_B - \int_{S_B} \frac{\nabla \Phi_B \cdot \bar{n}_B dS_B}{r} \\ &= - \int_{S_H} \Phi_H \nabla \left(\frac{1}{r} \right) \cdot \bar{n}_H dS_H + \int_{S_H} \frac{\nabla \Phi_H \cdot \bar{n}_H dS_H}{r} + \\ &\quad \int_{S_B} \Phi_B \nabla \left(\frac{1}{r} \right) \cdot \bar{n}_B dS_B - \int_{S_B} \frac{\nabla \Phi_B \cdot \bar{n}_B dS_B}{r}\end{aligned} \quad (8.14)$$

Note that when splitting the integral over the whole surface into two separate integrals over the heart and body surface as we did above, we should pay special attention to the direction of \bar{n} . As can be seen in Figure 8.1, \bar{n} is always directed *out of the volume* V , while we defined \bar{n}_H as *out of the volume* H (thus into the volume V). Thus, at the surface S_H , it holds that $\bar{n} = -\bar{n}_H$, which introduces a negative sign in these integrals.

Then, due to the Neumann boundary condition from equation 8.9, $\nabla\Phi \cdot \bar{n}_B = 0$ on the body surface, eliminating the fourth term of equation 8.14. If we also multiply the left and right-hand side with -1 , then we obtain the following equation:

$$\begin{aligned} \int_V -\Phi \nabla^2 \left(\frac{1}{r} \right) dV &= \int_{S_H} \Phi_H \nabla \left(\frac{1}{r} \right) \cdot \bar{n}_H dS_H - \int_{S_H} \frac{\nabla\Phi_H \cdot \bar{n}_H dS_H}{r} - \\ &\quad \int_{S_B} \Phi_B \nabla \left(\frac{1}{r} \right) \cdot \bar{n}_B dS_B \end{aligned} \quad (8.15)$$

The reason for the multiplication with -1 is that we now have a solution to $\int_V -\Phi \nabla^2 \left(\frac{1}{r} \right) dV$. Assume that we want to know the potential at a certain observer location o , then we can take this Φ_o out of the integral and obtain as left-hand side of equation 8.15

$$-\Phi_o \int_V \nabla^2 \left(\frac{1}{r} \right) dV \quad (8.16)$$

for a certain location o . Now, we are going to use the fact that

$$\nabla^2 \left(\frac{1}{r} \right) = -4\pi\delta(r) \quad (8.17)$$

for any point r , where the delta function δ is defined as being zero everywhere except where $r = 0$, in which case it is infinite. (See for a derivation of this equality a standard work on this subject, e.g. [27], page 20.) Now, combining equation 8.16 with 8.17 yields

$$\begin{aligned} -\Phi_o \int_V \nabla^2 \left(\frac{1}{r} \right) dV &= -\Phi_o \int_V -4\pi\delta(r) dV \\ &= 4\pi\Phi_o \int_V \delta(r) dV \\ &= 4\pi\Phi_o \end{aligned} \quad (8.18)$$

where the last step is justified by the fact that, by definition, the integral over the delta function equals 1: $\int \delta(r) dV = 1$ (see [27]).

We now have redefined the left-hand side of equation 8.15. Combining this equation with equation 8.18 yields a formula for the electric potential at an observation point o :

$$\begin{aligned}
4\pi\Phi_o &= \int_{S_H} \Phi_H \nabla \left(\frac{1}{r} \right) \cdot \bar{n}_H dS_H - \int_{S_H} \frac{\nabla\Phi_H \cdot \bar{n}_H dS_H}{r} - \\
&\quad \int_{S_B} \Phi_B \nabla \left(\frac{1}{r} \right) \cdot \bar{n}_B dS_B \\
\Phi_o &= \frac{1}{4\pi} \int_{S_H} \Phi_H \nabla \left(\frac{1}{r} \right) \cdot \bar{n}_H dS_H - \frac{1}{4\pi} \int_{S_H} \frac{\nabla\Phi_H \cdot \bar{n}_H dS_H}{r} - \\
&\quad \frac{1}{4\pi} \int_{S_B} \Phi_B \nabla \left(\frac{1}{r} \right) \cdot \bar{n}_B dS_B
\end{aligned} \tag{8.19}$$

Now, we are going to expand the term $\nabla \left(\frac{1}{r} \right)$. By definition, r is the magnitude of a vector from the observation point o to the location of the electrical source s :

$$r = \sqrt{(x_s - x_o)^2 + (y_s - y_o)^2 + (z_s - z_o)^2} \tag{8.20}$$

Define \bar{a} as the unit vector from the source point s to the observation point o . Carrying out the gradient operation ∇ we get (see [27] for more details):

$$\begin{aligned}
\nabla \left(\frac{1}{r} \right) &= \frac{\partial}{\partial x} \left(\frac{1}{r} \right) \bar{a}_x + \frac{\partial}{\partial y} \left(\frac{1}{r} \right) \bar{a}_y + \frac{\partial}{\partial z} \left(\frac{1}{r} \right) \bar{a}_z \\
&= \frac{1}{r^2} \left[\frac{(x_o - x_s)\bar{a}_x + (y_o - y_s)\bar{a}_y + (z_o - z_s)\bar{a}_z}{r} \right] \\
&= \frac{\bar{a}}{r^2}
\end{aligned} \tag{8.21}$$

However, \bar{a} points from the source point s to the observation point o , while actually we are evaluating from a certain observation point o the integral over the whole surface (that is, over all source points s). Thus, the use of a vector $\bar{r} = -\bar{a}$ that points from the observation point o to a source point s is more convenient. Combined with 8.21 we get:

$$\nabla \left(\frac{1}{r} \right) = -\frac{\bar{r}}{r^2} \tag{8.22}$$

which, together with 8.19 yields our final formula for obtaining the potential at a certain observation point o between the heart surface S_H that contains all electrical sources and the surrounding body surface S_B as in Figure 8.1:

$$\begin{aligned}
\Phi_o &= -\frac{1}{4\pi} \int_{S_H} \Phi_H \frac{\bar{r} \cdot \bar{n}_H}{r^2} dS_H - \frac{1}{4\pi} \int_{S_H} \frac{\nabla\Phi_H \cdot \bar{n}_H}{r} dS_H \\
&\quad + \frac{1}{4\pi} \int_{S_B} \Phi_B \frac{\bar{r} \cdot \bar{n}_B}{r^2} dS_B
\end{aligned} \tag{8.23}$$

with Φ_o the potential at this observation point, Φ_H the potential at the element of

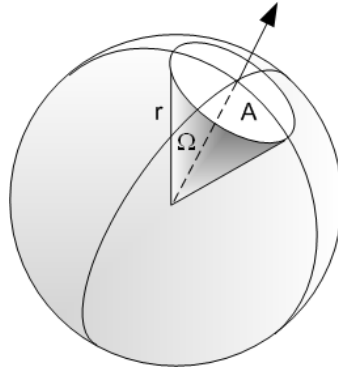


FIGURE 8.2: The solid angle Ω can be interpreted as the area A intercepted on a unit sphere by the rays r drawn to the periphery of a surface element (now shown here) in three-dimensional space.

integration at the heart surface, \bar{n}_H the normal at this element of integration at the heart surface, pointing outwards, Φ_B and \bar{n}_H similarly, but then for the body surface, \bar{r} the unit vector pointing from the observation point o to the element of integration and r the distance between the observation point and the element of integration.

In this formula, we recognize a solid angle. The *solid angle*, a measure for the two-dimensional angle that an object subtends at a point in three-dimensional space as in Figure 8.2, is defined as:

$$d\Omega = \frac{\bar{r} \cdot \bar{n}}{r^2} dS \quad (8.24)$$

This allows us to rewrite equation 8.23 as:

$$\Phi_o = -\frac{1}{4\pi} \int_{S_H} \Phi_H d\Omega_H - \frac{1}{4\pi} \int_{S_H} \frac{\nabla\Phi_H \cdot \bar{n}_H}{r} dS_H + \frac{1}{4\pi} \int_{S_B} \Phi_B d\Omega_B \quad (8.25)$$

Here, the first two integrals take into account the potentials and gradients of potential (that is, the currents) that exist on the cardiac surface. As they are two distinct integrals, they might suggest that they are not related, but in fact, the potentials and gradients at the heart surface are not independent of each other [27]. The last integral reflects that the potential at a point on the body surface is also influenced by all other locations at the body surface. This might seem strange, but a little more thought elucidates this matter. Indeed, the body surface represents the discontinuity between the conducting torso and the nonconducting air. Accordingly, secondary electrical sources arise at this surface and the potential of any surface location will depend on the field generated by all such secondary sources. In general, this means that the body surface sources cause the body surface potentials to be larger than they otherwise would be, by approximately a factor of 2 or 3 [27].

Equation 8.24 arises from field theoretic considerations, but integrals in there also have another interpretation. The first two integrals can be thought to represent primary sources, namely a double layer with its strength depending on the potential Φ_H , as in the first integral, and a single layer with its strength depending on the gradient of the potential $\nabla\Phi_H$, as in the second integral.

8.1.3 Finding the transfer matrix

It is important to recognize that the observation point o can be placed anywhere in the volume V between the heart surface and the body surface. Because we want to find a relation between the potentials at the heart surface and the potentials at the body surface, a logical step would be to place the observation point arbitrary close to either the heart or body surface, such that the corresponding potential almost equals that of the surface point. Repeating this for all locations will lead to a set of simultaneous linear equations relating the body surface locations to the heart surface locations that can be expressed in matrix form [27]:

$$\Phi_B = A\Phi_H \quad (8.26)$$

Exact derivation of these linear equations can be obtained in several similar ways, as described in [25, 29, 30]. Basically, the observation point is placed at each location of the heart and body surface, then equation 8.25 is used to get an expression for the potential at that location, and all resulting equations are combined into a matrix form. Our approach is based on the well-known article by Barr, published in 1977 already [30], combined with more recent techniques. Our implementation of the set of simultaneous linear equations as derived by Barr will be explained in chapter 10.

8.2 Measuring errors

In our experiments, we will be reconstructing surface potentials. To assess the quality of these reconstructions, we need a measure for determining how well our reconstructed potentials match the original potentials. Therefore, let us define the *relative error* to compare a set of known (correct) potentials with a set of reconstructed potentials as in [31]:

$$RE = \sqrt{\frac{\sum_{i=1}^n (\Phi_R^i - \Phi_C^i)^2}{\sum_{i=1}^n (\Phi_C^i)^2}} \quad (8.27)$$

where the Φ_R^i stands for the reconstructed potentials at electrode i and Φ_C^i for the correct potentials at that electrode. We also define the *normalized relative error*, which

is the relative error of the two normalized sets of potentials:

$$RE_{norm} = \sqrt{\frac{\sum_{i=1}^n (\tilde{\Phi}_R^i - \tilde{\Phi}_C^i)^2}{\sum_{i=1}^n (\tilde{\Phi}_C^i)^2}} \quad (8.28)$$

where $\tilde{\Phi}_R^i$ and $\tilde{\Phi}_C^i$ now stand for the normalized reconstructed and correct potentials respectively. Normalizing is done by dividing each potential by the standard deviation of its set:

$$\tilde{\Phi}_{set}^i = \frac{\Phi_{set}^i}{std(\tilde{\Phi}_{set})} \quad (8.29)$$

with $std(\tilde{\Phi}_{set})$ denoting the standard deviation of the total set of potentials $\tilde{\Phi}_{set}$.

Chapter 9

Data and model description

For validation and experiments, we use several simple and more complex models and data sets. Each model consists of a heart and a body surface. In some models, we know the heart potentials and can apply our implementation of the forward problem to calculate the body surface potentials. In other models, we know only the body surface potentials. And in some, we know both, which means we can use those to validate our methods.

In all models, the heart and body surface consist of vertices that are connected in such a way that they span a surface of triangles that represents the heart or body surface, see Figure 9.1. Each vertex can be assigned a certain electrical potential, which can be visualized by coloring the surface accordingly.

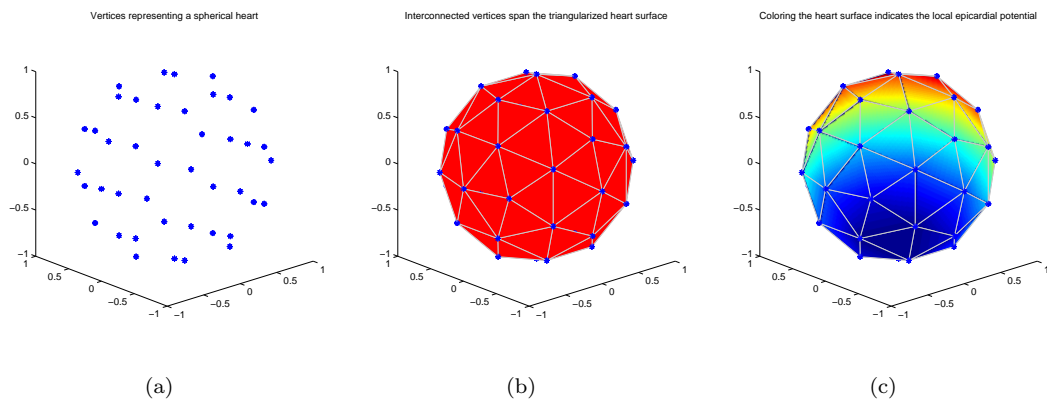


FIGURE 9.1: A cloud of vertices can represent a heart (or body) surface, but the location of the vertices only is not enough to reconstruct this surface, see subfigure (a). We need a specification on how exactly the vertices should be connected to span a surface; for this purpose, a triangulation is used and results in the surface of subfigure (b). Now, each vertex can be assigned a certain electrical potential, which can be visualized by coloring the surface accordingly, as in (c).

9.1 The concentric spheres model

Our most simple model consists of two spheres, one representing the heart, and a bigger one representing the body. These are either concentric, meaning that their centers are at the same location, or eccentric, when the heart sphere is moved in a certain direction within the body sphere.

In the concentric spheres model, the centers of the heart sphere and the body sphere coincide. We can place an electric dipole at this center, which consists of two charges of equal strength but opposite sign, placed at some distance from each other, thereby generating a field of electrical potentials. When placed at the center of the heart and body, a dipole results in a potential distribution across the corresponding surfaces.

These potentials can be computed analytically, which provides us with a set of analytical data that can be used as golden standard for validation of our methods. For example, we can use the analytically known heart surface potentials, apply the forward method to obtain computed body surface potentials, and compare those to the analytically known body surface potentials for validation. By reversing the process, using known body surface potentials as a start, our inverse method yields reconstructed heart surface potentials, which can be compared with the analytically known heart surface potentials.

The epicardial (heart surface) potentials can be determined according to the following formula [30]:

$$\Phi_H^i = \frac{1}{4\pi\sigma} \frac{\bar{p} \cdot \hat{r}_H^i}{(r_H)^2} \left[\frac{2r_H}{r_B} + \left(\frac{r_B}{r_H} \right)^2 \right] \quad (9.1)$$

where Φ_H^i stands for the electrical potential at a certain point i at the heart surface, σ is the conductivity of the heart (taken one in this experiment), \bar{p} is the dipole moment (which indirectly is a measure for the strength of the dipole), \hat{r}_H^i is a unit vector to our point i and r_B and r_H are the radii of our body and heart spheres.

The analytical potentials at the body surface can be determined from the fact that electrical potentials at a body surface, resulting from a centric dipole, are three times the potentials from the same dipole in a homogeneous volume conductor of infinite extent [30]:

$$\Phi_B^i = 3 \frac{1}{4\pi\epsilon} \frac{\bar{p} \cdot \hat{r}_B^i}{|\hat{r}_B^i|^2} \quad (9.2)$$

where Φ_B^i is the electrical potential at a body surface location i , ϵ is the permittivity (taken one), \hat{r}_B^i is a unit vector from the dipole to our point i and $|\hat{r}_B^i|$ is the corresponding distance to the dipole.

Heart and torso, with local potentials as normalized colors

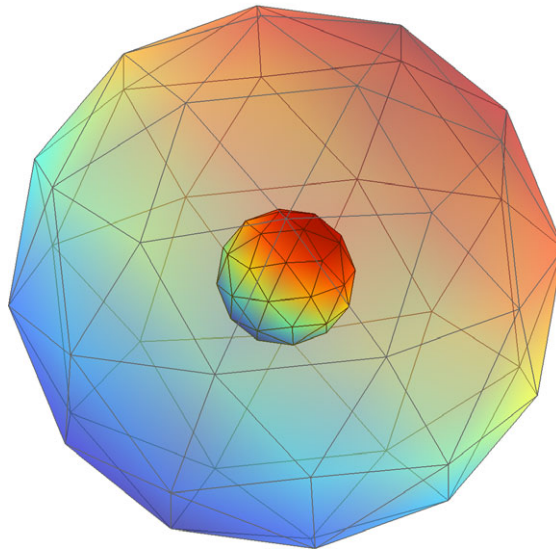


FIGURE 9.2: A concentric spheres model with a heart radius of 1, a body radius of 4. A dipole with moment $\bar{p} = (1 \ 1 \ 1)$ is placed at the center, and the corresponding electrical potentials at the heart and body surface are analytically computed.

With these formulas, we can analytically obtain electrical potentials at heart and body surfaces for our concentric spheres model. We can vary the size of the heart and the torso to generate different types of geometry for our experiments. For an example of a specific model and corresponding potentials, see Figure 9.2.

9.2 Eccentric spheres model

When the centers of the heart sphere and the body sphere do not coincide, the eccentric spheres model applies. In this case, the heart sphere is moved relative to the body sphere. This resembles the physiological case better than the concentric spheres model, as the human heart is also not centered in the human torso.

However, for this case it is not possible to analytically determine the heart and body surface potentials, as the symmetry of the concentric spheres model is lost and the previously mentioned formulas do not apply. However, some basic experiments can still be performed by applying the dipole distribution to the heart and visually inspecting the corresponding body surface potentials that are computed with the forward method. This will be described in more detail in subsequent chapters.

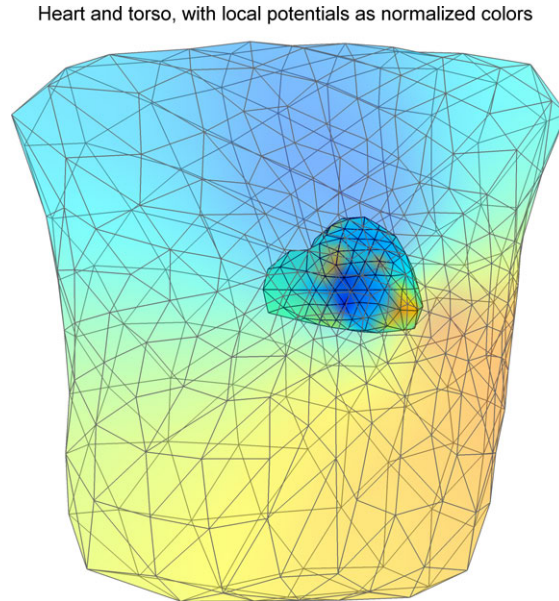


FIGURE 9.3: Geometric model and potential data extracted from the ECGsim package.

9.3 ECGsim model

ECGsim is a simulation program to investigate ECGs, developed by Van Oosterom and Oostendorp [32]. From this program, the geometrical data of heart and body could be extracted, along with heart and body surface potentials for one heart beat, see Figure 9.3. These given potentials were used as reference to validate our own methods.

It should be noted, however, that the ECGsim package is a simulation program itself; we should not pay too much value to the comparison with our own reconstructions, as these simulations themselves could be not (entirely) correct. Furthermore, we now have (simulated) data on one whole human heart beat available, which makes it possible to investigate our methods for time series of more or less realistic data.

9.4 Geometrical and practical issues

Until now, we did not stress some important properties of the geometry of our models. Each geometry is the combined set of a heart surface and a body surface, being very simple, as in Figure 9.2, or more complex, as in Figure 9.3. A surface is represented by vertices with a known (x, y, z) location in three-dimensional space, and a *triangulation*. A triangulation is a description of the connections between the vertices. Each vertex is connected with other vertices in such a way that the resulting surface is made of triangles.

Each vertex is considered a location where the potential is known. This means, that there are N_B body-surface vertices and N_H heart-surface vertices. The number of triangles connecting these vertices is typically some factors higher.

Chapter 10

Implementation of the forward method

In section 8.1 we derived the forward model. For a model with a heart surface S_H and a body surface S_B , we saw that Laplace's equation should be solved. By doing so, we ultimately obtained an expression for the electrical potential Φ_o at a location o the volume between the two surfaces, see equation 8.25.

Now, assume there are N_H locations at the heart surface of which we know the electrical potential, and there are N_B locations at the body surface where we want to compute the resulting electrical potentials. We can obtain equations for those by placing our observation point o at the i^{th} location at the heart surface and the i^{th} location at the body surface. The following two equations relate either the body-surface potentials respectively the heart-surface potentials to all other potentials:

$$\Phi_B^i = -\frac{1}{4\pi} \int_{S_H} \Phi_H d\Omega_{BH}^i - \frac{1}{4\pi} \int_{S_H} \frac{\nabla\Phi_H \cdot \bar{n}_H}{r^i} dS_H + \frac{1}{4\pi} \int_{S_B} \Phi_B d\Omega_{BB}^i \quad (10.1)$$

$$\Phi_H^i = -\frac{1}{4\pi} \int_{S_H} \Phi_H d\Omega_{HH}^i - \frac{1}{4\pi} \int_{S_H} \frac{\nabla\Phi_H \cdot \bar{n}_H}{r^i} dS_H + \frac{1}{4\pi} \int_{S_B} \Phi_B d\Omega_{HB}^i \quad (10.2)$$

where $d\Omega_B^i$ now stand for the element of the solid angle spanned by the surface-element of integration (at the corresponding surface) from the i^{th} observation point. Note that the solid angle can both be from an observation point at one surface to an element of integration at the other surface, as to an element of integration at the same surface. The exact solid angle depends on the location of the observation point, which means that the solid angle in the first term of equation 10.1 is different (namely, from body to heart) from that of equation 10.2 (where it is from heart to heart). This is indicated with the extra subscript. Furthermore, in this notation, r^i reflects the distance from the i^{th} observation point to the element of integration.

Placing all terms on the same side and taking similar ones together in brackets yields:

$$\begin{aligned} & \left(-\frac{1}{4\pi} \int_{S_H} \Phi_H d\Omega_{BH}^i \right) + \left(-\frac{1}{4\pi} \int_{S_H} \frac{\nabla\Phi_H \cdot \bar{n}_H}{r^i} dS_H \right) \\ & + \left(-\Phi_B^i + \frac{1}{4\pi} \int_{S_B} \Phi_B d\Omega_{BB}^i \right) = 0 \end{aligned} \quad (10.3)$$

$$\begin{aligned} & \left(-\Phi_H^i - \frac{1}{4\pi} \int_{S_H} \Phi_H d\Omega_{HH}^i \right) + \left(-\frac{1}{4\pi} \int_{S_H} \frac{\nabla\Phi_H \cdot \bar{n}_H}{r^i} dS_H \right) \\ & + \left(\frac{1}{4\pi} \int_{S_B} \Phi_B d\Omega_{HB}^i \right) = 0 \end{aligned} \quad (10.4)$$

Now we can set up a discretization scheme for each of the terms as follows. We define coefficients p and g such that they satisfy the following requirements. For equation 10.3 we get:

$$-\frac{1}{4\pi} \int_{S_H} \Phi_H d\Omega_{BH}^i = \sum_{j=1}^{N_H} p_{BH}^{ij} \Phi_H^j \quad (10.5)$$

$$-\frac{1}{4\pi} \int_{S_H} \frac{\nabla\Phi_H \cdot \bar{n}_H}{r^i} dS_H = \sum_{j=1}^{N_H} g_{BH}^{ij} \Gamma_H^j \quad (10.6)$$

$$-\Phi_B^i + \frac{1}{4\pi} \int_{S_B} \Phi_B d\Omega_{BB}^i = \sum_{j=1}^{N_B} p_{BB}^{ij} \Phi_B^j \quad (10.7)$$

And for equation 10.4, we get:

$$-\Phi_H^i - \frac{1}{4\pi} \int_{S_H} \Phi_H d\Omega_{HH}^i = \sum_{j=1}^{N_H} p_{HH}^{ij} \Phi_H^j \quad (10.8)$$

$$-\frac{1}{4\pi} \int_{S_H} \frac{\nabla\Phi_H \cdot \bar{n}_H}{r^i} dS_H = \sum_{j=1}^{N_H} g_{HH}^{ij} \Gamma_H^j \quad (10.9)$$

$$\frac{1}{4\pi} \int_{S_B} \Phi_B d\Omega_{HB}^i = \sum_{j=1}^{N_B} p_{HB}^{ij} \Phi_B^j \quad (10.10)$$

In these equations, Φ_B and Φ_H represent the vectors of all body-surface or heart-surface potentials. When a superscript is added, Φ_B^j and Φ_H^j reflect the potential at the j^{th} location at either the heart surface or the body surface, respectively. An element of the solid angle $d\Omega_{BH}^i$ is determined from its observer location (the i^{th} node in this case) at a certain surface (here the body surface) to the element of integration (in this case an element from the heart surface). The other solid angles are determined similarly.

The p_{BH}^{ij} 's (and similar for the other p 's and g 's) that result from a certain integral then of course also reflect properties of an observer location at position i of the body surface, and an element of summation (originally the element of integration) at location j of the

heart surface. All p 's and g 's are coefficients whose values are determined on the basis of geometry only, by either solid angles or gradients.

We can substitute the above implicit definition of the p and g vectors into equations 10.3 and 10.4, obtaining a vector notation for our simultaneous linear equations:

$$\sum_{j=1}^{N_H} p_{BH}^{ij} \Phi_H^j + \sum_{j=1}^{N_H} g_{BH}^{ij} \Gamma_H^j + \sum_{j=1}^{N_B} p_{BB}^{ij} \Phi_B^j = 0 \quad (10.11)$$

$$\sum_{j=1}^{N_H} p_{HH}^{ij} \Phi_H^j + \sum_{j=1}^{N_H} g_{HH}^{ij} \Gamma_H^j + \sum_{j=1}^{N_B} p_{HB}^{ij} \Phi_B^j = 0 \quad (10.12)$$

We can further simplify these by noting that each term is a sum of products of individual, subsequent elements of the vectors. This is the definition of multiplication of two vectors, thus we can write each term as a vector multiplication and obtain:

$$p_{BH}^i \Phi_H + g_{BH}^i \Gamma_H + p_{BB}^i \Phi_B = 0, \quad \forall i \in \{1, 2, \dots, N_B\} \quad (10.13)$$

$$p_{HH}^i \Phi_H + g_{HH}^i \Gamma_H + p_{HB}^i \Phi_B = 0, \quad \forall i \in \{1, 2, \dots, N_H\} \quad (10.14)$$

Remember that we have N_B (the number of body-surface locations) equations of type 10.13, since i runs from 1 to N_B . Similarly, there are N_H equations of type 10.14. We can combine those sets of equations and write them as a matrix system:

$$P_{BH} \Phi_H + G_{BH} \Gamma_H + P_{BB} \Phi_B = 0 \quad (10.15)$$

$$P_{HH} \Phi_H + G_{HH} \Gamma_H + P_{HB} \Phi_B = 0 \quad (10.16)$$

where each P and G result from the combination of the successive separate equations. By inspecting the equations, we see that the P 's are coefficients for potentials Φ at either the heart or body surface, and the G 's are coefficients for the normal components of the potential gradients Γ_H at the heart surface. This is a very nice property, as this means that all our coefficients are independent of the potentials.

However, this also means that we not only have to use the potentials Φ as an input to our system, but also explicitly the potential gradients Γ_H at the heart surface. Luckily, we can eliminate Γ_H by solving from equation 10.16:

$$\begin{aligned} \Gamma_H &= G_{HH}^{-1} (-P_{HB} \Phi_B - P_{HH} \Phi_H) \\ &= -G_{HH}^{-1} (P_{HB} \Phi_B + P_{HH} \Phi_H) \end{aligned} \quad (10.17)$$

For this, we need the inverse of G_{HH} , which should be no problem, as it is a square matrix (with N_H rows and columns) of full rank. When substituting this result into equation 10.15 and rearranging the results we obtain a nice relation between the potentials at the

heart surface and the potentials at the body surface:

$$\begin{aligned}
0 &= P_{BH}\Phi_H + G_{BH}(-G_{HH}^{-1}(P_{HB}\Phi_B + P_{HH}\Phi_H)) + P_{BB}\Phi_B \\
0 &= P_{BH}\Phi_H - G_{BH}G_{HH}^{-1}(P_{HB}\Phi_B + P_{HH}\Phi_H) + P_{BB}\Phi_B \\
0 &= P_{BH}\Phi_H - G_{BH}G_{HH}^{-1}P_{HB}\Phi_B - G_{BH}G_{HH}^{-1}P_{HH}\Phi_H + P_{BB}\Phi_B \\
0 &= (P_{BH} - G_{BH}G_{HH}^{-1}P_{HH})\Phi_H - (P_{BB} - G_{BH}G_{HH}^{-1}P_{HB})\Phi_B \\
\Phi_B &= (P_{BB} - G_{BH}G_{HH}^{-1}P_{HB})^{-1}(G_{BH}G_{HH}^{-1}P_{HH} - P_{BH})\Phi_H \\
\Phi_B &= A\Phi_H
\end{aligned} \tag{10.18}$$

Finally, we have obtained our linear relation $\Phi_B = A\Phi_H$, relating the heart-surface potentials with the body-surface potentials by means of transfer matrix A . We now also know how matrix A is defined, namely:

$$A = (P_{BB} - G_{BH}G_{HH}^{-1}P_{HB})^{-1}(G_{BH}G_{HH}^{-1}P_{HH} - P_{BH}) \tag{10.19}$$

where the P and G matrices are as defined by our discretization scheme mentioned above.

The above results are the same as the derivations made by Barr in 1977, see [30]. Also Horáček et al. [29] derived similar results. They also present methods to obtain the geometrical coefficients for the P and G matrices, some of which will be discussed in the following sections.

10.1 Finding the coefficients of the transfer matrix

The discretization scheme defined by equations 10.5 to 10.8 provides a method to determine the coefficients of the elements of the P and G matrices, and thereby indirectly also those of the transfer matrix A . We followed the method described by Barr [30] to obtain those coefficients. We will not go into too much detail here, as their article elucidates this process quite thoroughly.

Each of the equations of our discretization scheme has a basic form: for each vertex i , an integral over either a solid angle or a gradient is set equal to the coefficient vector p or g multiplied with a potential or gradient vector. In general, it is impossible to make the right-hand side of the discretization equations equal to the left-hand side. Therefore, Barr tries to approximate the elements of the corresponding P and G matrices as good as possible.

A first step is to divide the integrals in two parts: a part that integrates all vertices that lie close to the observation point, and a part that integrates all vertices that lie far from the observation point. A vertex is considered “close” when it is adjacent to the observation vertex. Then, the close region integral can be computed from a simple product over all close triangles, while the far region integral consists of a product over all “far” triangles.

However, we do not know the electrical values (potential or gradient) at a triangle, but we only know the values at the vertices of that triangle. A simple approximation is to assume that the electrical value of the triangle is the average of the values at the vertices of that triangle.

These steps result in a general method for obtaining the coefficients of a P or G matrix, by evaluating a summation over close and distant triangles, involving either solid angles (for the P matrices) or gradients (for the G matrices). For each of the P and G matrices, Barr [30] describes a specific approach to apply the general method for that specific matrix, which can then be combined to obtain the transfer matrix A with use of equation 10.19. We will not repeat those methods here, as they are quite straightforward and are described good enough. We will, however, briefly describe the most important parts, namely the computation of the solid angle and the computation of the integral dS/r needed for the gradient.

10.1.1 Computation of the solid angle

Evaluating the discretization scheme for the P matrices requires the computation of solid angles. The idea behind the solid angle was explained in Figure 8.2. We did not implement the Barr method for computing solid angles, as it is sensitive to numerical errors. Van Oosterom et al. published an alternative method [33], that is computationally more stable and faster.

They presented an efficient formula for calculating the solid angle at an observation point o subtended by the triangular surface ABC where \bar{a} , \bar{b} and \bar{c} are the vectors spanning that triangle:

$$\tan\left(\frac{1}{2}\Omega\right) = \frac{[\bar{a} \ \bar{b} \ \bar{c}]}{abc + (\bar{a} \cdot \bar{b})c + (\bar{a} \cdot \bar{c})b + (\bar{b} \cdot \bar{c})a}$$

where $[\bar{a} \ \bar{b} \ \bar{c}] = \bar{a} \cdot (\bar{b} \times \bar{c})$ is the triple scalar product. That means that we can find the solid angle with:

$$\Omega = 2 \arctan\left(\frac{[\bar{a} \ \bar{b} \ \bar{c}]}{abc + (\bar{a} \cdot \bar{b})c + (\bar{a} \cdot \bar{c})b + (\bar{b} \cdot \bar{c})a}\right) \quad (10.20)$$

The ordering of \bar{a} , \bar{b} and \bar{c} ensures that the sign of the solid angle automatically switches when the observation point moves from one side of the plane of the triangle to the other, as is required.

10.1.2 Computation of the gradient integral

Computing the geometrical part of the gradient involves integrating over the distance r to an arbitrary placed triangle. For example, for a vertex i at the body surface and triangle k at the heart surface, we would need to evaluate the following equation

$$\int_{S_H^k} \frac{dS_H}{r_H^i}$$

In obtaining the result, we used some simplifications, described in appendix III of [30]. Basically, a solution is known when we have a pie-shaped area instead of a triangle, and our observation point is positioned perpendicular to this area. However, the pie-shaped area can be approximated very well by a triangle. In that case, the assumption of perpendicularity generates an approximated solution in the general case, but an exact result in the case where the distance to the triangle is zero (and the value of the integral is largest). In other words, it gives the best result in the most important case.

10.2 Implementation

In section 8.1, we derived an equation for obtaining the electrical potential in the body torso. In this chapter, we derived a linear relation $\Phi_B = A\Phi_H$ that relates the heart-surface potentials to the body-surface potentials by means of a matrix A that is only dependent on the geometry, and not on the potentials at the body or heart surface. In addition, we briefly described methods to find the coefficients of this transfer matrix, based on [30].

After this theoretical development, we implemented the algorithms as described above to obtain the transfer matrix A . Implementation was done in the mathematical development software MATLAB[®] (The MathWorks, Inc., Natick, MS, US). Extensive validation was performed, which is described in the next chapter.

It should be noted that other approaches to the forward problem of electrocardiography have been pursued. For example, Horáček [29] has derived very similar results. Stenroos [34, 35], on the other hand, tried to present the problem in terms of residual minimization, in order to be able to apply other methods for discretization, for example the

Galerkin method. He also compared different methods, but did not find very remarkable differences between them.

Therefore, we focused only on the method described here. In our development environment, we created software for processing data, representing geometries and computing the associated transfer matrix. Also, methods for visualizing and comparing results of experiments were written. The following chapter will describe the results of the validation of the forward methods we have described thus far.

Chapter 11

Validation of the forward implementation

In this chapter we will describe the validation of our implementation regarding the forward problem. For this, we used the concentric and eccentric sphere models, and the ECGsim model, described in Chapter 9.

11.1 Concentric spheres model

The most reliable validation we can perform is with the concentric spheres model, because we can use physical laws to calculate both the heart-surface potentials and body-surface potentials that result from a dipole placed at the center of the spheres, as described in section 9.1. In Figure 11.1, we placed a dipole with moment $\bar{p} = (1 \ 1 \ 1)$ at the center and analytically determined the resulting potential distribution.

Next, we applied our forward algorithm to the analytically computed heart-surface potentials to obtain reconstructed body-surface potentials. Those reconstructed body-surface potentials were compared to the analytically computed body-surface potentials to validate the algorithm. In Figure 11.2, both known and reconstructed potential distributions are shown. From the scale of the coloring, we can see that the reconstructed potentials are too high in amplitude. Their distribution, however, seems to be correct. This is confirmed in Figure 11.3, where we normalized the potentials and see a perfect fit between the distribution of the known and reconstructed potentials.

When we look at the relative error, as defined in section 8.2, we indeed see that this mismatch is very high: 32.3. This confirms that the potentials are, at least in magnitude,

Heart and torso, with local potentials as normalized colors

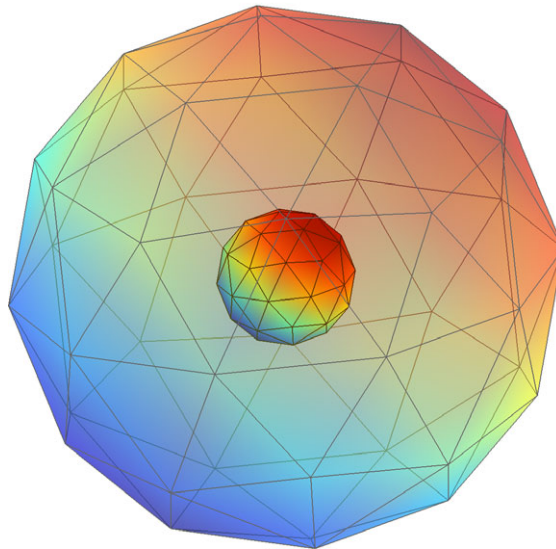


FIGURE 11.1: A concentric spheres model with a heart radius of 1, a body radius of 4. A dipole with moment $\bar{p} = (1 \ 1 \ 1)$ is placed at the center, and the corresponding electrical potentials at the heart and body surface are analytically computed.

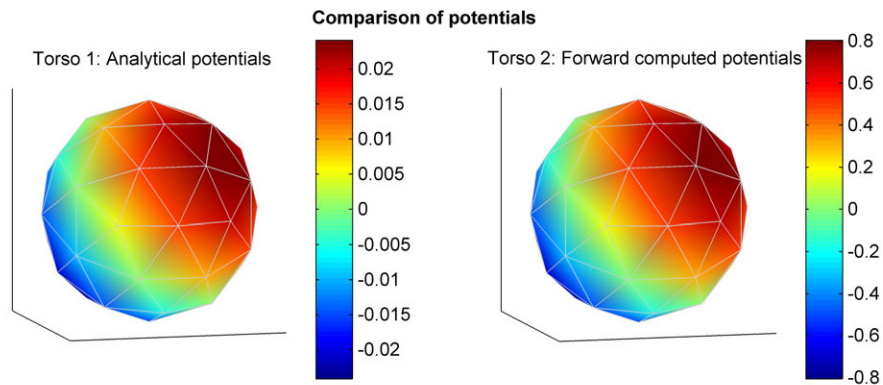


FIGURE 11.2: A comparison between the analytically known body-surface potentials (left), and the forward computed body-surface potentials (right), when a dipole with moment $\bar{p} = (1 \ 1 \ 1)$ is placed at the center. It can be seen that the distribution of the reconstructed body-surface potentials fits the known potentials perfectly. Note from the color scale however, that their amplitude is too high.

incorrect. However, the relative error of the normalized sets indeed confirms that the distributions fit perfectly, as this normalized relative error is only 0.002.

Thus, although the forward computed potentials are too high, their distribution perfectly fits the analytical distribution. Because this phenomenon was not described in the original article by Barr [30], we must assume that this is a defect in our implementation. However, we should also note that in practice, we are not interested in amplitudes at all, but only in the distribution. Nevertheless, extensive analysis of this defect was performed and is described in the following subsection.

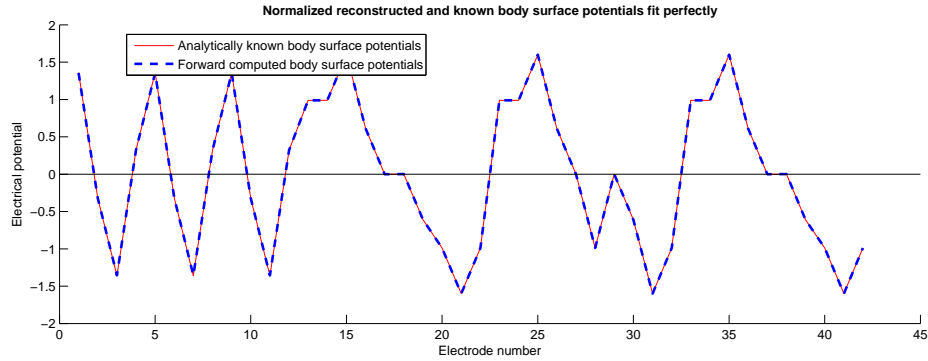


FIGURE 11.3: This figure shows both the analytically determined body-surface potentials, and the forward computed body-surface potentials, at each of the 42 virtual body-surface “electrodes”. The ordering of the vertices (or electrodes) is arbitrary. Both potential distributions are normalized by dividing them by their standard deviation, because we know that the reconstructed potentials are too large in amplitude. Therefore, we are mainly interested in their distribution, which by this figure perfectly fits the analytically known potentials as both graphs match exactly.

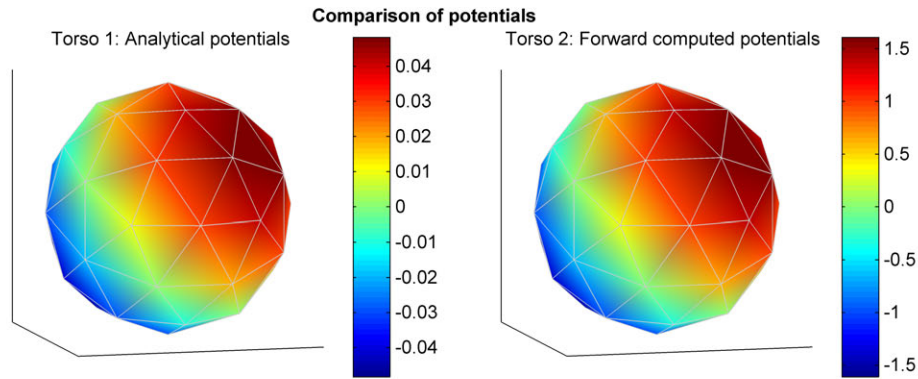


FIGURE 11.4: Same as Figure 11.2, but now with a dipole twice as strong (dipole moment $\vec{p} = (2 \ 2 \ 2)$). This results in analytical potentials twice as strong, but also the forward computed potentials are twice as strong, as can be seen from the color scale and more in detail in Figure 11.5.

11.1.1 Investigation of the scaling defect

First, note from Figures 11.4 and 11.5 that making the dipole twice as strong results in forward computed potentials that are also twice as strong, as should be the case. Thus, at least the scaling defect is consistent with the potential amplitudes being used: small source potentials will be reconstructed as (relatively) small potentials and large source potentials will be reconstructed as (relatively) large potentials. This means, that essential phenomena that depend on potential amplitude can still be extracted by investigating their “relative” amplitude. Or, in other words, when using a certain geometry, the scaling defect is a constant factor, independent of what potentials are actually applied.

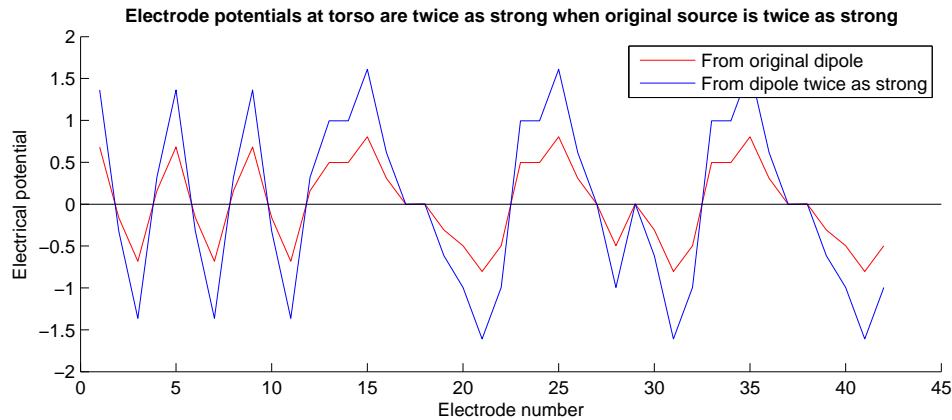


FIGURE 11.5: When we make the dipole twice as strong, the forward reconstructed potentials at the body surface are also twice as strong, as is expected.

Next, we investigated the dependency of the scaling defect on different geometries. In the first case, we scaled the heart and body spheres by the same factor. Thus each geometry is congruent to the others except for a scaling factor. This should result in a relative decrease of potential amplitudes, but no other essential changes. As Figure 11.6 shows, the scaling defect decreases as the spheres get scaled up. The figure also shows that we can fit a logarithmic function to this error. Since absolute (and not relative) distance is the only thing that differs between the geometries, these findings suggest that the scaling defect is somehow logarithmically related to the distance between geometrical subparts, as this absolute distance is the only thing that differs between the geometries.

On the other hand, these findings rule out the location of the scaling defect in our implementation of the solid angle computations. After all, scaling up both heart and body sphere with the same factor does not change any solid angle within this geometry. (This was checked experimentally.) Indeed, this is due to the definition of a solid angle, as it is an angle in three-dimensional space and angles do not change when scaling the geometry. Thus, we can cross out the solid angle implementation as a source of this defect.

The suggestion that the scaling defect is logarithmically related to the distance between *all* geometrical subparts is strengthened by Figure 11.7. This figure shows that when we keep the heart sphere at a fixed size and make the body sphere larger, the scaling defect increases (or: multiplication factor decreases).

We now have established the hypothesis that the deficit might be (logarithmically) related to distance between vertices. If we rule the solid angle, the only other location where distance is explicitly involved is the computation of the integral $\int \frac{d\bar{S}}{\bar{r}}$. To investigate this possibility, we used an alternative computation of this integral, where we added an extra distance factor. This alternative computation had no physical or mathematical

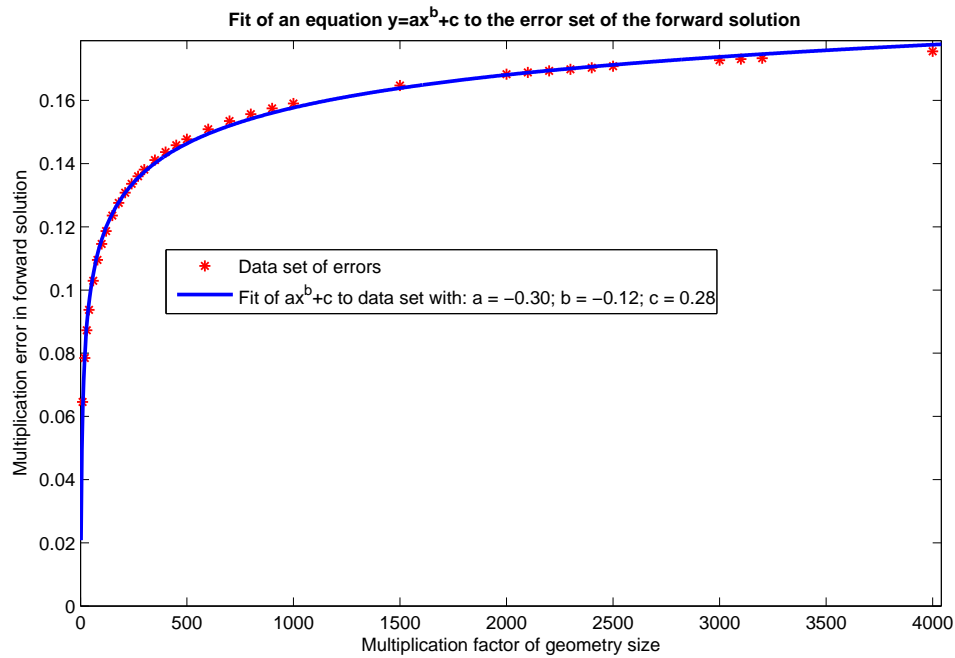


FIGURE 11.6: This plot shows the scaling defect for several similar geometrical sets of concentric heart and body spheres. Both heart and body sphere are multiplied with the same scaling factor (shown on the horizontal axis) to obtain a new but similar geometry. Of all these geometries, the associated forward multiplication error is shown (red stars) on the vertical axis. This multiplication factor is needed to obtain the correct solution. Thus, a value of 1 is optimal here, since in that case we have the correct amplitudes compared to the analytically known amplitudes. A multiplication factor of less than 1 means that our reconstructed potentials are too high and should be multiplied with a number below 1 to get the smaller correct potentials. As can be seen from the plot, the multiplication factor increases when we scale the original geometry up. We can fit a logarithmic equation to it, which suggests that the defect is somehow logarithmically related to the distance between geometrical subparts.

foundation and was only to investigate the influence of any changes to the computation of this integral. From Figure 11.8, we see that this alternative implementation, although not based on any physical grounds, improves the results.

This suggests that the defect might be in our original implementation of the computation of the integral, although we did follow the original Barr [30] implementation as close as possible. Careful investigation of our implementation did not yield any useful results. For the sake of time, we decided to postpone the investigation of the source of the scaling defect. This decision is supported by the fact that the reconstruction yields correct potential *distributions*, which in fact are far more important than the exact potential amplitudes.

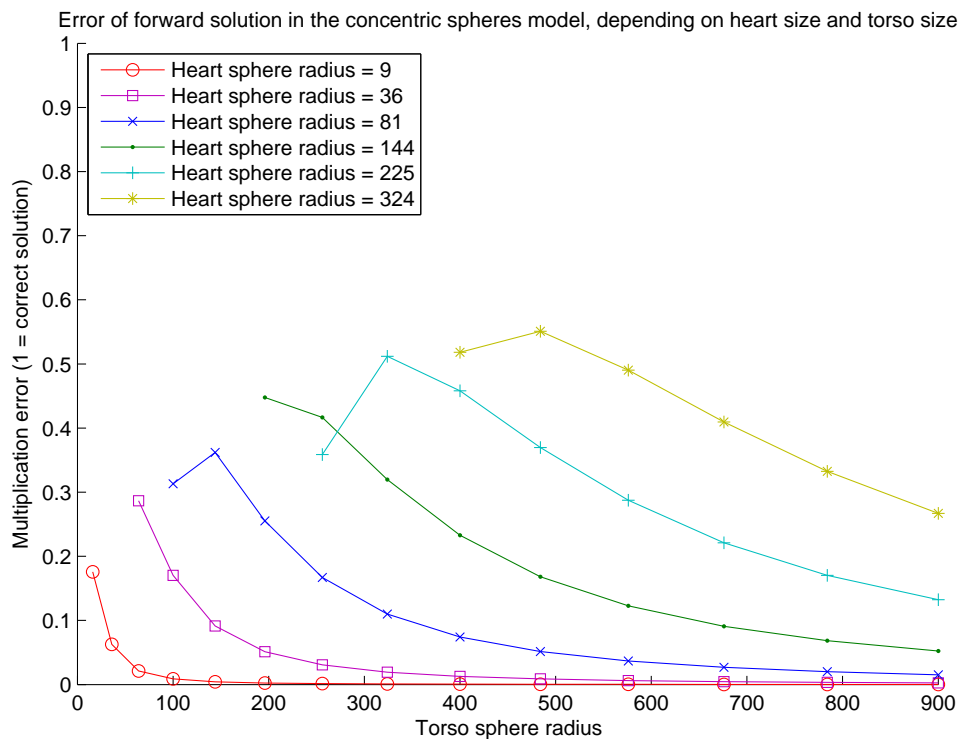


FIGURE 11.7: This Figure is similar to Figure 11.6, but now, the heart and body (torso) spheres are scaled independently of each other. The vertical axis again shows the multiplication factor needed to obtain the correct solution. From this figure, we see that when we vary the radii of the heart sphere and torso sphere independently of each other, the scaling factor is not consistent. We see that the error gets larger (that is, the multiplication factor lower) when the body sphere gets larger relative to the heart sphere.

11.2 Eccentric spheres model

Now that we have established that the potential distributions are perfectly computed in the concentric spheres model, we can increase the complexity of our model by moving the heart sphere out of the body-spheres center. However, we have no analytical formulas for computing the resulting body-surface potentials. Thus, we can reconstruct body-surface potentials from some dipole distribution on the heart surface, but cannot compare this to analytically known body-surface potentials.

However, if we move the heart sphere in a certain direction within the body sphere, the resulting body-surface potentials should be more pronounced in that direction. Indeed: when a charge is more close to the right than left part of the body surface, the largest potential amplitudes should be visible on the right side of the body surface too. Simulations confirmed this finding, as is shown in Figure 11.9, where it can be seen that the potentials are larger on the right than on the opposite side of the body. This is

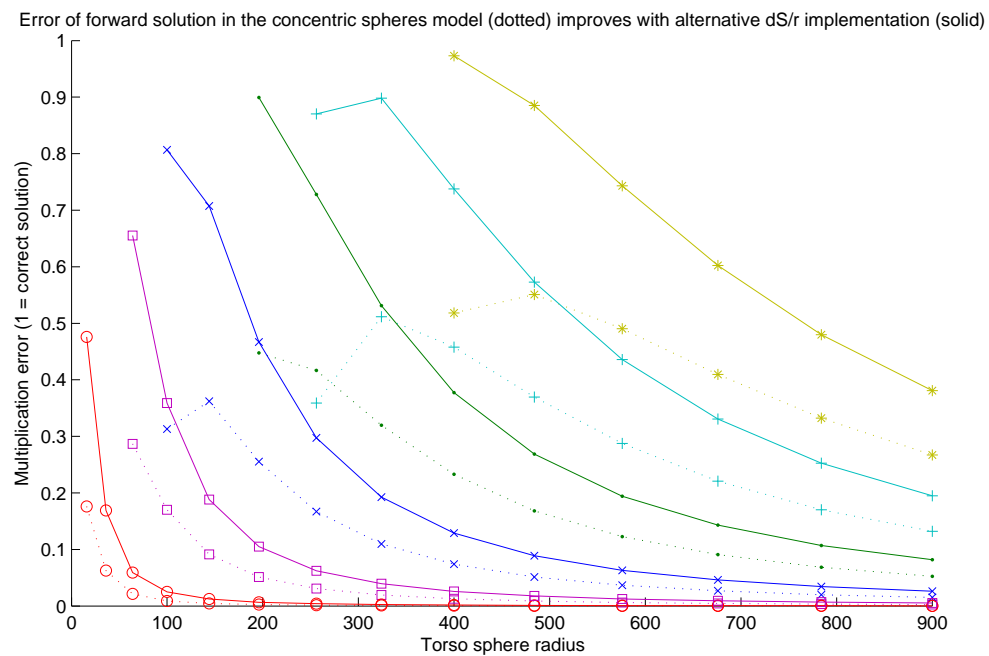


FIGURE 11.8: This figure is the same as Figure 11.7 (now as dotted lines), but now with the results of an alternative computation of $\int \frac{dS}{r}$ superimposed as solid lines. It can be seen that this improves the results, which suggests that the defect might be in our original implementation of this integral.

more clearly confirmed in Figure 11.10, where we can see the heart and body-surface potentials separately.

In another experiment we performed the same procedure, but now with a dipole twice as strong. As expected, this yielded the same results, but with body surface amplitudes twice as high. Those results are not shown here.

When the sphere is moved only half as far as the previously used direction, one would expect the body-surface potentials to be more spread out over the whole body surface. This is confirmed by Figure 11.11. In the end, we can conclude that all these experiments fit the physical predictions.

11.3 ECGsim model

From the ECGsim program, we extracted geometry and simulated heart and body-surface potentials. When we apply the forward method to these heart-surface potentials, we can compare our reconstructions with the original body-surface potentials. Because we have a time series of data available (together forming a heart beat), we can have a look at several time instants. Figure 11.12 shows the original and reconstructed body-surface potentials at several time instants around the QRS peak. Again, the potentials

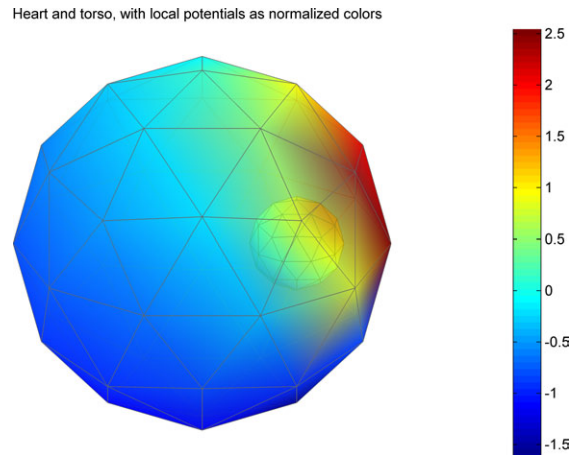


FIGURE 11.9: An eccentric spheres model with a heart radius of 1 unit, a body radius of 4 units and the heart moved 2 units in the direction of the x axis. A dipole with moment $\bar{p} = (2 \ 2 \ 2)$ is placed at the center of the heart, and the corresponding electrical potentials at the heart surface are analytically computed. No analytical potentials were known, but the forward potentials are reconstructed from the heart-surface potentials with our forward method. The figure shows the heart-surface potentials and reconstructed body-surface potentials as colors.

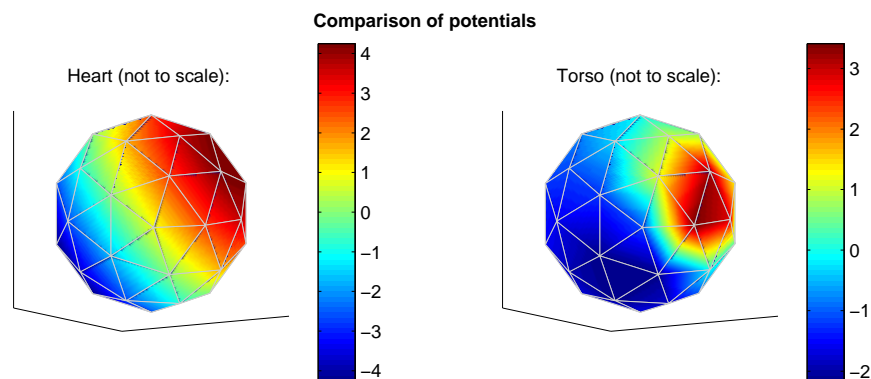


FIGURE 11.10: Heart and body surfaces in the eccentric spheres model. The heart-surface potentials are analytically computed from a dipole at its center. The corresponding body-surface potentials are not known, but can be reconstructed with the forward method. As expected, in the direction of movement (i.e., to the right and front in this image), the body-surface potentials are the most influenced by the heart-surface potentials.

are too high, as we would expect from our scaling defect, but the distributions seem to fit quite well. In most cases, the same features can be observed in both images.

The normalized relative error can be calculated at each time instant, to compare the (normalized) reconstructed potentials with the (normalized) original potentials, see Figure 11.13. Because there is no perfect match of the distributions, we see that the normalized relative error can be quite high. In other words, this error function might not be a good measure for more complex geometries and complex distributions, as a small shift in distribution already increases the relative error significantly.

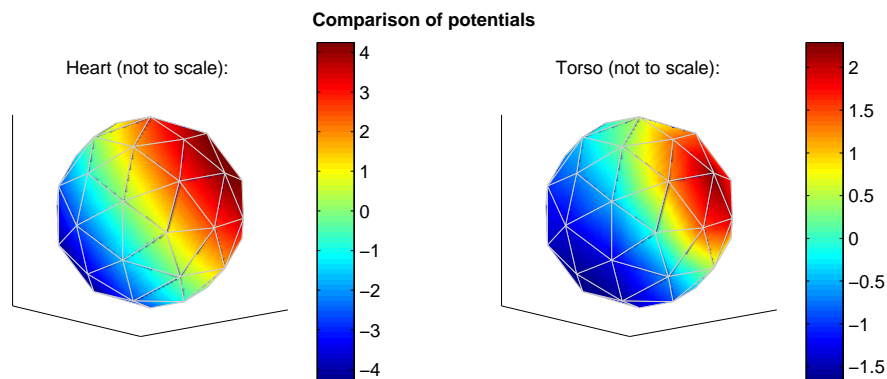


FIGURE 11.11: Similar to Figure 11.10, but now with the heart sphere only moved half as far. As expected, the resulting reconstructed body-surface potentials are less concentrated in the movement direction.

We should bear in mind, however, that the “original” potentials are simulated themselves. Thus, although we can clearly see some matches and a few mismatches, care should be taken when interpreting this as erroneous, as the original data might be flawed themselves.

11.4 Conclusion on the validation of the forward method

In conclusion, when we apply our forward method to heart-surface potentials and a certain geometry, the reconstructed body-surface potentials are too high in amplitude, but their distribution in general fits the expected distributions well. Thus, our forward method is valid, when we look only at distributions and not at amplitudes. As amplitudes are not relevant, the method is useful for obtaining forward reconstructions. Therefore, it will also be useful as a basis for our inverse reconstructions.

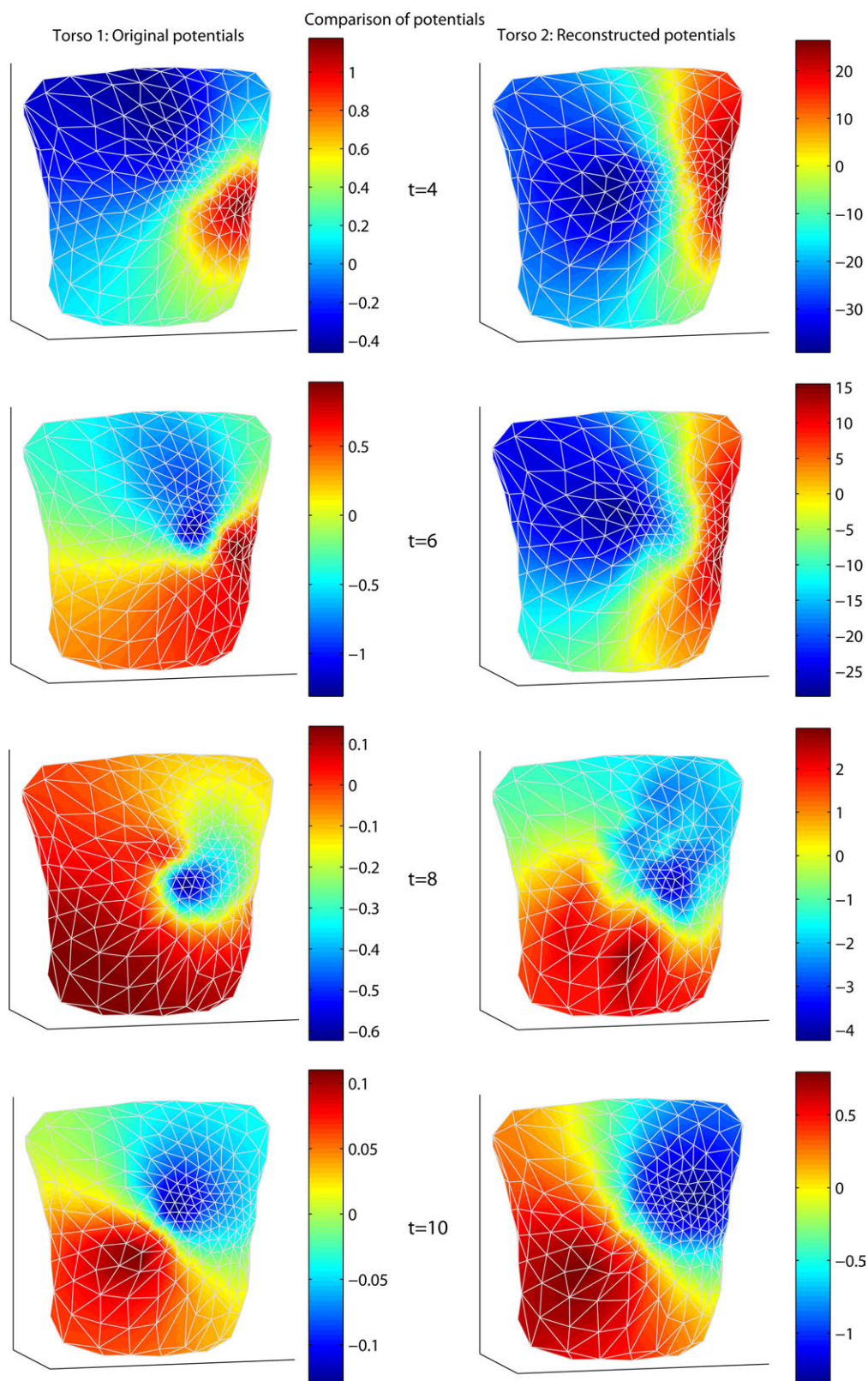


FIGURE 11.12: At time instants $t=4, 6, 8$ and 10 (corresponding to time instants of the QRS complex), both the original (left column) and our reconstructed potentials (right column) are shown. It can be seen that the same features can be extracted from our reconstructions and from the original images.

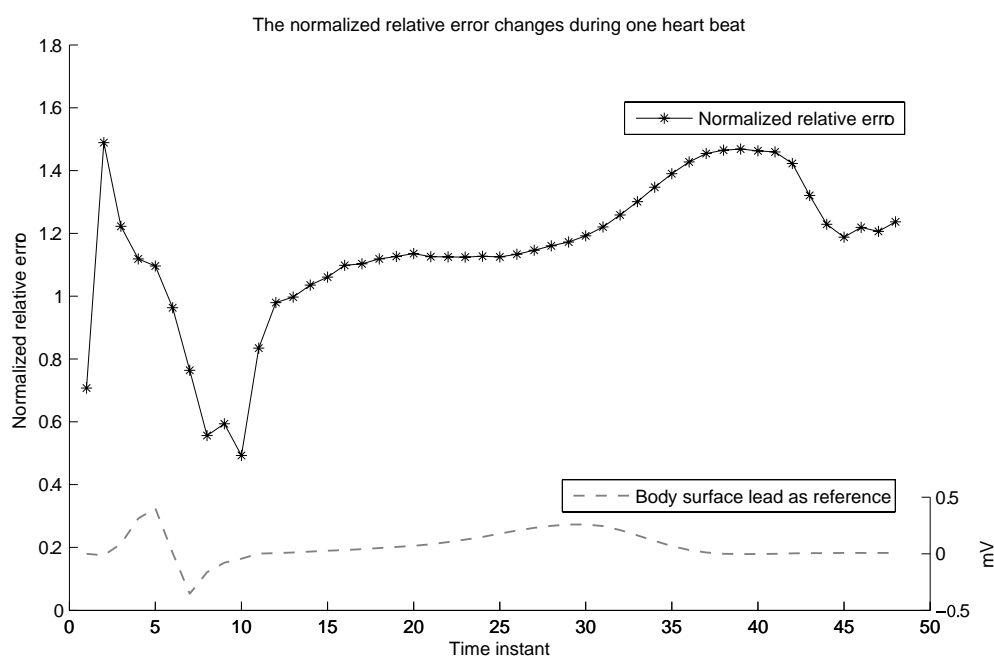


FIGURE 11.13: The normalized relative error during a whole heart beat for the ECGsim model and our reconstructions. The relative error can be quite high due to a non-perfect match between distributions. But if we take that into consideration, the normalized relative error is not extremely high, ranging from 50% to 150%.

Chapter 12

Regularization of the inverse problem

Until now, we have talked mainly about the forward problem of electrocardiography: computing body-surface potentials from heart-surface potentials. However, in practice we will not have heart-surface potentials, but can easily obtain body-surface potentials. Since cardiologists are mainly interested in heart-surface potentials, we actually want to compute those from body-surface potentials, the opposite of what we have been doing so far. This problem of reconstructing heart-surface potentials from body-surface potentials is called the *inverse problem of electrocardiography*.

As J.B. Keller explained [36], two problems are each others inverses if “the formulation of each involves all or part of the solution of the other”. Often, one problem is much more investigated than the other, since it is easier or more fundamental. This more investigated problem, called the direct problem, is physically oriented along a cause-effect sequence. Indeed, in our case the forward problem of electrocardiography follows the propagation laws of physics. The inverse problem, on the other hand, tries to determine the cause from the effect, as in our inverse problem of electrocardiography.

However, like many inverse problems, this inverse problem of electrocardiography is *ill-posed*, meaning that a small disturbance in the data can yield completely different reconstructions. More formally, when our forward problem is $\Phi_B = A\Phi_H$, we can compute one, and only one, solution to our algebraic inverse problem $\Phi_H = A^{-1}\Phi_B$, but this solution is physically unacceptable. Thus, small oscillating data produce large oscillating solutions; and since data are always noisy, our reconstructions are probably inaccurate. The physically acceptable solution we would like to obtain is actually the solution of an approximation of the problem.

However, the solutions to our approximated problem constitute a very broad spectrum of completely different solutions, for the same reason the problem exists: small changes in the approximated starting data will yield big changes in the solution. Thus, we need a criterion for selecting correct solutions.

An appealing approach for selecting a criterion is to let this criterion be inspired by physical laws. Indeed, when we know certain physical properties that the solution should exhibit, we can use these as criteria. For example, reconstructed heart-surface potentials will not have amplitudes of many million volts, so the amplitude of the potentials could serve as a criterion. Another criterion could take spatial continuity into account: we do not expect potentials to be completely different at two nearby locations. Thus, *a priori* information about the solution can serve as a criterion for *regularizing* the solution into the most realistic direction.

The idea behind regularization is to get the best solution out of the set of approximate solutions, depending on a parameter called the regularization parameter. One important property is that, when we have noise-free data, the family of approximate solutions should converge to the exact solution, when the regularization parameter tends to zero. When we have noisy data, as is the case in real world applications, an optimal approximation of the exact solution can be obtained for an optimal non-zero value of the regularization parameter [36]. *How* to select this optimal value for the regularization parameter can be a problem in itself and will also be discussed in the following sections.

12.1 The inverse problem is indeed ill-posed

Before diving into the different regularization techniques, we should check whether the inverse problem of electrocardiography is indeed ill-posed. In 1972 already, Martin and others showed that it is not feasible to determine heart-surface potentials from body-surface potentials by using unconstrained (that is, unregularized) solutions [37].

An example by Rudy et al. [25] shows the numerical problems associated with computations involving ill-conditioned matrices, such as the transfer matrix A . First of all, let us introduce a measure for the severity of the ill-conditioning based on the condition number of matrix. The *condition number* of a matrix is defined as the ratio between the largest eigenvalue of that matrix, and the smallest eigenvalue. The higher the condition number, the more ill-posed the problem is.

For example, a transfer matrix

$$A = \begin{pmatrix} 1.000 & 2.000 \\ 1.001 & 2.000 \end{pmatrix}$$

with the corresponding eigenvalues $\lambda_1 = 3$ and $\lambda_2 = 0.00067$, has condition number $\lambda_1/\lambda_2 = 4500$, which represents a moderately ill-conditioned system. Now assume that the real body-surface potentials are $\Phi_B^{real} = (5.000, 5.001)$, then applying the (non-regularized) inverse method yields the following real heart-surface potentials:

$$\Phi_H^{real} = A^{-1}\Phi_B^{real} = \begin{pmatrix} 1.000 \\ 2.000 \end{pmatrix}$$

But, due to noise, we will never measure the body-surface potentials exactly correct. Assume that the first electrode measures a 0.02% perturbed potential, such that the measured body-surface potentials equal $\Phi_B^{measured} = (4.999, 5.001)$. Then the resulting, inversely reconstructed, heart-surface potentials are:

$$\Phi_H^{measured} = A^{-1}\Phi_B^{measured} = \begin{pmatrix} 2.0000 \\ 1.4995 \end{pmatrix}$$

The heart-surface potentials reconstructed from the real body-surface potential thus differ drastically from the potentials reconstructed from only slightly different body-surface potentials.

While in this example, a 0.02% change in the input data results in a 25%-100% change in the output data, the matrix A was not that ill-conditioned, with a condition number of only 4500. However, our concentric spheres model, in its simple form, has a condition number of already 9000, the eccentric spheres model a condition number of 43000, and our more realistic ECGsim model has a condition number of 58000. Furthermore, real-world noise will be larger than 0.02%. Combined, this means that we will not be able to obtain realistic inverse reconstructions for real-world situations without imposing additional constraints.

Indeed, Figures 12.1 and 12.2 show that in our implementation, applying the inverse method $\Phi_H = A^{-1}\Phi_B$, without any regularization, is not sufficient to obtain realistic reconstructions. To simulate real-world circumstances, we added 10% additive white gaussian noise to the body-surface potentials that serve as input to our inverse method. The figures stress the need for regularization techniques to obtain a more realistic solution.

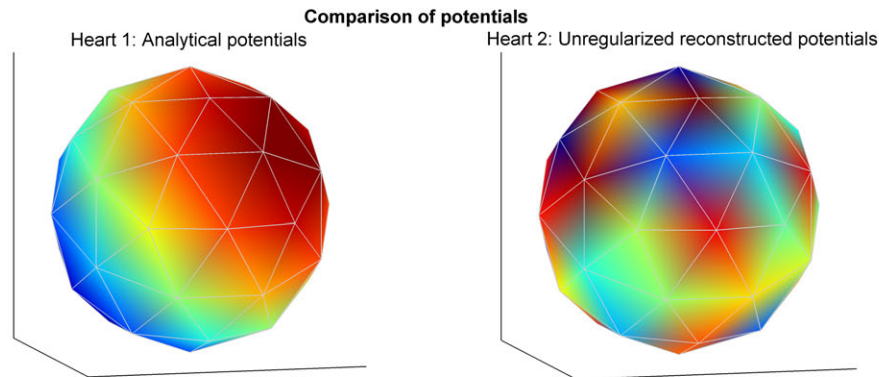


FIGURE 12.1: A comparison between the analytically known heart-surface potentials (left), and the inversely reconstructed heart-surface potentials (right) in the concentric spheres model. We applied the reconstruction $\Phi_H = A^{-1}\Phi_B$ without any regularization. A little noise (10%) was added to the analytically known body-surface potentials to simulate real-world noise. It can be seen that the reconstructed potentials do not fit the original potentials at all, due to the ill-posed nature of the inverse problem. This result stresses the need for regularization techniques.

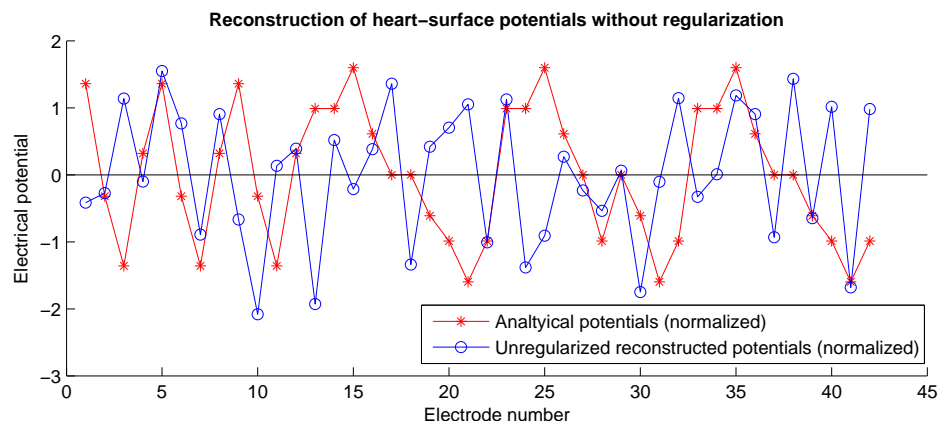


FIGURE 12.2: This figure shows even better that the inversely reconstructed, non-regularized potentials, even when normalized, do not fit the original distribution at all.

12.2 Selected regularization methods

Now that we have seen that our models are ill-posed and require regularization methods, we can look at specific types of those methods. The current implementation of Rudy's ECGI uses spatial [38] and temporal [39] regularization. For our implementation, we will focus on two types of spatial regularization. In other words, we will not take temporal regularization into account for now.

The first, and most widely accepted type of regularization is Tikhonov regularization [40]. This method rewrites the problem $\Phi_B = A\Phi_H$ as a linear least squares problem where we want to minimize the residual $\|A\Phi_H - \Phi_B\|^2$. However, only using the least squares method is not sufficient, because the matrix A is also ill-conditioned and the

solution to the least squares problem is not unique. An extra constraint involving the least squares solution $\|\Phi_H\|^2$ is added to minimize the norm of the solution, thus preferring “lower-valued” solutions.

The other method is based on the generalized minimal residual (GMRes) method. This method tries to prevent the smoothing that can result from Tikhonov regularization. It is an iterative method to find the solution to a system of linear equations, where again a residual is to be minimized. Where Tikhonov used the least squares residual of the problem, GMRes focuses on what potentials Φ_H are allowed in the solution to minimize this residual.

Both types of regularization will be discussed in more detail in the following sections. They share one problem, namely determining the optimal value for the regularization parameter, that in the Tikhonov method determines the weight of the constraint, and in the GMRes method determines the number of iterations. For both methods, the choice of the regularization parameter greatly influences the results, and a separate section is dedicated to this problem.

12.2.1 Tikhonov regularization

With Tikhonov regularization, the problem of solving an ill-posed system of linear equations $Ax = b$ is replaced by the following minimization problem:

$$x = \arg \min_x \left\{ \|Ax - b\|^2 + \lambda \|Rx\|^2 \right\} \quad (12.1)$$

for some suitably chosen regularization parameter $\lambda > 0$ and some suitably chosen *Tikhonov matrix* R . $\|\cdot\|$ denotes the Euclidian norm. The Tikhonov matrix R determines on what properties of x we actually impose a bound. When $R = I$ (the identity matrix), then we impose a bound on the amplitude of the solution, called a *zero-order Tikhonov regularization*. Taking $R = \nabla$ (the discretized gradient operator), we impose a bound on the amplitude of the first derivative of the solution, called *first-order Tikhonov regularization*. When $R = \Delta = \nabla^2$, the Laplace differential operator, then we impose a bound on the second derivative of the solution, not surprisingly called *second-order Tikhonov regularization*.

In other words, Tikhonov regularization tries to find x as a best fit to the least-squares solution to the inverse problem, but with an extra penalty on the norm of (a derivative of) the solution x . The weight of this extra penalty is determined by the regularization parameter λ .

The regularization parameter determines the trade-off between the “naive” least squares solution with *residual norm* $\|Ax - b\|^2$ and the weight of the penalty function on the *solution norm* $\|Rx\|^2$. A higher value for λ results in damping of the solution, which is necessary to restrict the drastically oscillating solutions in a realistic direction. However, with λ too high, too much damping is induced, and the fit to the given data b will not be proper. The resulting residual norm will be too large. If, on the other hand, λ is too small, too little regularization is imposed, and the solution will be dominated by the contributions from the data errors. The resulting solution norm will be too high.

Thus, the regularization parameter λ should be chosen such that a balance is found between the residual norm and the solution norm. This optimal value for λ depends on the given data b and cannot therefore be chosen equal for all applications. A separate section is devoted to the optimal choice of this regularization parameter.

When we have chosen an optimal λ , a direct solution to the Tikhonov minimization problem 12.1 is given by [25, 40]:

$$\begin{aligned} (A^T A + \lambda R^T R) x &= A^T b \\ x &= (A^T A + \lambda R^T R)^{-1} A^T b \end{aligned} \quad (12.2)$$

12.2.1.1 Applying Tikhonov to our case

Now, if we apply the Tikhonov theory to our problem, we would like to find a solution for $\Phi_B = A\Phi_H$ where we know Φ_B and want to obtain Φ_H . Then, applying the theory from above, we get [31]:

$$\Phi_H = \arg \min_{\Phi_H} \left\{ \|A^{-1}\Phi_H - \Phi_B\|^2 + \lambda \|R\Phi_H\|^2 \right\} \quad (12.3)$$

In this formulation, R is either:

- the unit matrix (Tikhonov zero-order); minimizing the absolute value of the potentials
- the surface gradient operator (Tikhonov first-order); minimizing the spatial derivative of the potentials. In other words, the curvature of the solution should not be too steep.
- the surface Laplacian operator (Tikhonov second-order); minimizing the second spatial derivative of the potentials. In other words, the potentials should not change too quickly in the spatial dimension.

All of the above characteristics are physical properties of heart-surface potentials, and therefore could serve as regularization penalty.

The first term of equation 12.3 represents the least-square solution of the inverse problem, based on the *residual norm* $\|A^{-1}\Phi_H - \Phi_B\|$. The second term imposes bounds on the amplitude of the solution (or one of its derivatives), the *solution norm* $\|R\Phi_H\|$. The value of λ controls the degree of the imposed constraint. When λ is small, the first term dominates, giving the least-squares solution priority. A larger value of λ makes the solution more constrained. The best choice for λ balances accuracy and stability of the solution.

The direct solution to problem 12.3, according to 12.2, is:

$$\Phi_H = (A^T A + \lambda R^T R)^{-1} A^T \Phi_B \quad (12.4)$$

This equation yields a regularized solution of the inverse problem, as long as we find an optimal value for the regularization parameter λ . The L-curve method is a method for obtaining an optimal value for this parameter and is described in a subsequent section. Essentially, we want to find the point where an increase in the residual norm (due to less regularization) is not satisfactorily accompanied by a substantial decrease in the solution norm.

Previous research has shown that, for the problem of electrocardiographic imaging, the specific choice for $R = I$, $R = \nabla$ or $R = \Delta$ does not have a large impact on the solution [25]. This is partly because the associated physical properties are consistent with each other; combining or changing the choice of R is therefore not likely to improve the results very much. However, more recent studies [34, 41] suggest that the choice may still have impact and further research is required in order to determine its importance for our data. For the current research, we will take $R = I$, applying Tikhonov zero order.

12.2.2 Generalized minimal residual regularization

The other regularization method we investigate is the generalized minimal residual (GMRes) method. Tikhonov regularization can sometimes reduce spatial resolution by smoothing and is dependent on a priori information of the solution characteristics. Ramanathan and others applied the GMRes method in order to by-pass these problems [38].

The iterative numerical method of GMRes has been successfully employed in solving ill-posed problems in the area of image-processing. The method does not impose constraints

and therefore does not require a priori information. However, we do need to make a suitable choice on when to stop the iteration of the method.

The properties of the GMRes method are quite different from those of the Tikhonov method. This makes it a suitable complementary (independent) method for obtaining inverse reconstructions. In other words, when both methods independently give similar results, this is a strong indication that the results are free of artifacts resulting from the ill-posed nature of the problem.

Let us again start with a linear system of equations $Ax = b$, but now with matrix A being square. Then we want to obtain x given A and b . Now define a *Krylov subspace* of order r as the linear subspace spanned by the images of b under the first r powers of A :

$$\mathcal{K}_r(A, b) = \text{span} \{b, Ab, A^2b, \dots, A^{r-1}b\}. \quad (12.5)$$

Then the GMRes method determines for an arbitrary value of $r \geq 1$ the solution $x_r \in \mathcal{K}_r(A, b)$, such that it satisfies

$$x_r = \arg \min_{x_r \in \mathcal{K}_r(A, b)} \|Ax_r - b\|$$

In other words, it approximates the solution by a vector x_r that is in the Krylov subspace and that minimizes the norm of the residual $Ax_r - b$ [42].

For more information about the algorithm that computes this projection of the inverse matrix, see [42, 43]. Basically, at iteration r , it applies the Arnoldi iteration to find an orthonormal basis of $\mathcal{K}_r(A, b)$, whose vectors are stored as columns in a matrix Q_r . The r^{th} reconstruction x_r then is a weighted combination of the vectors of this basis, written as $x_r = Q_r y_r$. The weights y_r are determined such that the residual $\|Ax_r - b\|$ is minimized. Or, more formally, the orthonormal basis matrix Q_r defines an upper Hessenberg matrix H_r by

$$H_r = Q_r^T A Q_r$$

which means that we can determine the residual $\|Ax_r - b\|$ according to

$$\|Ax_r - b\| = \|H_r y_r - b\|$$

Now, we have reduced the problem to finding the weights y_r such that the residual $\|H_r y_r - b\|$ is minimized. If the resulting residual is small enough, we can stop, otherwise, we continue with a new iteration [43].

Note that in this short explanation we have omitted a lot of details. More information can be found in the paper by Saad introducing the GMRes method [43]. The algorithm

we used implemented by Hansen et al. [44], who based his implementation on [42].

12.2.2.1 Applying GMRes to our case

Several practical issues have to be solved when we want to apply the above theory to our case. Our transfer matrix A is in general not square, as the number of body-surface electrodes usually is not equal to the number of reconstruction points on the heart-surface. We can overcome this problem by considering the problem $A^T \Phi_B = A^T A \Phi_H$, instead of using the problem $\Phi_B = A \Phi_H$. These problems are equal, but now $A^T A$ is square, which allows us to apply the GMRes method.

With each iteration of GMRes, the Krylov subspace is extended. With the number of iterations increasing, the subspace approaches the whole space, which means that amplified noise components start being included in the solution [38]. In other words, we need to stop the iterations at a suitable moment, such that the solution is stable with minimal contamination from amplified noise components.

Consider the upper Hessenberg matrix H_r at iteration r . This matrix reflects our current projection of the inverse of A into our Krylov subspace. With each iteration, this projection will result in a better fit, but it will also become more and more ill-conditioned. This is reflected by the condition number of H_r increasing when r becomes larger. On the other hand, with r increasing, the norm of the residual decreases. We could plot the condition number of H_r versus the logarithm of the norm of the r^{th} residual. Typically, as r increases, the increase in condition number is accompanied by a reasonable decrease in the norm of the residual. At a certain point, however, the residual error does not improve significantly, while the condition number keeps growing. The optimal value of the iteration number r can be found with the L-curve method, which also played a part in determining the optimal value for the Tikhonov regularization. This method will be explained in the next section.

12.3 The L-curve method for selecting optimal parameters

Almost all regularization methods involve a trade-off between the “size” of the regularized solution and the quality of the fit that it provides to the given data [40]. The difference between the methods is how these quantities are measured, and how the optimal trade-off is determined.

In Tikhonov regularization, we need to select the optimal value for the parameter λ that weights the solution norm, while in GMRes-based regularization, we need to find

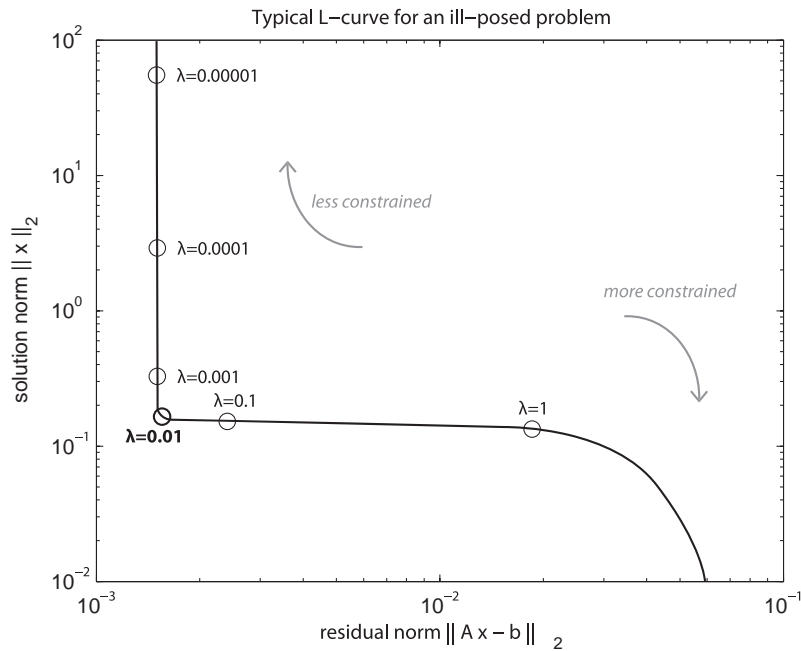


FIGURE 12.3: A generic L-curve for a Tikhonov regularization problem, where for a certain λ the corresponding residual norm and solution norm are plotted. Note that this representation uses log-log axes. The circles indicate the values for $\lambda = 10^{-5}, 10^{-4}, 10^{-3}, 10^{-2}, 10^{-1}$ and 1. A lower λ , which means going up the curve, represents less regularization or filtering. In the other direction, with λ increasing, more regularization is performed (at the cost of accuracy of the fit).

an optimal iteration number r . In both situations, these parameters define a trade-off between:

- the accuracy of the fit; reflected by the residual norm
- and the influence of the ill-posedness; reflected by either the solution norm in Tikhonov regularization, or by the condition number in the GMRes approach.

The accuracy should of course be as high as possible, but with as little influence of amplified noise components due to the ill-conditioned nature of the problem. In other words, we want to have the residual norm and the solution norm (or condition number) as low as possible, but lowering one will increase the other.

For Tikhonov regularization, the *L-curve* method was introduced for this problem [40]. Remember the Tikhonov regularization problem for a certain value of λ from equation 12.3. In this case, there is a trade-off between the norm of the residual $\|A^{-1}\Phi_{H,\lambda} - \Phi_B\|$, and the norm of the regularized solution $\|R\Phi_{H,\lambda}\|$. Note that we have included λ in the subscript of Φ_H to indicate that two norms are dependent of each other by the choice for λ .

We can plot those two quantities versus each other, as a curve

$$(\|A^{-1}\Phi_{H,\lambda} - \Phi_B\|, \|R\Phi_{H,\lambda}\|)$$

parametrized by λ . This is the definition of the L-curve; it is a tradeoff-curve between two quantities that both should be controlled. Figure 12.3 shows an example L-curve for a Tikhonov regularization problem. Note that it is customary to plot the two quantities in logarithmic scale, to further emphasize the abrupt corner in the curve.

This concave corner is the location of the optimal trade-off: when continuing to increase the regularization parameter λ here, the solution norm might still decrease a bit, but at a huge cost to the residual norm and thus less accuracy. On the other hand, if we make λ lower than the corner value, we drastically increase the solution norm (giving the ill-posedness a chance of influencing the solution), without decreasing the residual norm a lot.

Selecting the optimal value of the regularization parameter, the *L-curve criterion* is based on this idea of finding the apparent concave corner in the curve. Hansen [40] showed that when $Ax = b$ with b noisy, there always is (more or less) such a corner. He also describes a method to determine this corner. In a given curve, he searches for candidate corners, and then selects the corner with the maximum curvature. His algorithms are available in a Matlab toolbox, that were used in our implementation of this problem [45].

12.3.1 Applying the L-curve method to GMRes regularization

Until now, we have mainly talked about the L-curve method in the context of Tikhonov regularization. However, the problem of finding the optimal iteration number for the GMRes method is quite similar. In the GMRes method, the trade-off is between the norm of the residual $\|A^{-1}\Phi_{H,r} - \Phi_B\|$, and the condition number C_r of the upper Hessenberg matrix that approximates the inverse of our transfer matrix A . Thus, where in the normal L-curve method for Tikhonov regularization we used the norm of the solution, we now use another measure for the degree of ill-posedness, namely the condition number our reconstruction matrix.

Thus, at iteration r , we have two quantities: the norm of the residual $\|A^{-1}\Phi_{H,r} - \Phi_B\|$, and the condition number C_r . Note that these values now are dependent of the iteration number r instead of the weight λ in Tikhonov regularization. Again, we plot these quantities versus each other as a curve

$$(C_r, \|A^{-1}\Phi_{H,r} - \Phi_B\|)$$

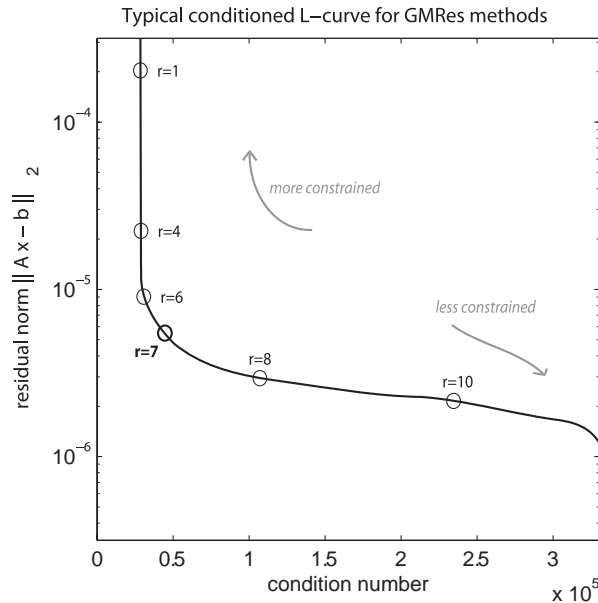


FIGURE 12.4: A generic conditioned L-curve for a GMRes regularization problem, where for a certain iteration r the corresponding residual norm and condition number are plotted. Note that this representation uses a logarithmic vertical axis. Note also the differences with Figure 12.3: the residual norm is now on the vertical axis; the condition number replaces the measure for ill-posedness (and is placed on the horizontal axis); and going down the curve now represents *less constraining* instead of more.

Note that we have switched the residual to the vertical axis, in contrast to its horizontal position in the case of Tikhonov. Also, while we took the 10-log of both the residual norm and the solution norm in the case of Tikhonov regularization, with the GMRes we only take the 10-log of the residual norm, and keep the condition number as it is. This adjusted version of the L-curve is introduced by Ramanathan et al. [38] for the problem of electrocardiography, and is referred to as the *conditioned L-curve*. Figure 12.4 shows an example of this conditioned L-curve. Especially note that in this case, increasing the regularization parameter r *decreases the amount of constraining*, while a increase of the regularization parameter λ in the Tikhonov case yields an *increase in the weight of the constraint*.

Ramanathan et al. showed that for their implementation of methods in electrocardiography, the GMRes method had a similar overall performance as Tikhonov regularization. However, in some of their cases, GMRes was able to recover local features better than Tikhonov reconstructions.

12.4 Implementation

The regularization methods as described above were implemented in our MATLAB[®] framework. Part of the methods for L-curve corner selection were readily available in the regularization toolbox by Hansen [45]. We adjusted their methods for corner-selection to also be able to find *conditioned L-curve* corners, as needed for the GMRes method. The GMRes method itself was also partly based on corresponding methods in their toolbox.

In the next chapter, we will compare the results for Tikhonov-based reconstructions, and GMRes-based reconstructions.

Chapter 13

Regularization experiments

In this chapter, the first inverse reconstructions will be calculated. The goal of the experiments discussed in this topic is mainly to investigate the possibilities and limitations of inverse reconstructions of heart-surface potentials from body-surface potentials.

As we have seen, unregularized solutions are not possible. We will compare the results of Tikhonov regularized solutions with those of GMRes regularized solutions. Where possible, we will compare the reconstructions with the original, known heart-surface potentials.

To simulate real-world circumstances, and to make sure that we correctly deal with the ill-conditioned problems associated with the reconstructions, we add noise to the body-surface potentials that we use as a starting point for our inverse method. For the concentric and eccentric case, 10% additive white gaussian noise (resulting in a signal-to-noise ratio of 10) was added to the body-surface potentials. This amount of noise is quite high, to make sure that we are in a realistic situation.

In the following sections, we will first briefly illustrate the results of the Tikhonov reconstructions, the L-curve, the GMRes reconstructions, and the conditioned L-curve. Then, we will compare the two regularization methods. We will end this chapter with a section of special experiments, to investigate the resolution and sensitivity of the methods.

13.1 Tikhonov reconstructions

We start with the concentric spheres model. We apply the Tikhonov method as described in the previous chapter, for various choices of λ . The corresponding normalized relative error between the reconstructed heart-surface potentials and the known heart-surface potentials is shown in Figure 13.1. We see that there is an optimal choice for

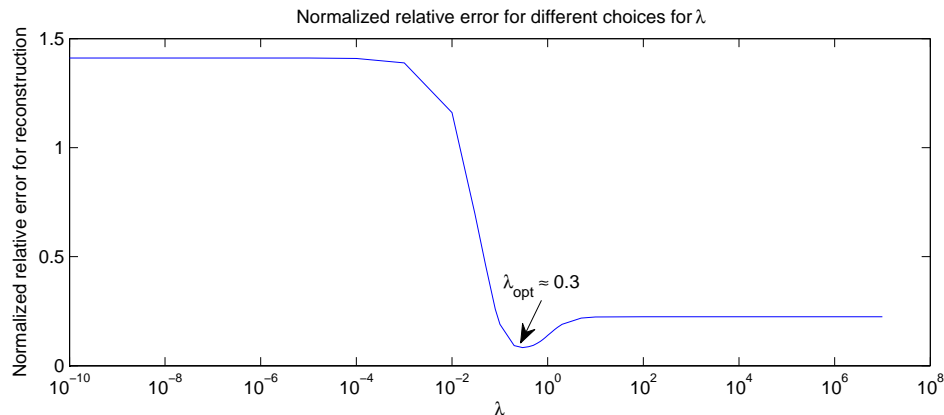


FIGURE 13.1: For each choice of λ , we used Tikhonov regularization to reconstruct the heart-surface potentials in the concentric spheres model based on the known body-surface potentials. The normalized relative error between these reconstructions and the known heart-surface potentials is computed for each choice of λ and shown here. It can be seen that there is an optimal reconstruction when $\lambda \approx 0.3$.

λ that minimizes the error. Choosing a lower λ results in a higher error due to too much influence of the amplified noise-components, while a higher λ results in too much smoothing. For the optimal value of $\lambda = 0.3$, we get a normalized relative error of $RE_{norm}(\lambda = 0.3) = 0.083$, which is very good.

When, for the same case, we apply the L-curve method for finding the optimal λ , we obtain the results of Figure 13.2. The L-curve method finds an optimal value for $\lambda = 0.1$. The normalized relative error for this is $RE_{norm}(\lambda = 0.1) = 0.191$, more than twice as high as with $\lambda = 0.3$. In other words, the value for λ we obtained with the L-curve still yields an accurate reconstruction, but a better one is possible. We should remember, however, that we obtained the optimal $\lambda = 0.3$ by using the *known heart-surface potentials* to compute the relative error. The L-curve method uses no known potentials (in a realistic situation, these would of course not be available), and thus has the built-in property that it is not able to check whether it selected the optimal value.

The reconstruction corresponding to the optimal parameter value found by the L-curve is shown in Figure 13.3. The reconstruction is very good: we can see the same pattern in the reconstruct potentials and in the known potentials. (Note that the scale of both distributions differs, however, we are not interested in absolute potentials.)

Results for the eccentric spheres case are similar and are not shown here, but will be discussed in the section where we compare Tikhonov reconstructions with GMRes reconstructions. We will, however, look more closely at the reconstructions in the ECGsim model, as we see some issues there. When we look at time-frame $t = 6$, for example, the L-curve has no distinct corner, as shown in Figure 13.4. This means, that there is no clear method of selecting an optimal λ . In other words, Tikhonov regularization is

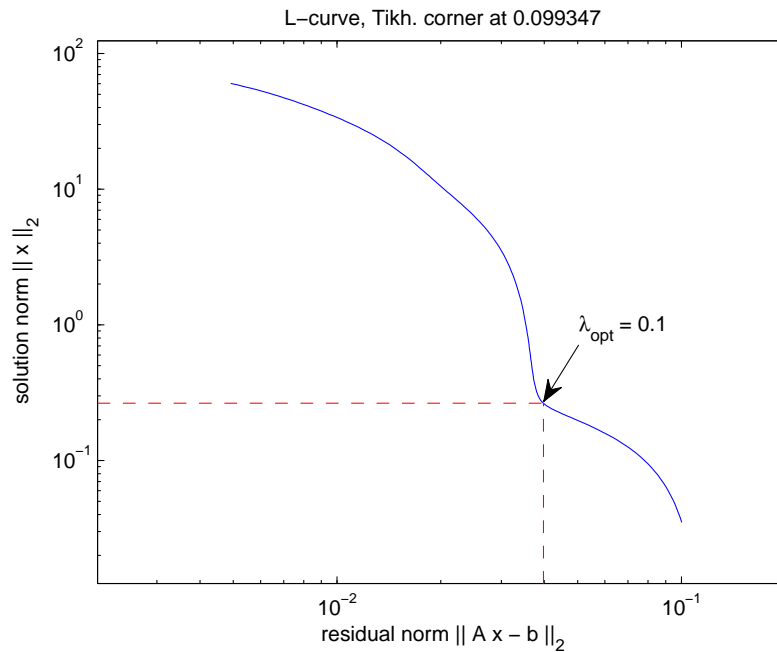


FIGURE 13.2: The L-curve method applied to find the optimal value for λ . On the horizontal axis, the residual norm (the mismatch of the fit) is shown, and on the vertical axis the corresponding solution norm (representing the ill-posed artifacts), both for a certain value of λ . The optimal value for λ is found at the concave corner, indicating the value with an optimal trade-off between accuracy and artifacts due to the ill-conditioned problems.

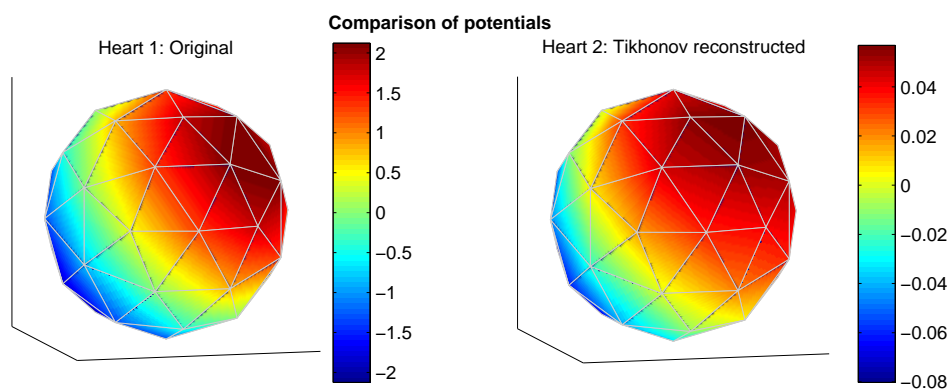


FIGURE 13.3: Original (known) heart-surface potentials (left) versus Tikhonov reconstructed potentials (right), with the optimal value for λ selected by the L-curve method. The reconstruction closely resembles the original potentials.

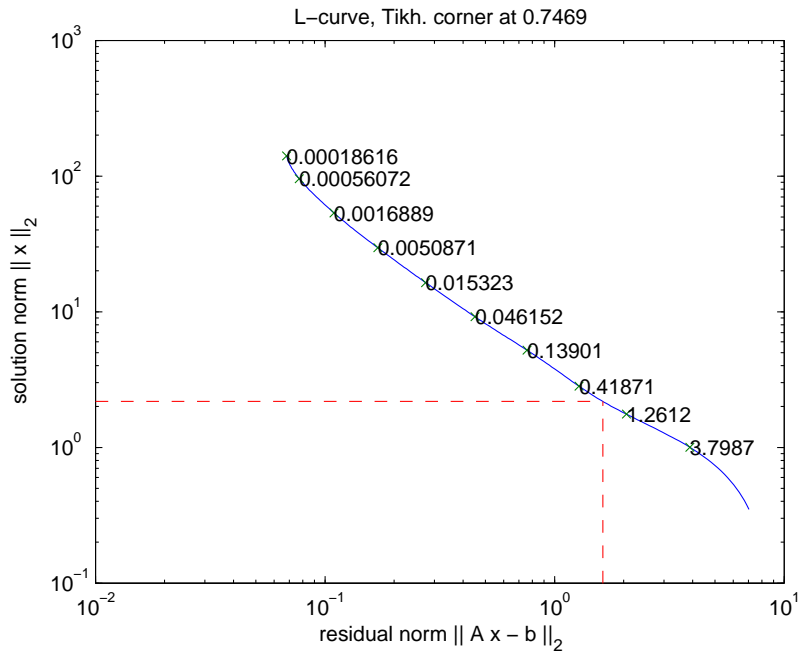


FIGURE 13.4: The L-curve for the ECGsim model at $t = 6$. This curve has no clear concave corner, which makes it difficult to select an optimal λ .

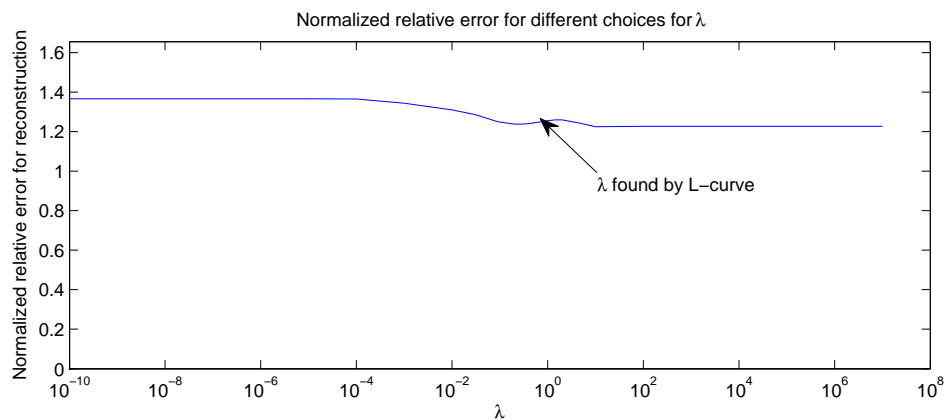


FIGURE 13.5: The normalized relative error for Tikhonov reconstructions, depending on the chosen value for λ . It can be seen that, whatever the choice for λ , the error never gets really low. In other words, Tikhonov regularization cannot find a good fit here, with the given transfer matrix A . This could explain why there is no typical “L-shaped corner” in the L-curve plot of Figure 13.4.

not able to find a good fit here. This is backed-up by the plot of the normalized relative error in Figure 13.5, which shows that, for all λ , no distinct optimal value can be found, as the error always stays relatively high.

Similar results were obtained for other time-instants. This means, that in this more complex case, we are not able to find a fit that gives a low normalized relative error. However, we still might get patterns that indicate the most important physiological properties. For example, Figure 13.6 a Tikhonov reconstruction for the ECGsim model,

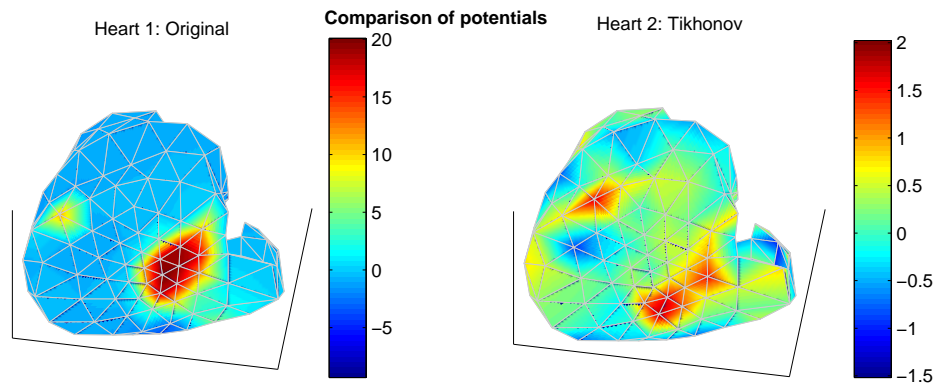


FIGURE 13.6: Although not perfect, we can see some similarities between the original heart-potential distribution (left) and the Tikhonov-based reconstruction (right).

where we can see two maxima in both the original and the reconstructed distribution. However, in many other cases, reconstructions and original patterns seem harder to match.

This suggests that Tikhonov regularization is unable to find a good match here. This can be due to limitations of the Tikhonov method, but also more fundamentally, a transfer matrix A that does not incorporate enough details on the complex geometry. Another issue here might be the fact, that the ECGsim model provides us with data that is simulated itself, with an unknown quality. In other words, perhaps we are trying to reconstruct false data. This will be further explained in section 13.3.

13.2 GMRes reconstructions

For the GMRes-based reconstructions, we also computed the normalized relative error for various choices of the regularization parameter, in this case the number of iterations r . For the concentric-spheres case, the results are shown in Figure 13.7. It can be seen that the lowest error is obtained when the number of iterations is $r = 2$, with a normalized relative error of $RE_{norm}(r = 2) = 0.068$, which is a good reconstruction.

Figure 13.8 shows the use of the conditioned L-curve method to find the optimal value for r in a situation where we do not have original heart-surface potentials to compare with. The L-curve method returns $r = 2$ as the optimal number of iterations, exactly at the real optimum which we determined from the previous plot. If we inspect the resulting distribution in Figure 13.9, we see that the reconstructed distribution is a perfect fit. In other words, in this case, GMRes finds a very nice fit, with the conditioned L-curve method finding the optimal regularization parameter r .

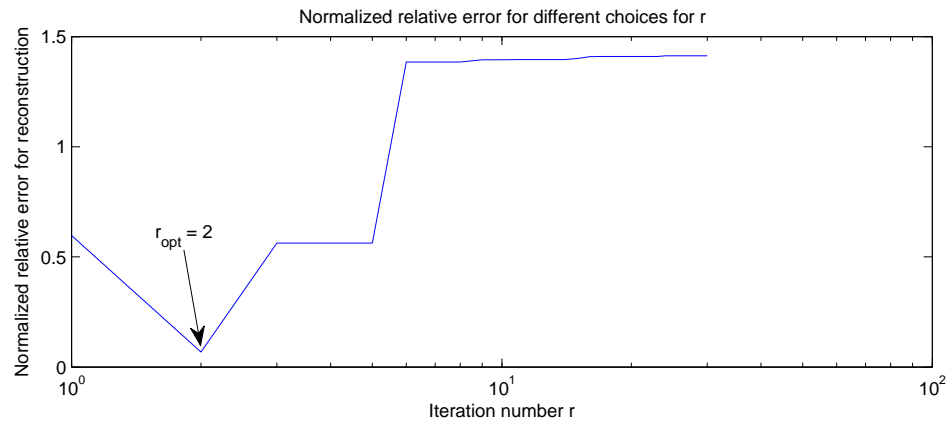


FIGURE 13.7: For each choice of r , we used GMRes regularization to reconstruct the heart-surface potentials in the concentric spheres model. The normalized relative error between these reconstructions and the known heart-surface potentials is computed for each choice of r and shown here. It can be seen that there is an optimal reconstruction when $r = 2$.

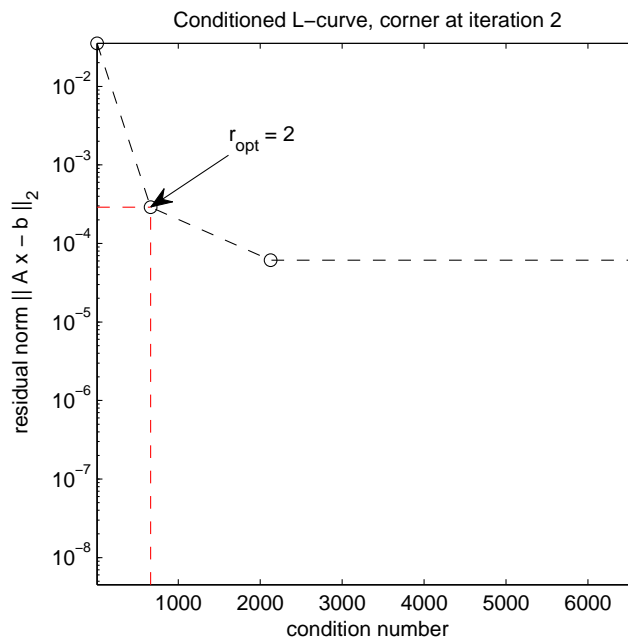


FIGURE 13.8: The L-curve method for finding the optimal value for r in the GMRes case. Now, on the vertical axis, the residual norm (the mismatch of the fit) is shown, and on the horizontal axis the corresponding condition number (representing the ill-posed artifacts), both for a certain value of the iteration number r . The optimal value for r is found at the concave corner, indicating the value with an optimal trade-off between accuracy and artifacts due to the ill-conditioned problems.

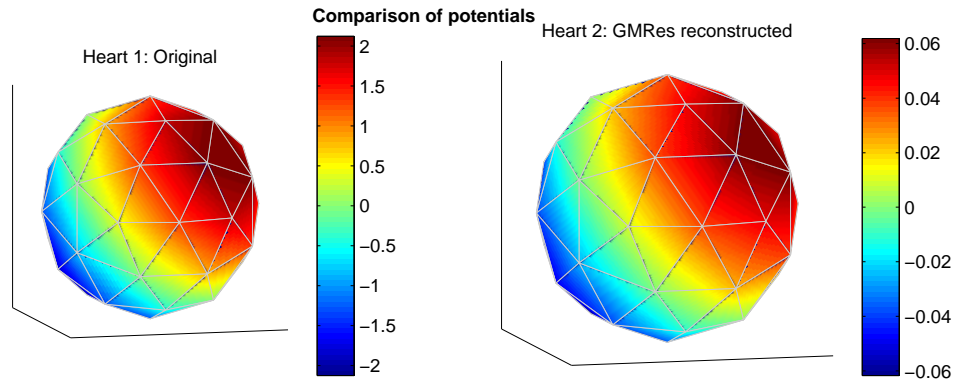


FIGURE 13.9: Original (known) heart-surface potentials (left) versus GMRes reconstructed potentials (right), with the optimal value for r selected by the conditioned L-curve method. The reconstruction fits the original potentials accurately.

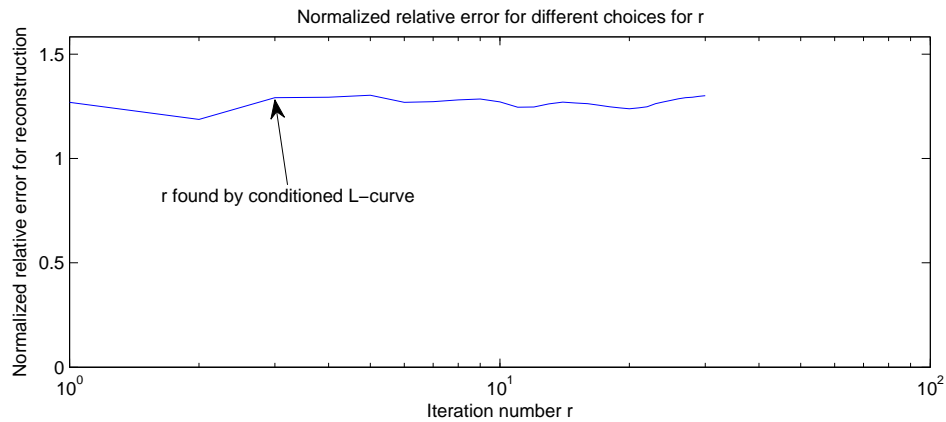


FIGURE 13.10: When we try to reconstruct heart-surface potentials with the GMRes-regularized method, we never obtain a fit that has a low normalized relative error.

For the eccentric spheres model, we found similar results, not shown here. If we look at a specific time-instant ($t = 6$, but similar results for other instants) at the GMRes reconstructions for the ECGsim model, we see, similar to the corresponding Tikhonov reconstructions, that the method is not able to achieve a good fit, as the plot of the normalized relative error in Figure 13.10 shows: the error always stays relatively high.

The conditioned L-curve method finds a quite distinct corner, however, at $r = 3$ iterations, see Figure 13.11. The corresponding reconstruction, unfortunately, is not that good, as shown in Figure 13.9.

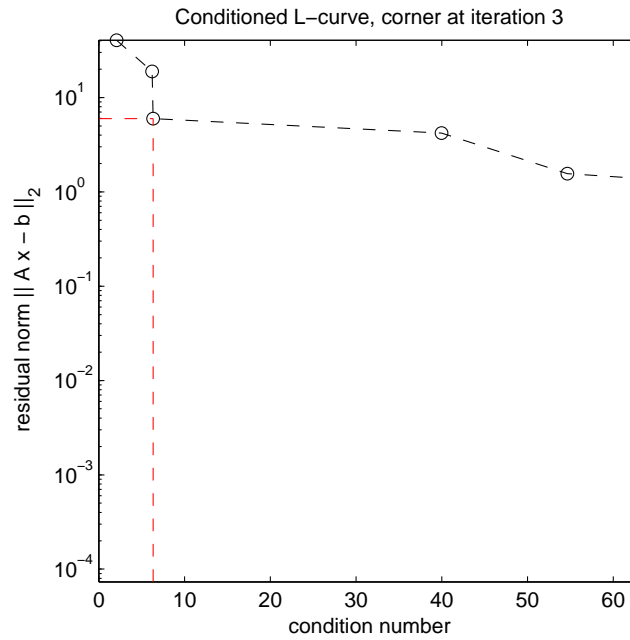


FIGURE 13.11: The conditioned L-curve method finds the optimal iteration at $r = 3$ for the ECGsim model.

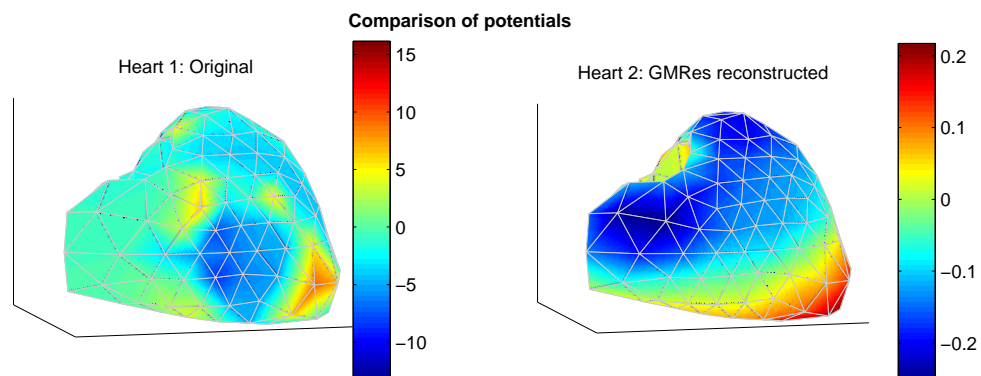


FIGURE 13.12: Original (known) heart-surface potentials (left) versus GMRes reconstructed potentials (right), with the optimal value for r selected by the conditioned L-curve method. The reconstruction does not fit the original potentials.

13.3 Reasons underlying the inability to reconstruct ECGsim model data

Both the GMRes reconstruction and the Tikhonov reconstruction yield very good results for our sphere models. However, in the ECGsim model, both methods are unable to reconstruct the heart-surface potentials to a satisfactory level, for any choice of the regularization parameter. The mismatch in the ECGsim case could be due to several reasons:

- The transfer matrix is not constructed correctly. It might be the case that the scaling defect, mentioned in chapter 11, has a higher influence in more complex cases. On the other hand: forward reconstructed body-surface potentials seemed to fit the known body-surface potentials accurately, suggesting that the transfer matrix is more or less correct.
- The regularization methods are not able to yield a correct solution due to built-in limitations. This could be the case, although in literature, both regularization methods have been shown to be able to yield correct reconstructions.
- The geometry is not suitable for our methods. The geometry is somewhat unusual, since the inner portions (endocardium) of the heart are also used as heart surface. This might not be a correct representation. In the literature, a closed surface is generally employed, without any inward folds.
- The given heart-surface potentials in the ECGsim model are not correct, and do not correspond to the given body-surface potentials that we use as starting point for our reconstructions. Some investigation points in this direction. In particular, when we compute the body-surface potentials ourselves, with our forward method, and use those to reconstruct the heart-surface potentials with the GMRes or Tikhonov method with 1% additional noise, we obtain a perfect fit.

The last cause seems the most plausible: the heart-surface potentials given with the model, do not correspond well to the given body-surface potentials. Indeed, if we use the forward method to compute body-surface potentials ourselves, add 1 or 2% additive white gaussian noise, and apply either GMRes or Tikhonov regularization, we obtain perfect fits. For the Tikhonov method, Figure 13.13 shows the L-curve, the mismatch error for each λ , and the reconstruction for the automatically selected λ . Figure 13.14 shows the same plots for the GMRes method. In both Figures, we see a good reconstruction. However, in Tikhonov we used 2% additive noise, while in GMRes only 1%, because 2% in the latter case did not yield very good results. We investigate the noise dependency of both reconstruction methods further in a subsequent section, but at least we have shown now that also in the complex ECGsim model, we are able to reconstruct heart-surface potentials.

13.4 Detection of maxima

In this and the following sections, we will investigate some special cases and the corresponding resolving capacity of our regularization methods. For most of the cases, we will

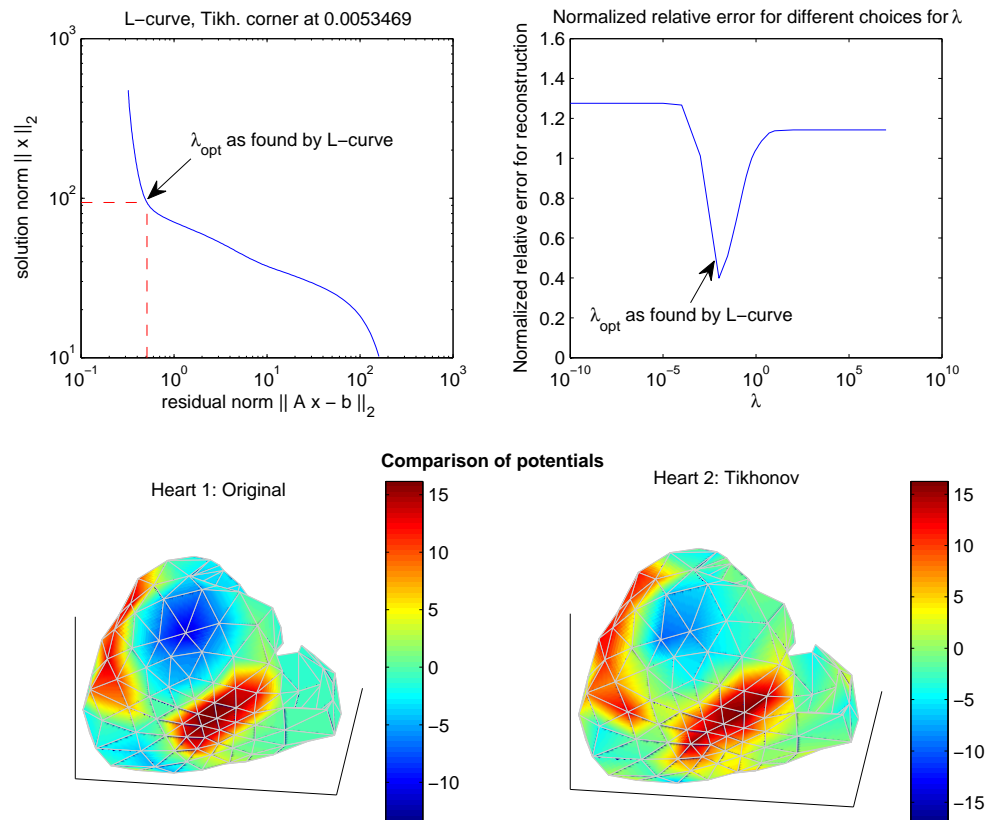


FIGURE 13.13: When we use our forwardly computed body-surface potentials as a starting point for reconstruction in the ECGsim model, we see that the Tikhonov method is able find a good reconstruction. The L-curve (top left) shows a distinct corner, which also corresponds to the optimal λ in the plot of the normalized relative errors for various choices of that parameter (top right). The corresponding reconstruction is shown below and shows a nice fit.

define a heart-surface potential distribution manually, and then check the possibilities of reconstruction.

The first case we will investigate is detection of maxima: how well can we reconstruct a single maximum on the heart-surface? We will investigate this in the eccentric spheres model, see Figure 13.15. This model simulates the realistic situation the best, without using the less reliable ECGsim model. Note that we have generated spheres with more detail (more vertices and surface elements) than in the previous experiments, to be able to investigate the spatial resolution capacities to the fullest.

We start with a heart-surface with a constant potential of zero. One vertex is given a potential of 1, and its direct neighbors a potential of 0.5. With the forward method we compute the corresponding potential distribution at the body surface. Some noise (1%) is added to these potentials to ensure realistic circumstances. Using the GMRes and Tikhonov methods, we reconstruct the heart-surface potentials. We repeat this

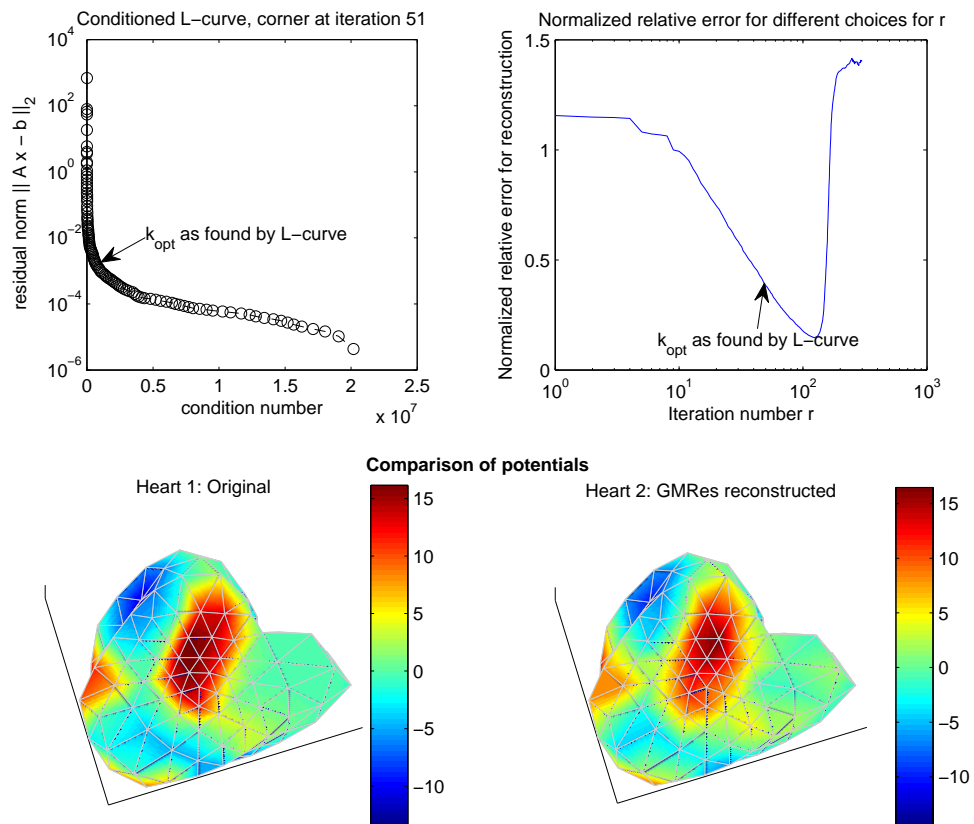


FIGURE 13.14: Same as Figure 13.13, but now for GMRes reconstruction. Again, a clear corner is found (top left), but the higher iteration number could actually give somewhat better results (top right). Nevertheless, important features are still visible in the reconstruction (bottom).

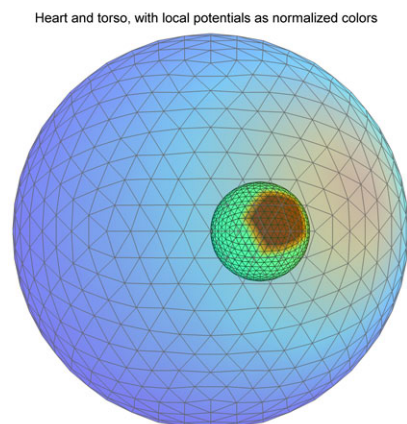


FIGURE 13.15: The eccentric spheres model used for some experiments. Note that this model is the same as the previous eccentric spheres model, but more detailed. In this model, both heart and body have 642 vertices and 1280 triangulated surface elements.

process for increasing sizes of area of high potential, to investigate the resolution of the reconstructions.

The results are shown in Figure 13.16. The figure shows for each case the original heart-surface potential distribution (left), and the reconstructed distributions. For each reconstruction, the corresponding normalized relative error is given.

Even with a small area of maximal potentials, we find a corresponding maximal area in the reconstruction, with the same location (top row). However, the reconstructed area is much too large: the reconstructed maximum includes a large part of the zero-valued area surrounding the original maximal area. This is also reflected by the high relative error. When we increase the original area of potentials, the reconstructed area remains too large, until row 4, where the reconstructed area matches the original area. As from row 5, the reconstructed area of maximal potentials nicely grows with the original area of maximal potentials.

Thus, the location of the maximum is always found exactly in this model. However, with only a small maximum (and no other significant potentials on the surface), the reconstructed area of high potentials is too large. This indicates that the spatial resolution of the reconstruction methods is not very good in their current implementation.

But, how then do we explain the very nice results we got from the ECGsim model, when we also used the forwardly computed potentials as a basis for reconstruction, as shown in Figure 13.14 for GMRes reconstructed potentials, and Figure 13.13 for Tikhonov reconstruct potentials? Indeed, in these figures, we see several maxima (and minima), and the reconstruction clearly matches those.

It appears that the amount of noise is the significant factor here. For example, if we repeat the procedure with the first row of Figure 13.16, but now with 10 times less noise added to the body-surface potentials, we obtain Figure 13.17. This figure clearly shows an almost perfect reconstruction, where in the previous case we got the worst results here. Apparently, the amount of noise that is present is a major determinant of the spatial quality of reconstruction.

13.5 Detection of several maxima

We can also investigate the spatial resolution capabilities of the reconstruction methods by starting with two maxima, slowly moving away from each other. When the two maxima are very close to each other, they will be reconstructed as a single maximum.

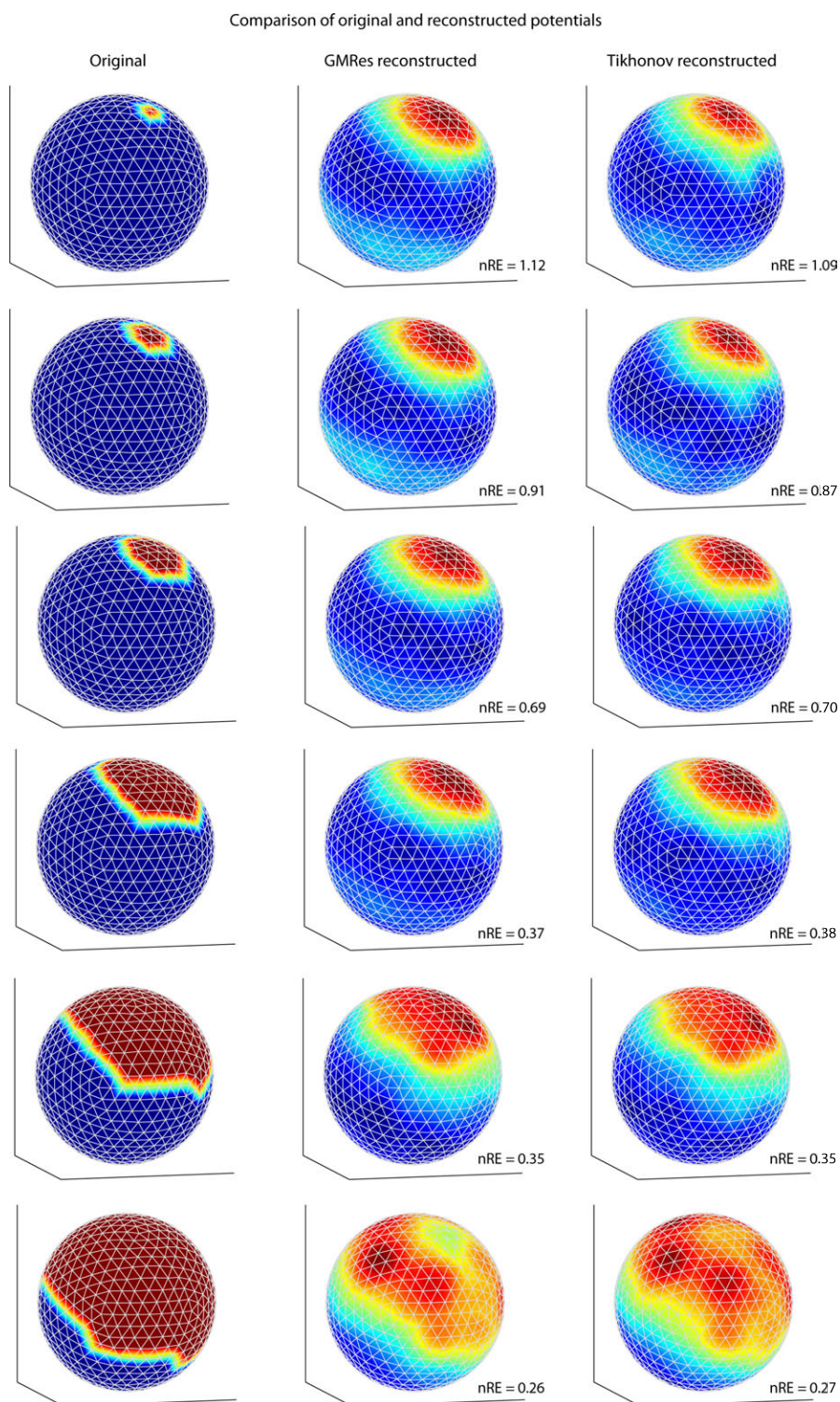


FIGURE 13.16: Results from reconstruction of heart-surface potentials with one original maximum. Left: the original heart-surface potential distribution. Middle: GMRes reconstructed potentials, with the regularization parameter automatically selected by the conditioned L-curve method. Right: Tikhonov reconstructed potentials, also with automatic parameter selection.

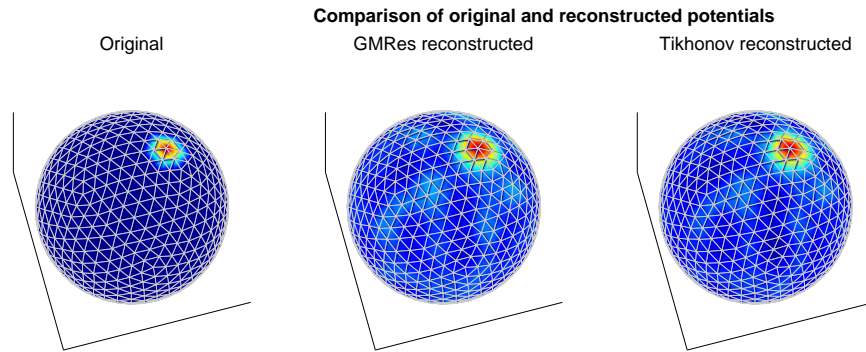


FIGURE 13.17: Same as the first row of Figure 13.16, but now with 10 times less noise added to the body-surface potentials.

As soon as the two maxima are reconstructed separately, we have found the maximum resolution of the reconstruction methods.

Figure 13.18 shows the results for these experiments. We have performed the experiments for two different noise levels. It can be seen that when a considerable amount of noise is added (top three rows), the reconstructed distribution always has a single maximum. The reconstructed maximum gets broader when the underlying maxima are further away, but only a single maximum can be observed.

With a 10-fold lower noise level of the body-surface potentials, the reconstructions are much better (bottom three rows). When the maxima are very close (first row), both reconstruction methods are not able to reconstruct two distinct maxima, but moving a bit further away yields two separate maxima in the reconstruction (second row).

13.6 Summarizing the first results

We have seen now, that we are able to reconstruct heart-surface potentials from (analytically known, or forwardly computed) body-surface potentials and a given geometry. We have provided a proof of concept of the idea that it is possible to reconstruct electrical heart activity from electrical measurements at the body surface. Both Tikhonov reconstructions and GMRes reconstructions yield valid results.

Furthermore, from these results, we see that noise has a significant impact on the reconstruction capacity of the algorithms. The spatial resolution of the reconstruction depends heavily on the amount of noise present, and the ability of the regularization methods to deal with this noise.

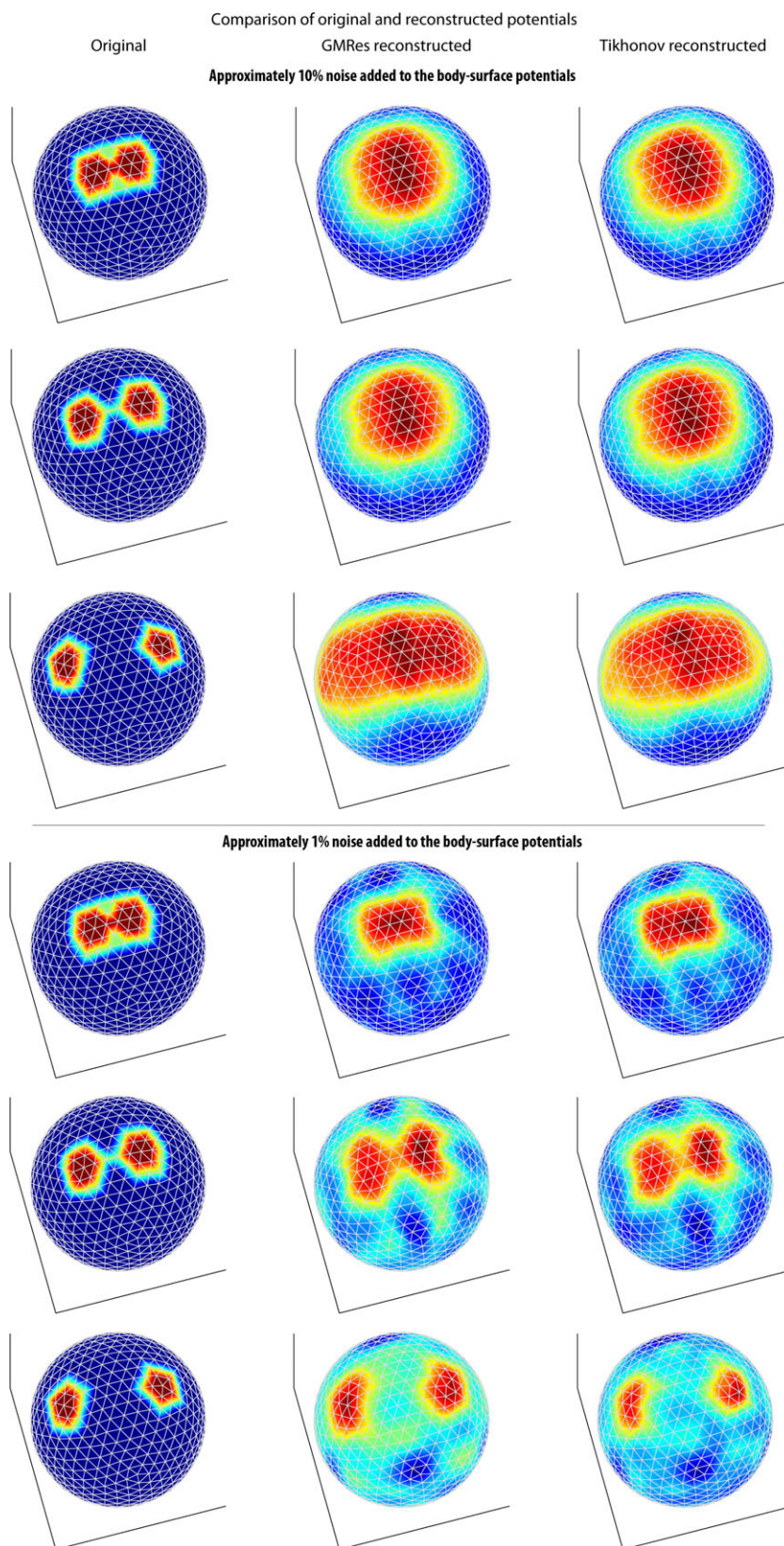


FIGURE 13.18: Results from reconstruction of heart-surface potentials with two maxima moving away from each other. In the three top rows, we added approximately 10% noise to the body-surface potentials, in the other three rows only 1%. Optimal values for the regularization parameters are automatically selected.

Another important result is the fact that in almost all situations, both the GMRes method and the Tikhonov method yield similar reconstructions. This has two implications:

1. We did not find any evidence for the “reduced-smoothing” property that GMRes is supposed to have. Both Tikhonov and GMRes seem to smooth the result by the same amount. For example, we would expect to see the two maxima reconstructed earlier with GMRes than with Tikhonov methods, but could not find such a result.
2. Since both regularization methods are based on very different ideas and methods, the fact that they generate similar results is an indication for the validity of the methods and of the implementation. This is a very important result, as it strengthens our confidence in the framework.

Now we know that, although noise is limiting factor, we are able to correctly reconstruct heart-surface potentials. The next step is to investigate uncertainty in the geometrical properties. In other words, how exact do we need to know the geometry to correctly reconstruct heart-surface potentials?

13.7 Sensitivity to translation errors

Our transfer matrix is based on the geometry and location of the heart and body. We can determine this shape and location from a non-specific, average human anatomy, but also more patient-specific with the use of Computed Tomography (CT) or Magnetic Resonance Imaging (MRI), as explained in chapter 6. Although CT and MRI are more accurate than a predefined, non-specific anatomy, they still have their limitations.

In this section, we will investigate how well we are able to reconstruct heart-surface potentials, if our transfer matrix is based on a certain assumed geometry, but the real geometry actually differs a little. We investigate this in the eccentric spheres model. Again, we will be using the detailed model of eccentric spheres. The computationally more demanding transfer matrix computations are compensated for by the more detailed analyses they allow.

We start with a certain “known geometry” and a given heart-surface potential distribution with two maxima, as in Figure 13.19. Using the corresponding “real” transfer matrix, we will compute the body-surface potentials, to which a little noise (1%) will be added for realistic circumstances. Next, we will reconstruct the heart-surface potentials while assuming an inaccurate geometry and a corresponding “faulty” transfer matrix.

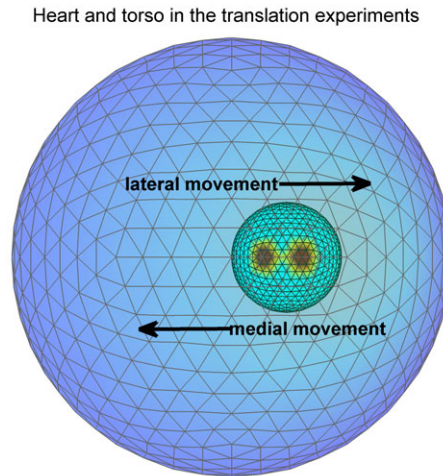


FIGURE 13.19: The geometry and heart-surface potential distribution used in the translation experiments. The assumed heart lies either lateral or medial from the actual (shown) heart location.

The reconstructed heart-surface potentials are then compared to the original potentials to determine the sensitivity of the reconstructions to errors in geometry assumptions.

The first geometrical error we will investigate is translation: what if we think that the heart is positioned at a location slightly moved from its actual position? So far, in the eccentric sphere model, the heart has been placed at a distance $1/4$ of the radius from the center of the body sphere. Figure 13.20 shows the reconstructions for a movement of 5%, 10%, 20% and 50% in the lateral (outside) direction, and for a movement of 5%, 10%, 20% and 50% closer to the body sphere center.

Panel A of this figure shows the original heart-surface distribution (left), which we gave two maxima. The corresponding body-surface potentials were calculated and a little noise was added for realism. Next, using the same geometry and corresponding transfer matrix, we reconstructed the heart-surface potentials with the GMRes methods (middle) and Tikhonov methods (right), as a reference for our next reconstructions.

In panel B, the heart sphere was progressively moved in medial (inward) direction by 5%, 10%, 20% and 50%. This new geometry was assumed to be the correct geometry. This assumed geometry was then used to generate the corresponding “faulty” transfer matrix. We used the body-surface potentials (forwardly computed with the “correct” transfer matrix) and the “faulty” transfer matrix based on the deviated geometry to reconstruct our heart-surface potentials with GMRes (left column) or Tikhonov methods (right column). We see that with a 5% deviation, the reconstruction still yields two distinct maxima at the correct location. In other words, at this (low) noise level, we are able to compensate for a small uncertainty in the geometry. This holds for the case with

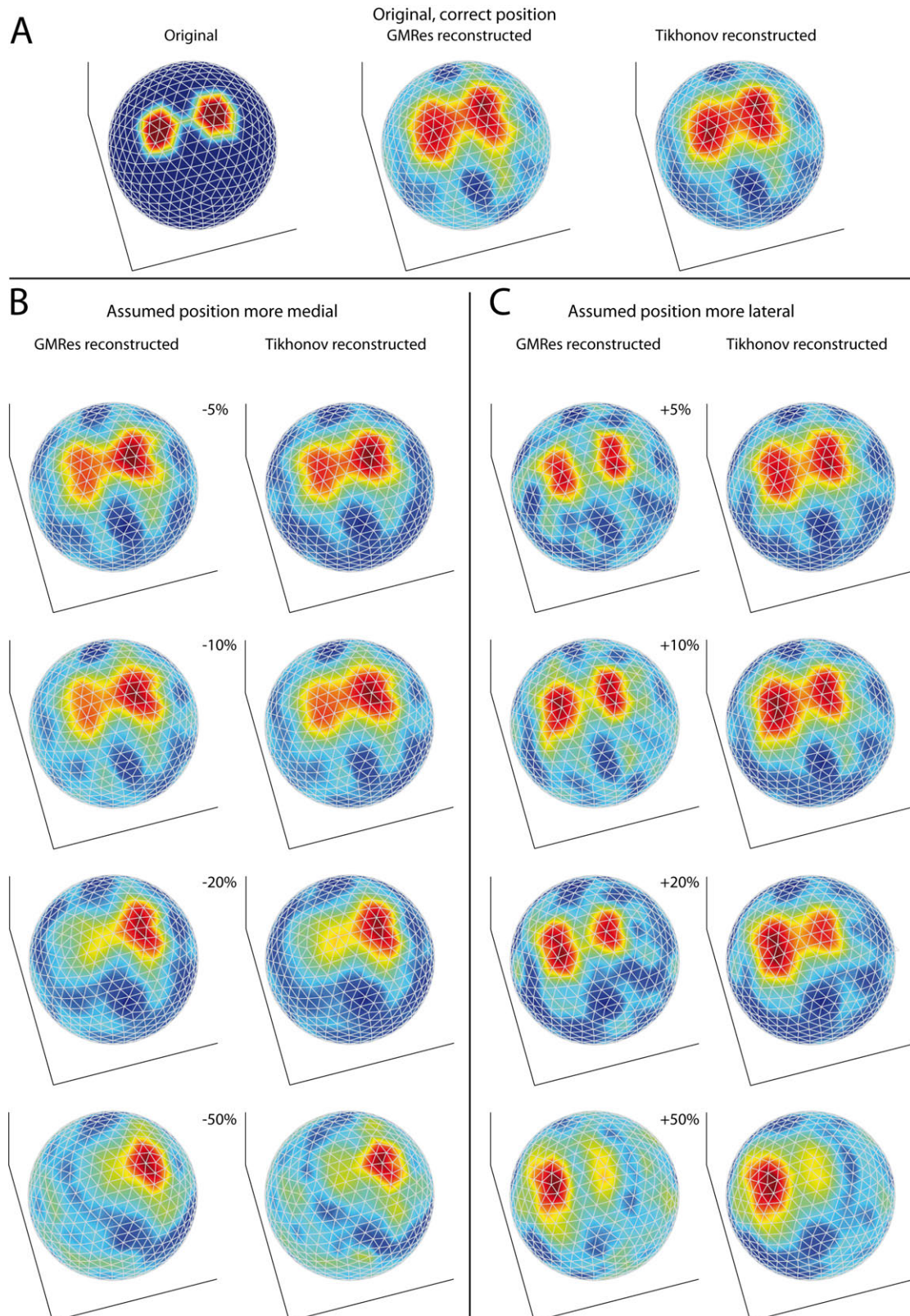


FIGURE 13.20: Results from reconstruction of heart-surface potentials with two maxima, when the assumed geometry differs from the real geometry. Panel A shows the original heart-surface distribution with two maxima (left), and the reconstructed potentials (middle and right). Panels B and C show the reconstructions where we assumed a geometry that deviated in medial or lateral directions, respectively.

10% deviation, although now we already see that the two maxima are merging. As of a deviation of 20%, we see that one maximum disappears, and the other moves in the direction of the location of the “real” heart (in this image to the right).

A similar story holds for panel C, where we assumed the heart to be located in a direction more lateral (outward) than its true position. With a 5% movement in the lateral direction, two distinct maxima are reconstructed, although GMRes seems to do a better job here than Tikhonov. This difference is even more distinct in the cases with 10% and 20% movement, where GMRes is still able to find two distinct maxima, and Tikhonov shows an area that is merging to one maximum. At 50%, even GMRes cannot reconstruct the other maximum properly anymore, and both reconstructions seem to have their maximum moved in the direction of the original heart location.

From panels B and C, we can conclude that with only a little deviation (and little noise), we are able to reconstruct the maxima distinctly and at their correct position. The more the actual geometry differs from the assumed geometry, however, the more difficult it becomes to reconstruct two separate maxima. We see that GMRes yields better reconstructions, at least in the lateral cases.

13.8 Sensitivity to size errors

We can repeat the same procedure as in the previous section, but now for size errors. Again, we take the same eccentric geometry, and now we vary the size of our “assumed” heart.

While doing these experiments, we saw that Tikhonov at a certain moment produces nonsense, whereas GMRes still generates useful data. Some investigation pointed out that in these situations, the L-curve has two corners, of which the wrong one was selected by the L-curve algorithm. The regularization parameter belonging to the other corner always gave better results, similar to those of GMRes. In the following results, we always selected the correct corner manually if necessary.

Figure 13.21 shows the results for varying heart sizes. In panel A, we used a heart-surface potential distribution with two maxima, and the “correct” transfer matrix, to compute the actual body-surface potentials. A little noise was added to these body-surface potentials. These body-surface potentials were used in all next experiments to reconstruct heart-surface potentials with an erroneous geometry. For reference, we used the correct transfer matrix with the GMRes (middle) and Tikhonov methods to reconstruct the heart-surface potentials in panel A.

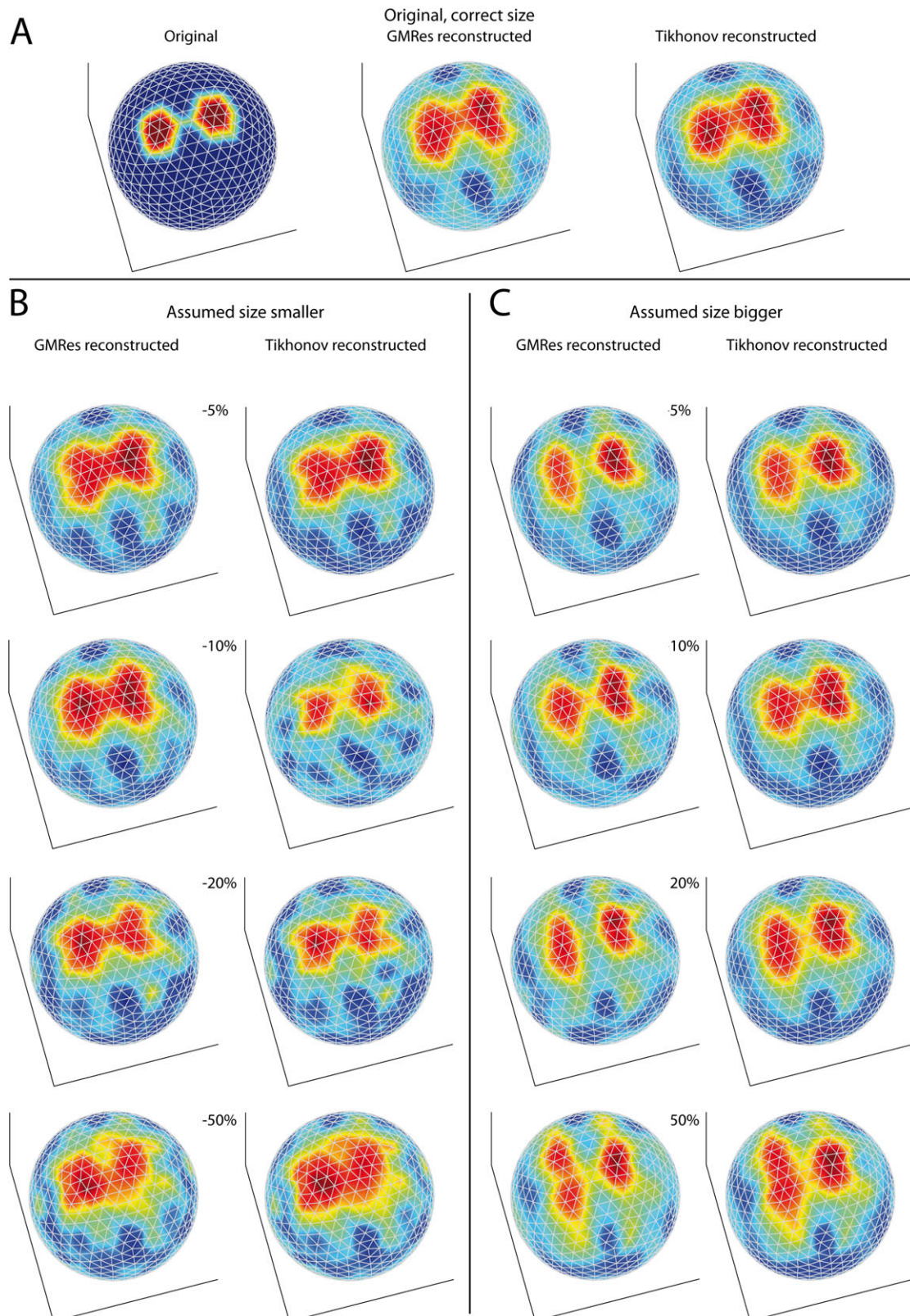


FIGURE 13.21: Results from reconstruction of heart-surface potentials with two maxima, when the assumed geometry differs from the real geometry. Panel A shows the original heart-surface distribution with two maxima (left), and the reconstructed potentials (middle and right). Panels B and C show the reconstructions where we assumed the heart to be smaller or larger, respectively.

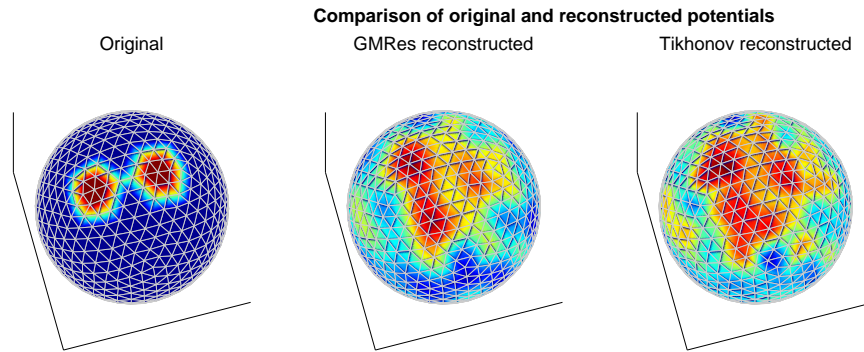


FIGURE 13.22: Reconstructions with GMRes and Tikhonov, where we assumed the heart to be twice as big as its actual size.

In panel B, we used a “erroneous” geometry, in which we assumed the heart to be smaller than its actual size, by 5%, 10%, 20% and 50%. The corresponding “faulty” transfer matrices were used to reconstruct heart-surface potentials with either the GMRes method (left column) or Tikhonov method (right column). Panel C shows similar results for a heart bigger than its actual size.

From panels B and C, we see that a little deviation in heart size does not directly induce any significant reconstruction errors. Only with deviations of -50% or +50% we see a mismatch. Out of interest, we performed the same experiment for a deviation of 100%, that is, an assumed heart size of twice the actual size. The results are shown in Figure 13.22. Now we can indeed say that the reconstruction shows little resemblance with the original distribution, although the resulting maximal area is at the correct location.

This leads us to the conclusion that some deviation in heart size still yields acceptable results; at the very least, location (translation) uncertainty, as investigated in the previous section, has a much higher impact than size uncertainty.

13.9 Sensitivity to noise in the body-surface potentials

In the experiments for detecting maxima, we already saw that noise in the body-surface potentials has a huge impact on the reconstruction quality. This sensitivity to noise is investigated in detail in this section. Again, we use the detailed, eccentric spheres model and applied two maxima to the heart surface. The corresponding body-surface potentials were computed with the forward methods. Then, we added different amounts of noise to the body-surface potentials, before trying to reconstruct the heart-surface potentials again.

As a measure for the amount of noise in a signal, one can use the *signal-to-noise ratio* (SNR). This ratio is defined as the ratio of the power of a signal and the power of the background noise. Usually, ten times the logarithm of this ratio is taken, such that we can express SNR in decibels (dB), and the definition becomes:

$$\text{SNR(dB)} = 10 \log_{10} \left(\frac{P_{\text{signal}}}{P_{\text{noise}}} \right)$$

Equivalently, SNR can be obtained by calculating the square of the amplitude ratio, which in the decibel notations becomes:

$$\text{SNR(dB)} = 20 \log_{10} \left(\frac{A_{\text{signal}}}{A_{\text{noise}}} \right) \quad (13.1)$$

with A the root mean square amplitude. Note that the higher the SNR, the cleaner (and thus better) the signal is. Also note, that this ratio is measured in decibels, a logarithmic scale with base 10: a decrease of SNR with 3dB actually means that twice as much noise is present in the signal.

We applied different quantities of noise to our signal. For this, we used *additive white gaussian noise*, in such an amount that it resulted in a specific signal-to-noise ratio. The results for the corresponding reconstructions are shown in Figure 13.23.

The top row of that figure shows our original, two maxima distribution, and the reconstructions that correspond to a signal-to-noise ratio of 100dB. At this (unrealistically good) noise level, the reconstructions clearly perform very well. When we decrease the SNR, thus making the influence of noise larger and larger, we see that the maxima slowly grow and merge to one maximum. At 50dB, the reconstruction still shows a good match with the original potential distribution. At 43dB, we see that some merging is occurring, and at 35dB, the Tikhonov method is not able to reconstruct two separate maxima anymore. At 23dB, also the GMRes method shows only one maximum. Even lower SNRs only result in larger areas of maximal potentials.

From these results, we can conclude that GMRes is somewhat better than Tikhonov at keeping the maxima separated under the influence of noise. However, both methods are severely influenced by the presence of noise.

13.9.1 Significance of these findings

But what does this mean for our own recordings? The system acquired at Maastricht University has a typical electrode noise of $10\mu\text{V}$ (this figure was obtained in a personal contact with the supplier). The root mean square amplitude, averaged over all electrodes

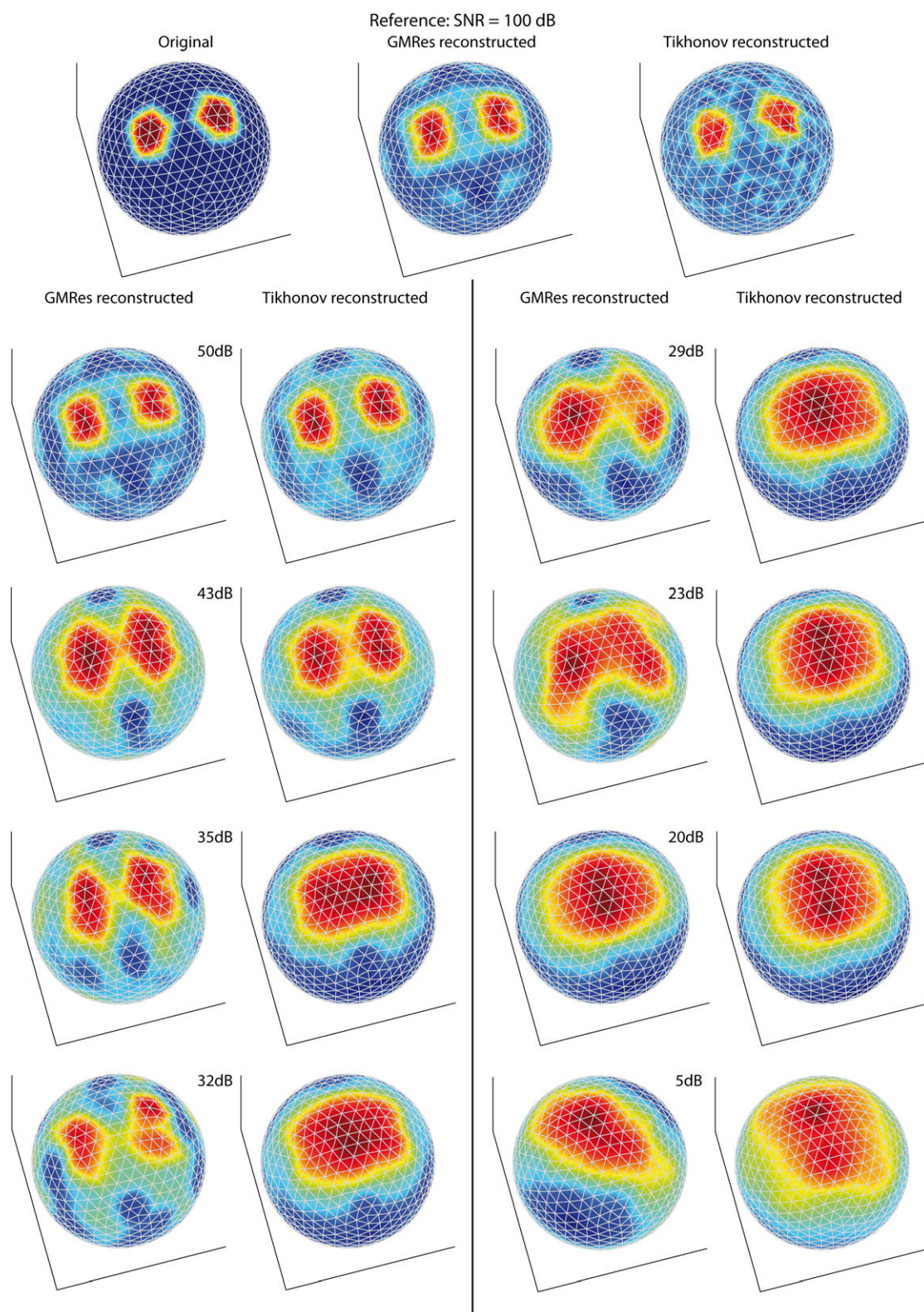


FIGURE 13.23: Results from reconstruction of heart-surface potentials with two maxima, when a certain amount of noise is added to the body-surface potentials. The amount of noise is expressed in a signal-to-noise ratio (SNR) in decibels, shown next to the reconstructions.

in our own recorded signals, is $177\mu\text{V}$. These two quantities give us, according to equation 13.1, an average signal-to-noise ratio of approximately 25dB. As we look at the results of a corresponding noise level of 23dB in Figure 13.23, we see that at this noise level, we are not able to reconstruct two close maxima separately.

However, we should remember that in obtaining this value, we used the root mean square amplitude over the whole signal, also including the parts where not much is happening at the body surface, with an amplitude of essentially zero volts. This pulls our root mean square amplitude down drastically. The QRS complex in our recordings, for example, is a significant increase in the signal amplitude. If we only look at this QRS complex, the root mean square amplitude, averaged over all electrodes in our recordings, is $480\mu\text{V}$. This corresponds to a signal-to-noise ratio of 34dB, at which we can distinctly reconstruct two maxima, at least with the GMRes method, according to Figure 13.23.

This leads us to believe that with the noise present in our signals, we will have a challenge in obtaining good reconstructions; only at the QRS complexes we have a signal amplitude that is strong enough to, in otherwise perfect conditions, reconstruct two close maxima.

13.10 Short summary

Let us shortly summarize these results. We have shown that reconstructions are possible in different models and geometries. Both Tikhonov and GMRes yield similar results; only in the heavy presence of noise, we see that GMRes might have some advantages over Tikhonov, as it seems to smooth the solution less. We should note however, that some of the “difficult” corners in GMRes were selected by hand, which might induce a bias towards the original signal.

We have established a serious doubt in the potentials provided with the ECGsim model for several reasons; therefore, we will not use the results in which these potentials were used in any conclusions. When we use our own forwardly computed potentials in this model, we are able to reconstruct heart-surface potentials nicely.

We furthermore saw that geometrical uncertainty also introduces errors in the reconstructions, especially with translation errors. Size errors seem to matter less. The final experiments established that noise really is an important factor in the quality of the reconstructions. Over the whole signal, with an signal-to-noise ratio of 25dB, we will not be able to yield perfect reconstructions. However, at the most significant part of the signal, the QRS complex, we obtain an signal-to-noise ratio of 34dB, which is a huge improvement and can yield nice reconstructions.

Chapter 14

Reconstructions with our own data

Until now, we have only been using simulated data and simple models. However, the ultimate goal is to reconstruct real human heart-surface potentials from measurements at the body surface. In this chapter, we will describe our efforts to fulfill this goal - or at least to give it a first try.

If we want to reconstruct heart-surface potentials from own data, we need several things:

- The equipment to record body-surface potential data. At the Cardiovascular Research Institute Maastricht (CARIM), the equipment to measure body surface potentials was acquired and put to use. The system allows for 256 simultaneous body-surface potential recordings.
- A human test subject. A male researcher from our department was kind enough to be the subject of our investigations. He went through a procedure in which 256 electrodes were attached to his body (see Figure 14.1), obtaining several minutes of body-surface potential recordings in rest. The test subject was a young, normally proportioned person with no known history of heart disease.
- A geometry representing the test subject's anatomy and the electrode positions.

Due to medical-ethical considerations, it was not yet possible to also obtain a CT scan of the test subject as geometrical reference for our computations. Therefore, we used a data set available from the “Utah torso” project, which was constructed from Magnetic Resonance Images (MRI) by MacLeod and others at the University of Utah [46]. This Utah torso is also a normally proportioned male. We extracted heart and body surface

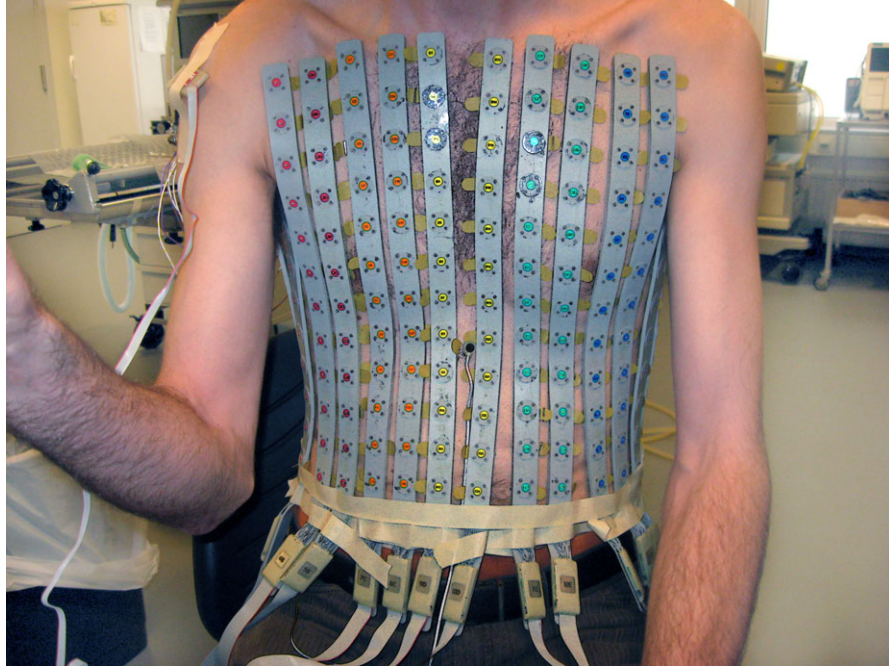


FIGURE 14.1: Our setup for measuring 256 body surface electrograms. Several strips with electrodes are attached to a male test subject and connected to our input devices. Image used with permission of the test subject.

geometry from these data sets and used those as geometrical reference in our calculations, see Figure 14.2. In the end, only 256 vertices of the body surface will be used, corresponding to the locations of the 256 electrodes used at time of measurement.

Also because of medical-ethical and practical reasons, it was not possible to directly measure epicardial potentials. Thus, for this model, we only have body-surface potential data, and no heart-surface potentials are available as a golden standard. The reconstructions of the heart surface potentials can only be assessed as ‘visually normal’ or ‘abnormal’ by a cardiologist and checked against literature findings.

14.1 Generating body surface potential maps

The measured body surface potentials need to be post-processed to obtain useful data. Basic operations involve extraction of the (filtered) potential data, and relating these data to the correct electrodes with a certain position. Software was written to generate Body Surface Potential Maps (BSPMs) from these data, as shown in Figure 14.3. These maps show the distribution of electrical potentials on the body surface. Animations of the changing body surface maps can be made to track temporal changes in cardiac activation. A link to an example animation can be found in Appendix A.

Heart and torso

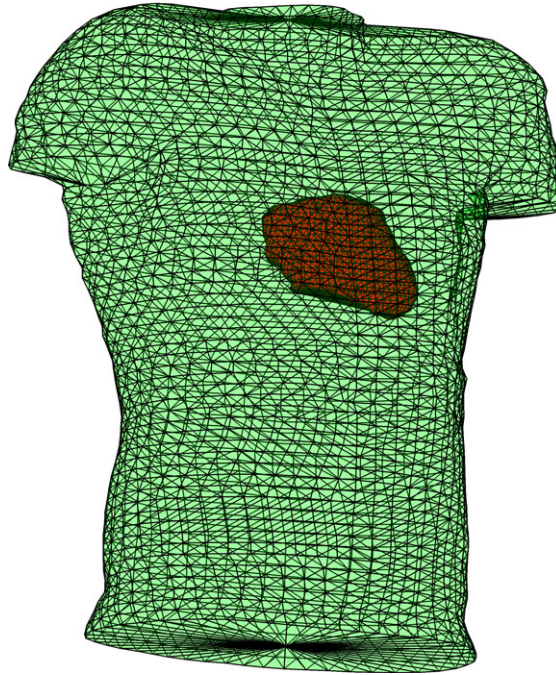


FIGURE 14.2: Realistic heart and body surface geometry as used for reconstructions of our own human measurements.

However, in this view, the electrodes are “unwrapped” on a two-dimensional surface, while in reality, the electrodes are positioned in a three-dimensional space. It would be more realistic if we projected the potential recordings on a torso geometry.

14.2 Tailoring the geometry

Since we were not able to obtain a CT or MRI scan to get an exact anatomical relation between the test subject’s heart, his torso and the electrode positions, we used the already digitized Utah torso and heart. This geometry corresponds to a normally proportioned male. Of course, no exact resemblance can be expected with our test subject, but the digitized torso and our test subject are not that different.

The digitized Utah torso contains 1329 vertices, which makes it a very detailed torso. However, we have recordings at “only” 256 positions. Therefore, we carefully selected the vertices on the Utah torso that correspond to an approximate electrode position in our recordings. In Figure 14.4, the Utah torso is shown, with the electrode positions mapped onto it.

Now we have annotated the electrode positions, this leaves us with 256 vertices, but without any triangulation. To obtain a correct, triangulated surface corresponding to

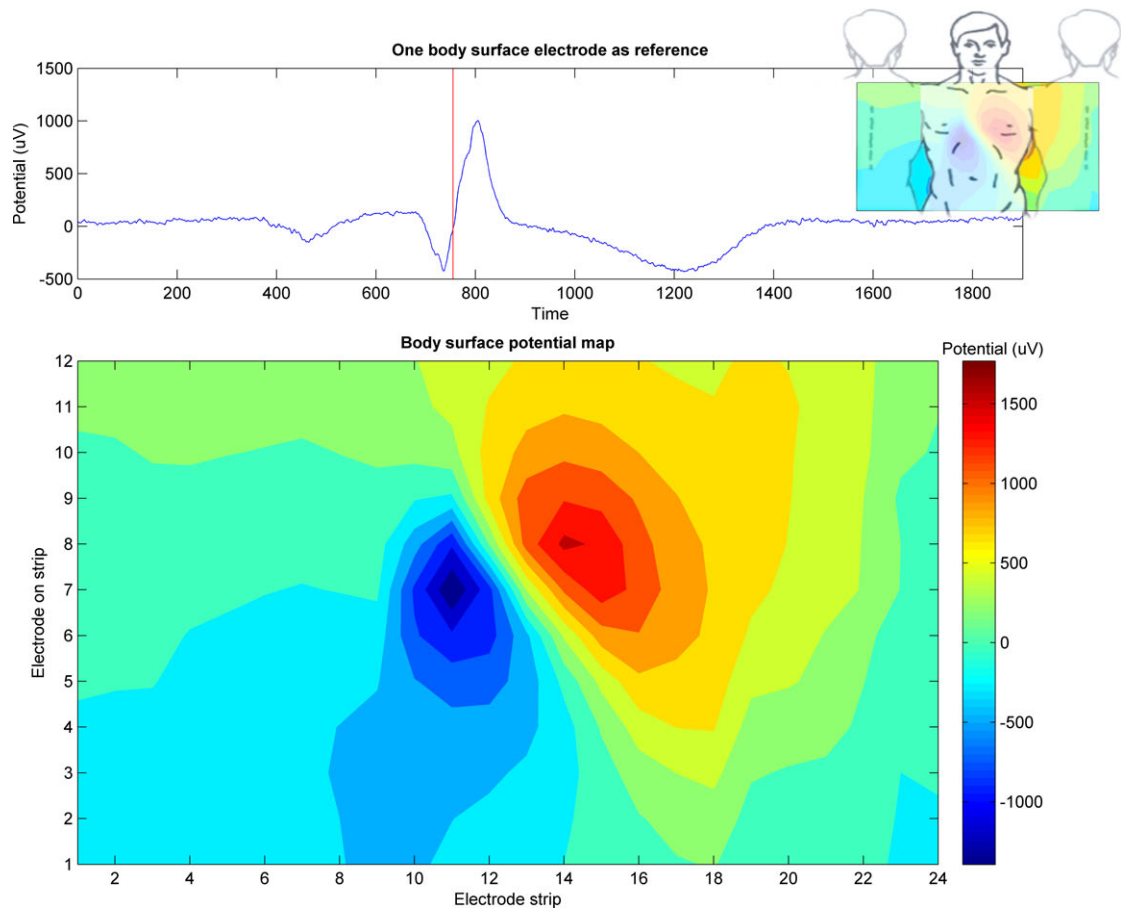


FIGURE 14.3: A body surface map at a certain instant during a heart beat, generated from our body surface potential measurements. The middle of the map represents the front torso, while the left and right side wrap to the back, as indicated by the inset at the right top.

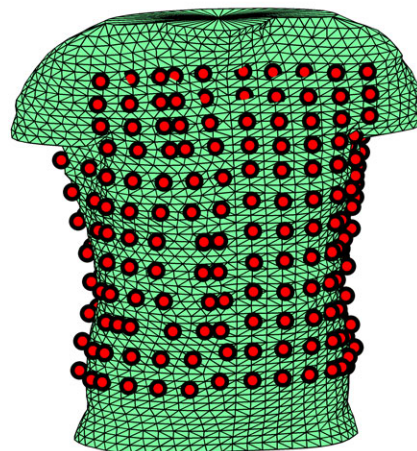
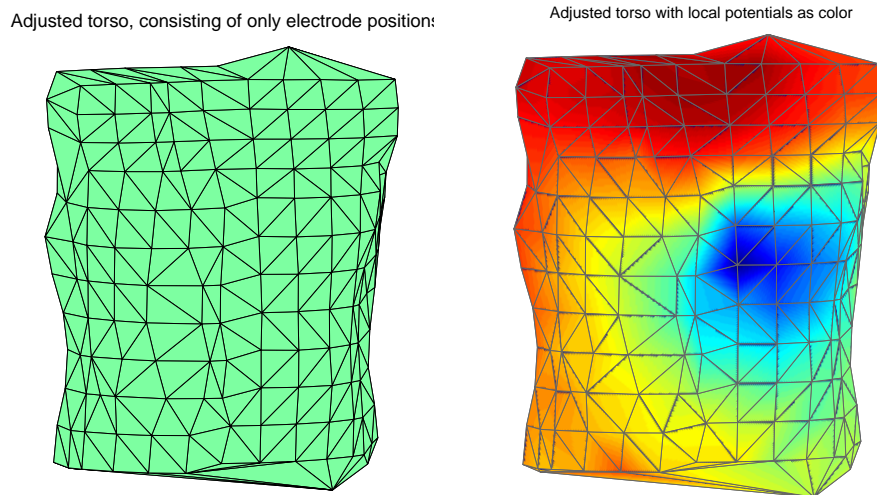


FIGURE 14.4: The Utah torso, with superimposed the vertices that more or less correspond to the electrode positions in our recordings.



(a) Our reconstructed torso, in which each vertex corresponds to an electrode used in our recordings of body-surface potentials. (b) The same torso, but now colored with the corresponding potentials (at a certain time instant).

FIGURE 14.5: Using a tailored geometry for representing the body-surface potentials is more accurate than a body-surface potential map.

these vertices, we performed “surface reconstruction”. We used the same methods as described in chapter 5, obtaining the surface shown in Figure 14.5(a). Now, each vertex corresponds to an electrode, which means that for each vertex we have a corresponding recording of body-surface potential over time.

The next step is to connect the recordings of potentials with the correct vertices. Caution is needed here, as wrong numbering of electrodes or vertex positions might yield a large mismatch in location. If we use colors to represent the potentials at the body-surface, we obtain Figure 14.5(b).

14.3 Reconstruction of heart-surface potentials

At this point, we have all the ingredients needed for reconstructing heart-surface potentials. The tailored Utah torso, combined with the detailed Utah heart, is used to compute a transfer matrix. This is computationally demanding, but fortunately has to be done only once for this geometry.

From our body-surface potential data, we extract one heart beat. At each time instant, we apply the Tikhonov and GMRes regularization techniques to reconstruct the corresponding heart-surface potentials. For several interesting time instants, we have visualized the results in Figures 14.6, 14.7, 14.8 and 14.9 .

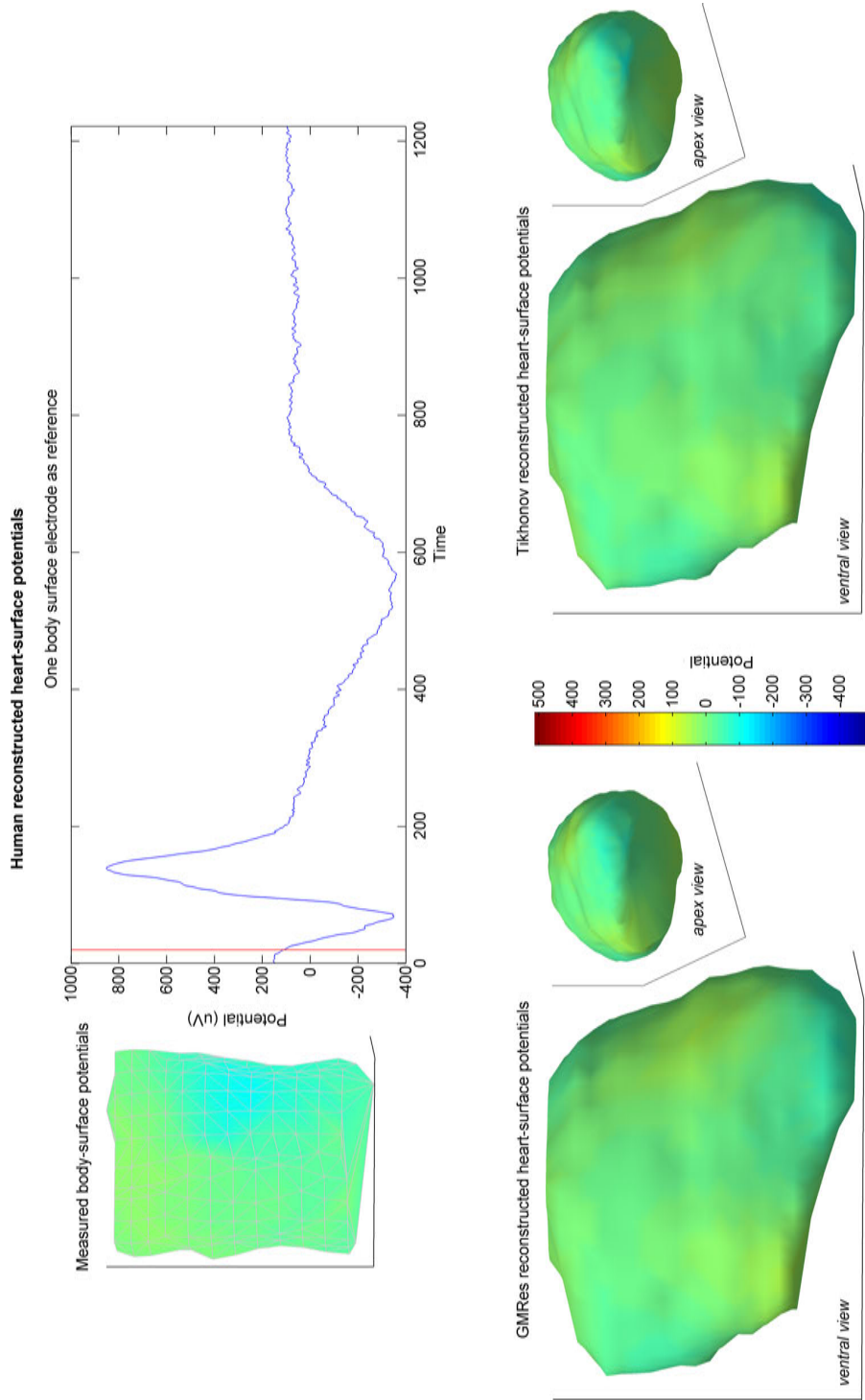


FIGURE 14.6: Reconstructions of heart-surface potentials with our own body-surface data and a tailored geometry. The upper left image shows the body surface with the corresponding potentials, as measured on our test subject. The image at the top right shows a random ECG lead for time reference, in which the current time is indicated by the red line. In this case, the data is taken just before the QRS complex. The images on the bottom show the ventral and apex view of the reconstructed heart-surface potentials, for either the GMRes reconstructions (left) or the Tikhonov reconstructions (right). Obviously, not much is happening at this time instant, as all potentials are approximately zero.

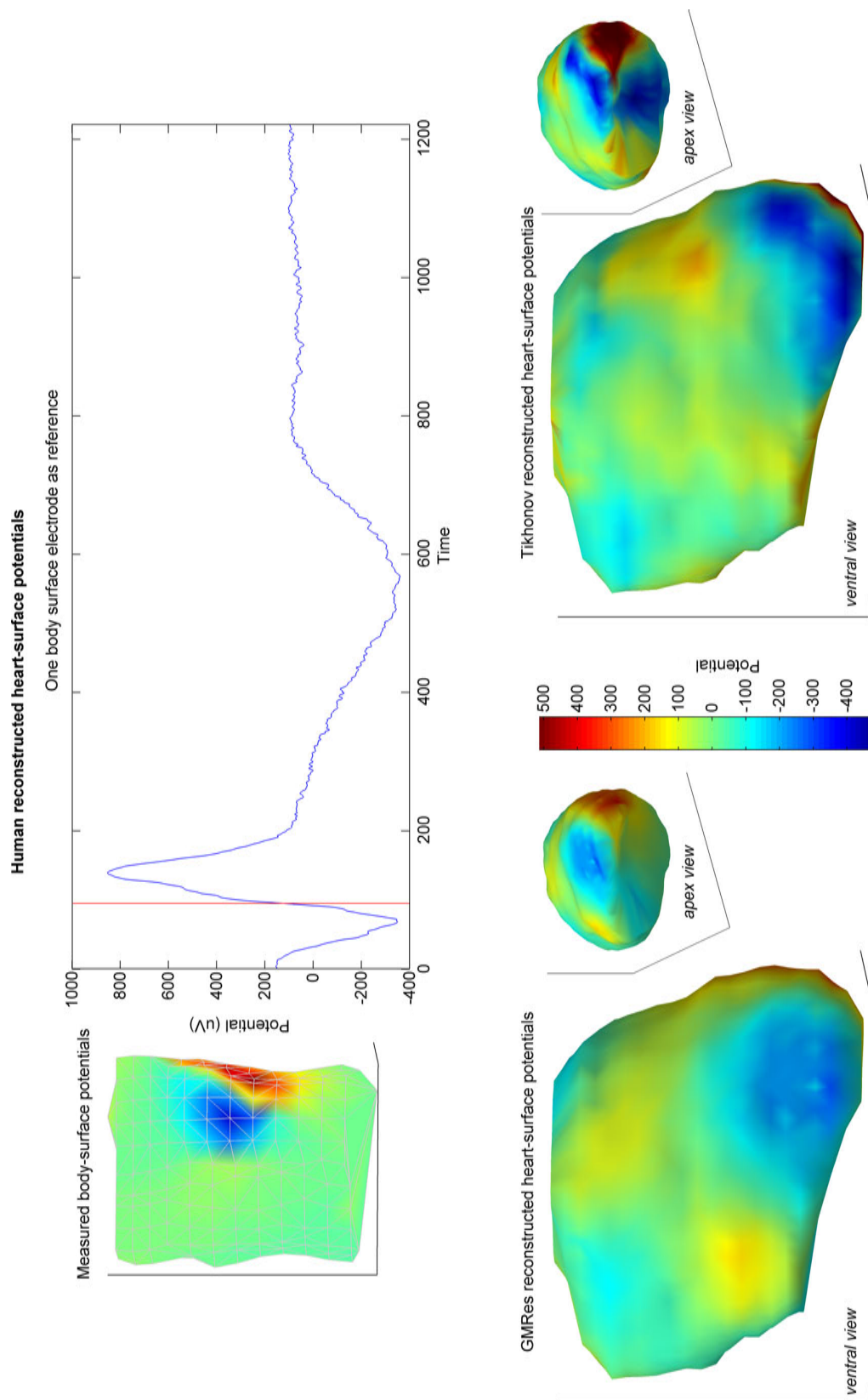


FIGURE 14.7: Same as Figure 14.6, but now for a moment during the upstroke of the R-peak, during which the right ventricle and left ventricle depolarize, shortly after each other.

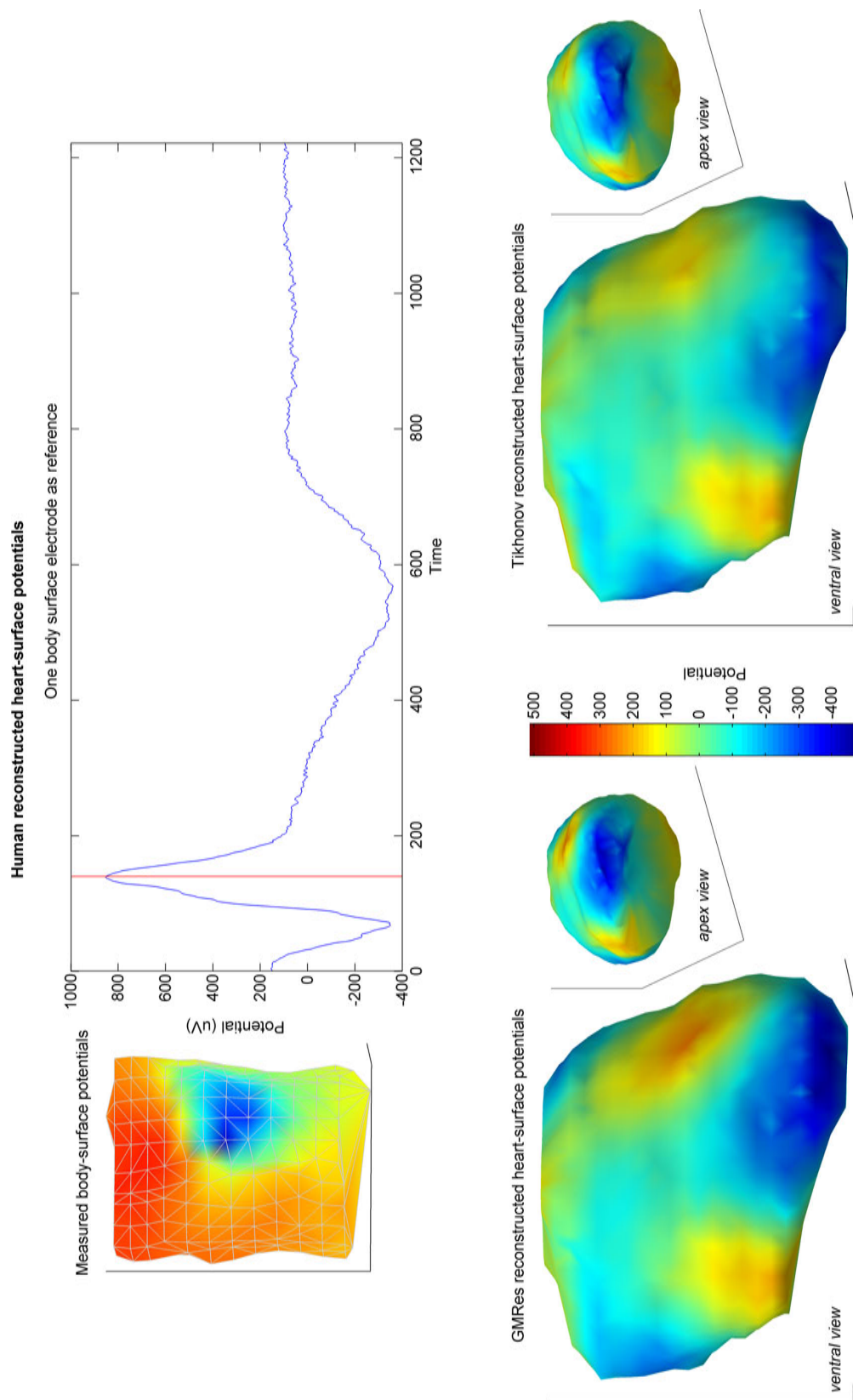


FIGURE 14.8: Heart-surface potential reconstructions at the top of the R-peak.

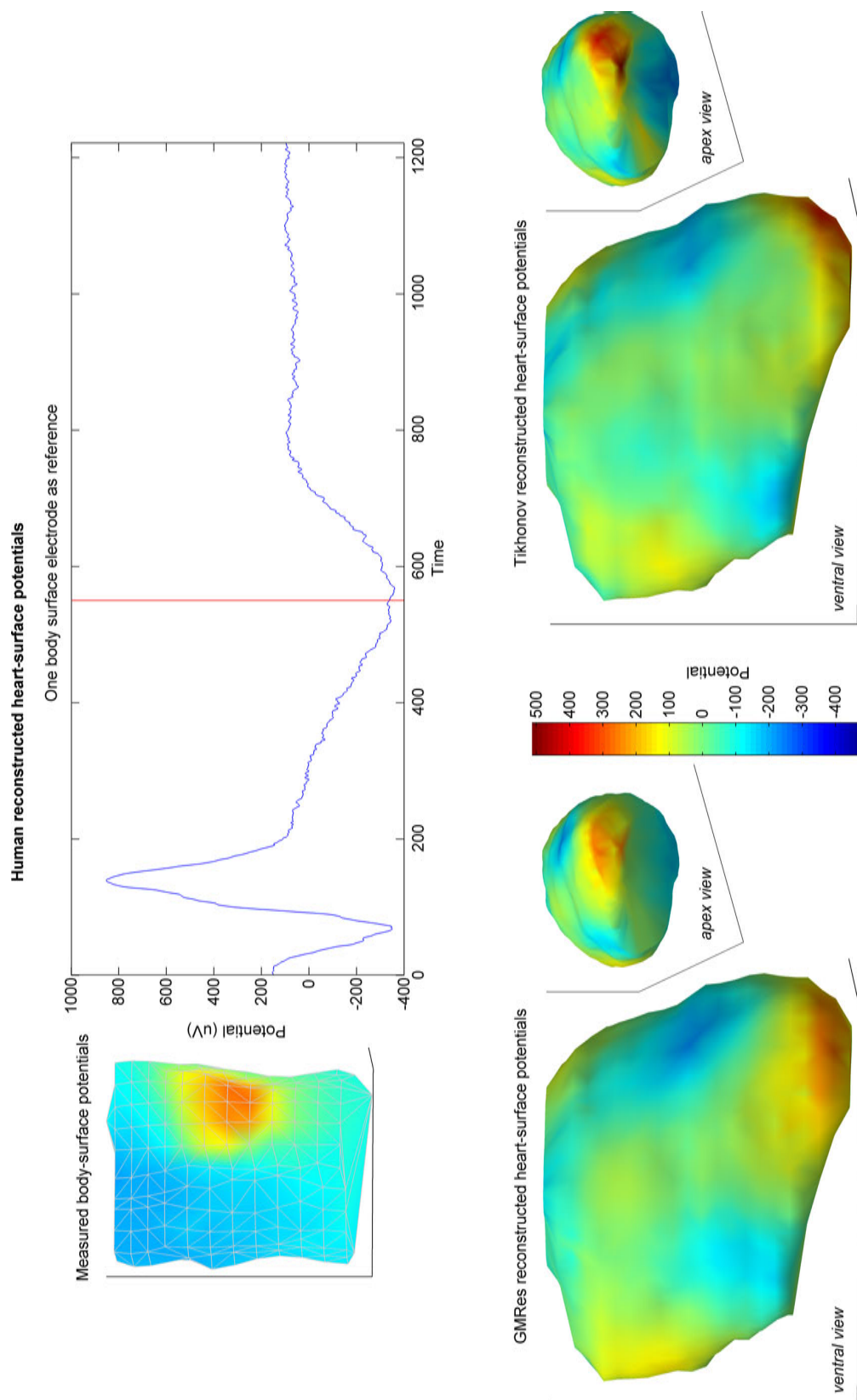


FIGURE 14.9: Reconstructions at the top of the T-peak, corresponding to repolarization of the ventricles. Note that the ECG lead shows a negative T-peak, but this is only due to the location of this (arbitrarily chosen) electrode.

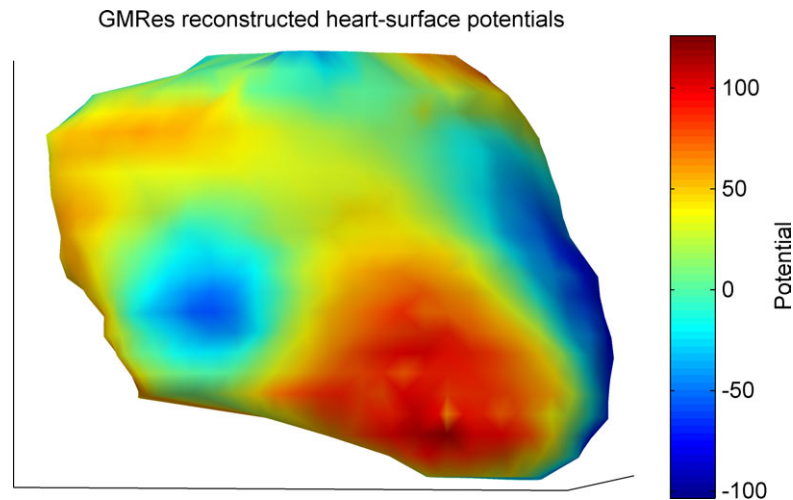


FIGURE 14.10: Reconstruction of heart-surface potentials just before epicardial breakthrough. The positive area reflects the area of breakthrough. Note that the color scale is different from that of the previous figures.

First note, that atrial potentials are too small to reconstruct at this moment and thus are not visible here. That is also the reason that, just before the depolarization of the ventricles (which happens during the QRS complex of an ECG lead), the reconstructed heart-surface potentials are almost zero, as Figure 14.6 shows. At this moment, the atria are depolarized, and the ventricles are still polarized. This means that the heart-surface potentials are very close to zero, as indeed is visible.

The depolarization process of the ventricles has several phases. Depolarization starts at the inner heart wall (the endocardium) and spreads to the outer heart wall (the epicardium). In healthy persons, the first location at which the epicardium gets depolarized, the so called “breakthrough”, is at the right ventricular wall. Subsequently, also the left ventricle depolarizes.

Just before epicardial breakthrough at the right ventricle, the depolarization front is approaching, but has not yet reached, the epicardium. This generates a positive potential region at the epicardium of the right ventricle. GMRes was able to reconstruct this area, as is shown in Figure 14.10. Upon right ventricular breakthrough, this positive region is invaded by a local potential minimum, quickly replacing the previously positive area and changing it in a pronounced negative area. This can be seen in Figure 14.7.

In that figure, we also see a positive area at the left ventricle. This reflects the moment just before left ventricular breakthrough: for the same reasons as on the right ventricle, we first get an area of maximum potential here. Again, at the moment of left ventricular breakthrough, we see that this positive area is replaced by a negative area, shown in Figure 14.8.

However, in that figure, also some areas of maximal potential can be seen, that persist during the depolarization phase. They are not invaded by a minimum, neither is the existing area of negative potential growing over them. We would expect the complete depolarization of the ventricles to be reflected by an area of negative potential completely covering the ventricles. Perhaps at this stage, the influence of noise and geometrical uncertainty is taking over, resulting in some artifacts.

The ventricles are now depolarized, and the next phase is slow repolarization of the ventricles. Repolarization of ventricles is reflected by a T-wave (which on an ECG lead, depending on the location of the reference electrode, can be positive or negative). This repolarization is reflected by a positive area at the anterior surface of the ventricles. However, in our reconstructions, such a positive area was found at the apex, as depicted in Figure 14.9. Furthermore, an area with negative potentials is found at the left ventricle, which has been described previously in humans [47].

14.4 Discussion

The findings as described above show some remarkable resemblances with results from a study performed by Ramanathan and others [47]. Our findings during the QRS complex, with maxima just before breakthrough at first the right ventricle and then the left ventricle, quickly followed by minima during the actual breakthrough, show a nice correspondence to their findings. In other words, although validating our results is not possible, our first results might reflect the actual physiological depolarization of our test subject.

However, during the repolarization phase a pronounced maximum was reconstructed at the apex, whereas Ramanathan et al. found a maximum area at the anterior side of the heart. Also, some areas of positive potential at the right ventricle are reconstructed, that are not subsequently replaced by one large area of negative potential, as we would expect when the ventricles are completely depolarized. These results suggest that the uncertainty factors are preventing an accurate reconstruction. Moreover, the results that do fit the expectations might just be lucky findings, although they are consistent throughout the recordings.

Taking the results of chapter 13 into account, where we performed an extensive analysis of the reconstruction capabilities of our methods, only some distinct resemblance between our reconstructions and the physiological expectations were expected. As we saw in that chapter, at the expected levels of noise and in otherwise perfect conditions, we would only expect some valid results at the QRS complex. However, in the test case

presented in this chapter we also have a significant geometrical uncertainty, because we used a non-specific geometry as reference. Nevertheless, we have found some nice results in our reconstructions, at least during the QRS complex. These findings are a proof-of-concept, indicating that it is possible to reconstruct heart-surface potentials noninvasively, although it should be stressed that the accuracy still has to be validated.

Our previous experiments showed that noise and geometrical uncertainty decrease the resolution of our reconstructions. In better circumstances, with noise-reduction and a more accurate geometry, we would expect the resolution of the reconstructions to increase. A higher detail in our reconstructions might reveal more breakthrough locations (instead of one large smoothed area of breakthrough), as those have been described in human physiological breakthrough previously [47].

For animations of the heart-surface reconstructions during one heart beat, see the links mentioned in Appendix A.

Part IV

Summary and Conclusions

Chapter 15

Summary

As we saw in the introductory chapters, the heart is a pump that heavily depends on electric impulses to function. These electrical waves spread over the heart surface to induce contraction. The results of this electric heart activity reflect to the body surface, where we can record the electric potentials that for example are used in the standard electrocardiogram (ECG).

However, these ECGs lack sensitivity and localized detail. A novel imaging technique called non-invasive electrocardiographic imaging (ECGI) tries to reconstruct from these ECGs the corresponding heart-surface potentials, more specifically, the potentials at the outer heart wall (the epicardium). For this, we need geometrical information, for example obtained by computed tomography (CT). We also need many locations at the body surface where we measure the body-surface potentials. The reconstruction of heart-surface potentials from body-surface potentials is part of a framework that tries to enable the analysis of transmural (that is, “through the heart wall”) potentials in the heart.

Based on physical laws, we derived a method, based on previous work, that enables us to relate heart-surface potentials to body-surface potentials, to solve the so called *forward problem of electrocardiography*. For obtaining body-surface potentials, we need two separate sets of data: geometrical data, relating the anatomy of the heart to the anatomy of the torso; and the heart-surface potentials itself.

The *transfer matrix* is an essential part of the forward problem, as it captures the geometrical data to relate the heart-surface potentials to the body-surface potentials. We derived a simple linear relation between the body-surface potentials and the heart-surface potentials, with the transfer matrix as key part. For various models and data sets, we validated our implementation of this linear relation and its corresponding framework.

We saw a nice correspondence between our forwardly computed body-surface potentials, and the known body-surface potentials, except for some scaling deviation that did not influence the distribution itself.

Unfortunately, we cannot simply invert this linear relation to reconstruct heart-surface potentials from body-surface potentials, to solve the *inverse problem of electrocardiography*. The reason for this is the *ill-posed* nature of the inverse problem, meaning that a small disturbance in the data yields completely different reconstructions. As noise is always present in real-world applications, these small disturbances will surely influence our reconstructions extremely, as we have seen in our experiments.

Therefore, *regularization methods* are needed to gently direct the solutions into a feasible direction. We implemented Tikhonov regularization, that poses a bound on the norm of the solution, preferring low-valued solutions over extremely high-valued solutions. We also used the generalized minimal residual (GMRes) method, iterating over an expanding set of possible solutions until a reasonable solution is found.

Both methods require a regularization parameter: Tikhonov for the weight of the imposed bound, and GMRes as selection of the optimal iteration. For this, we used the L-curve method. This method plots a measure for the ill-posedness versus a measure for the mismatch. Both quantities should be as low as possible, but getting to decrease one typically increases the other. To find an optimal trade-off, we select the corner at which a decrease in one starts to have a large impact on the increase of the other.

We validated this inverse implementation in several data sets and models. Both Tikhonov and GMRes methods produced nice reconstructions under controlled circumstances. We were able to reconstruct two close maxima if not too much noise was present, but also discovered that the amount of noise present in the body-surface potentials is a key factor in determining the quality of reconstruction. Also, when the position of the heart within the torso has an uncertainty factor, this influences the reconstruction considerably. This also holds, although to a lesser extent, for uncertainty in the size of the heart.

In these difficult situations, we discovered that GMRes, by carefully selecting the correct iteration, might be able to provide reconstructions that are somewhat more detailed than Tikhonov reconstructions. In general, however, they often yield the same results, which validates both methods as good regularization methods.

This thesis was ended with the results of our very first reconstructions based on own human data. Body-surface potential maps were measured on a healthy test person. An existing, digitized geometry (not belonging to our test person) was used as reference.

Withstanding the influence of noise and geometrical uncertainty, the reconstructed heart-surface potentials during the depolarization phase of a heart beat showed resemblance with findings described in literature.

Chapter 16

Conclusions

In this thesis, we have reached several milestones. First of all, we established that it is possible to write body-surface potentials in terms of some geometrical transfer matrix and heart-surface potentials. We did so under several assumptions, the most important one being the homogeneous assumption: we assumed a homogeneous torso. However, the method for an inhomogeneous torso, for example including the lungs, bones etcetera, is equivalent [35], and research has shown, that this homogeneous assumption does not influence the results extremely [24]. Nevertheless, it remains a gross assumption.

We validated our forward implementation extensively, establishing that the forwardly-computed body-surface potentials are correctly distributed, but with too high amplitudes. This scaling defect is constant for one geometry, but can differ for different geometries. We found suggestions that this defect is somehow logarithmically related to the distance between the geometrical elements. However, as the distributions showed a perfect fit, and we actually are only interested in distributions and not in absolute amplitudes, we can assume that this scaling defect has no further implications for our research.

In the inverse problem, we established some important facts. First of all, we provided a proof-of-concept: it is possible to reconstruct heart-surface potentials from body-surface potentials. However, we also discovered that this problem is ill-posed and regularization is needed. The Tikhonov and GMRes methods used for regularization yield nice results in low-noise conditions. An essential part of these methods is the automatic parameter selection, used for finding the optimal result. In Tikhonov, the L-curve method sometimes picks the wrong corner, yielding an unregularized solution. This can be corrected manually. The same holds for GMRes: selecting the correct corner position can be tricky with the conditioned L-curve. Manual selection often yields good results, and gives a good insight in the actual functioning of these methods.

On the subject of geometrical uncertainty, we saw that a big error in geometrical assumption yields incorrect reconstructions. However, the reconstructions seem able to deal with only minor uncertainty: a translation of heart position of 10% can be compensated for, and even larger size deviations are allowed. We expect that CT, used as a geometrical basis for reconstruction, yields geometries well within these margins.

On the other hand, we should note that the heart moves considerably during one heart beat. During its contraction phase, it shrinks, wrings and translates, which is not reflected in the static geometry used as basis for the transfer matrix. An approach with a geometry that changes with the actual location and shape of the heart during one beat might provide better results.

Another complicating factor is noise. The influence of noise is enormous. Noise severely reduces the resolution of the reconstruction. We saw that GMRes then shows its strength: it shows less smoothing than Tikhonov, and thereby better reconstruction of the original distribution. The signal-to-noise ratio in our own recordings varies from 25dB (over the whole signal) to 34dB (over only the QRS complex). At these values, and with the results of our experiments, we can only expect some valid reconstructions during the QRS complex of a heart beat. Noise reduction or better regularization of the inverse problem is therefore one of the key elements in our future approach.

Despite these complicating factors, our first reconstructions based on measured human body-surface potentials and a non-specific geometry show some unexpected similarity with findings described in literature, at least during the depolarization phase of the ventricles. However, extensive validation of these human reconstructions is necessary to be able to make solid conclusions based on future findings.

Combining all these results, we can conclude that it is possible to reconstruct human heart-surface potentials non-invasively when we make some relevant assumptions.

Chapter 17

Further discussion and future work

As the conclusion already pointed at, we still have enough to do. One of the first next steps should be the definite removal of the scaling defect. It has annoyed us for long enough now, and surely, we are much closer to its origin than ever.

Another step would be to implement other methods for reference. For example, Stenroos [35] and Horacek [29] have slightly different approaches that have some advantages; either computational (Horacek) or in accuracy by using a piece-wise homogeneous approach (Stenroos).

Then, one of the most important future goals would be to decrease the influence of noise in our reconstructions. Two paths can be followed here: either we reduce the noise level in our recordings, or we improve the regularization methods even further. Probably a combination of both paths is necessary.

For reducing the noise level, for example, we could use high resolution electrocardiography, in which noise is reduced by applying signal averaging methods [48] or filtering techniques [49]. Also, we could try using a wavelet approach. Some previous studies have shown nice results for ECGs [50], but none have been used in the inverse problem of electrocardiography as far as we know.

Other regularization techniques could also be pursued. For example, an approach by Greensite [51] is shown at least theoretically to be less influenced by noisy components. Furthermore, a regularization technique that not only regularizes in the spatial domain, but also in the temporal domain, might yield more stable solutions [52].

But before looking at other regularization techniques, we might try to apply some variants of Tikhonov regularization. In our experiments, we applied Tikhonov Zero Order regularization, imposing a bound on the absolute value of the potentials. However, with Tikhonov First Order or Second Order regularization, where we apply a bound on the spatial derivative or second spatial derivative, respectively, we might obtain better results, as suggested by Throne [41] and others.

Also, we could try to not regularize the potentials directly, but instead use a bound on the current density. A study by Khoury [53] has shown significant improvement with this approach. This is just a slight modification to our Tikhonov approach and worth investigating.

Until now, in Tikhonov regularization, we used the (euclidian) L2-norm of the potentials or its derivatives. In another approach by Ghosh [54], the L1-norm is used to prevent smoothing of the solution. They show that the L1-norm is more accurate than the L2 norm, which also in our case might reduce the influence of noise further.

All previously mentioned methods and approaches apply their own constraints to the data. It might be useful to combine these constraints, to obtain optimal results. Combining these constraints yields a set of admissible solutions, and has been suggested previously [55].

In other words, we cannot avoid the conclusion that, although we still have a long way to go before we obtain clinically relevant reconstructions, a lot of methods are just waiting to be applied to improve our results to a useful level.

Appendix A

Data

The animation showing the body-surface potential maps (BSPMs) during one heart beat, reconstructed from our own measurements, can be found at the following link:

<http://matthijs.cluitmans.net/academic/media/short.avi>

Animations showing the reconstructions of heart-surface potentials during a heart beat can be found here:

<http://matthijs.cluitmans.net/academic/media/reconstrHDventral.avi>

<http://matthijs.cluitmans.net/academic/media/reconstrHDapex.avi>

Bibliography

- [1] David. Bodanis. *Electric universe : the shocking true story of electricity / David Bodanis*. Crown Publishers, New York :, 1st ed. edition, —2005—.
- [2] R. P. Feynman, R. B. Leighton, and M. Sands. *The Feynman Lectures on Physics*, volume 2. Addison-Wesley, Reading, MA, —1964—.
- [3] P. Brugada and J. Brugada. Right bundle branch block, persistent st segment elevation and sudden cardiac death: a distinct clinical and electrocardiographic syndrome. a multicenter report. *J Am Coll Cardiol*, 20(6):1391–6, —1992—.
- [4] Marketa Bebarova, Tom O’Hara, Jan L. M. C. Geelen, Roselie J. Jongbloed, Carl Timmermans, Yvonne H. Arens, Luz-Maria Rodriguez, Yoram Rudy, and Paul G. A. Volders. Subepicardial phase 0 block and discontinuous transmural conduction underlie right precordial st-segment elevation by a scn5a loss-of-function mutation. *Am J Physiol Heart Circ Physiol*, 295(1):H48–58, —2008—.
- [5] L. Harris, E. Downar, L. Mickleborough, N. Shaikh, and I. Parson. Activation sequence of ventricular tachycardia: endocardial and epicardial mapping studies in the human ventricle. *J Am Coll Cardiol*, 10(5):1040–7, —1987—.
- [6] W. Kaltenbrunner, R. Cardinal, M. Dubuc, M. Shenasa, R. Nadeau, G. Tremblay, M. Vermeulen, P. Savard, and P. L. Page. Epicardial and endocardial mapping of ventricular tachycardia in patients with myocardial infarction. is the origin of the tachycardia always subendocardially localized? *Circulation*, 84(3):1058–1071, —1991—.
- [7] Heather Joanne Shannon, Cesar O. Navarro, Bernie A. Smith, Anthony J. McClelland, Ernest W. Lau, Michael J. D. Roberts, John M. C. Anderson, and Jeninifer A. Adgey. Activation patterns during selective pacing of the left ventricle can be characterized using noninvasive electrocardiographic imaging. *Journal of Electrocardiology*, 40(6, Supplement 1):S111–S117, —2007—.

- [8] L. Gepstein, G. Hayam, and S. A. Ben-Haim. A novel method for nonfluoroscopic catheter-based electroanatomical mapping of the heart. *in vitro* and *in vivo* accuracy results. *Circulation*, 95(6):1611–22, —1997—.
- [9] Biosense Webster. A step by step tutorial for epicardial segmentation using cartomerge software module, —2007—.
- [10] C. Ramanathan, R. N. Ghanem, P. Jia, K. Ryu, and Y. Rudy. Noninvasive electrocardiographic imaging for cardiac electrophysiology and arrhythmia. *Nat Med*, 10(4):422–8, —2004—.
- [11] H. Muller. Surface reconstruction - an introduction. In *Scientific Visualization Conference, 1997*, pages 239–239, —1997—.
- [12] N. Amenta, S. Choi, T. K. Dey, and N. Leekha. A simple algorithm for homeomorphic surface reconstruction, —2000—.
- [13] Tamal Dey and Jian Sun. Normal and feature approximations from noisy point clouds. In *FSTTCS 2006: Foundations of Software Technology and Theoretical Computer Science*, pages 21–32. —2006—.
- [14] Tamal K. Dey and Samrat Goswami. Tight cocone: a water-tight surface reconstructor, —2003—.
- [15] Tamal K. Dey and Jian Sun. An adaptive mls surface for reconstruction with guarantees, —2005—.
- [16] P. Kuklik, L. Szumowski, J. J. Zebrowski, and F. Walczak. The reconstruction, from a set of points, and analysis of the interior surface of the heart chamber. *Physiological Measurement*, 25(3):617–627, —2004—.
- [17] Z. J. Malchano, P. Neuzil, R. C. Cury, G. Holmvang, J. Weichet, E. J. Schmidt, J. N. Ruskin, and V. Y. Reddy. Integration of cardiac ct/mr imaging with three-dimensional electroanatomical mapping to guide catheter manipulation in the left atrium: implications for catheter ablation of atrial fibrillation. *J Cardiovasc Electrophysiol*, 17(11):1221–9, —2006—.
- [18] R. N. Ghanem. Noninvasive electrocardiographic imaging of arrhythmogenesis: insights from modeling and human studies. *J Electrocardiol*, 40(6 Suppl):S169–73, —2007—.
- [19] M.J.M. Cluitmans. Electrocardiographic imaging as a medical tool: The mathematical basis and medical implications of electrocardiographic imaging., —2007—.

- [20] R. N. Ghanem, P. Jia, C. Ramanathan, K. Ryu, A. Markowitz, and Y. Rudy. Non-invasive electrocardiographic imaging (ecgi): comparison to intraoperative mapping in patients. *Heart Rhythm*, 2(4):339–54, —2005—.
- [21] Howard S. Oster, Bruno Taccardi, Robert L. Lux, Philip R. Ershler, and Yoram Rudy. Electrocardiographic imaging : Noninvasive characterization of intramural myocardial activation from inverse-reconstructed epicardial potentials and electrograms. *Circulation*, 97(15):1496–1507, —1998—.
- [22] A. Intini, R. N. Goldstein, P. Jia, C. Ramanathan, K. Ryu, B. Giannattasio, R. Gilkeson, B. S. Stambler, P. Brugada, W. G. Stevenson, Y. Rudy, and A. L. Waldo. Electrocardiographic imaging (ecgi), a novel diagnostic modality used for mapping of focal left ventricular tachycardia in a young athlete. *Heart Rhythm*, 2(11):1250–2, —2005—.
- [23] R. S. MacLeod and D. H. Brooks. Recent progress in inverse problems in electrocardiology. *IEEE Eng Med Biol Mag*, 17(1):73–83, —1998—.
- [24] CHARULATHA RAMANATHAN and YORAM RUDY. Electrocardiographic imaging: Ii. effect of torso inhomogeneities on noninvasive reconstruction of epicardial potentials, electrograms, and isochrones. *Journal of Cardiovascular Electrophysiology*, 12(2):241–252, —2001—.
- [25] Y. Rudy and B. J. Messinger-Rapport. The inverse problem in electrocardiography: solutions in terms of epicardial potentials. *Crit Rev Biomed Eng*, 16(3):215–68, —1988—.
- [26] G. T. Lines, M. L. Buist, P. Grottum, A. J. Pullan, J. Sundnes, and A. Tveito. Mathematical models and numerical methods for the forward problem in cardiac electrophysiology. *Computing and Visualization in Science*, 5(4):215–239, —2003—.
- [27] Robert Plonsey and Roger C. Barr. *Bioelectricity: a quantitative approach*. Kluwer Academic/Plenum Publishers, New York, 2 edition, —2000—.
- [28] David Geselowitz and W. Miller. A bidomain model for anisotropic cardiac muscle. *Annals of Biomedical Engineering*, 11(3):191–206, —1983—.
- [29] B. M. Horacek and J. C. Clements. The inverse problem of electrocardiography: a solution in terms of single- and double-layer sources of the epicardial surface. *Math Biosci*, 144(2):119–54, —1997—.
- [30] R. C. Barr, 3rd Ramsey, M., and M. S. Spach. Relating epicardial to body surface potential distributions by means of transfer coefficients based on geometry measurements. *IEEE Trans Biomed Eng*, 24(1):1–11, —1977—.

-
- [31] H. S. Oster and Y. Rudy. Regional regularization of the electrocardiographic inverse problem: a model study using spherical geometry. *IEEE Trans Biomed Eng*, 44(2):188–99, —1997—.
- [32] A. van Oosterom and T. F. Oostendorp. Ecgsm: an interactive tool for studying the genesis of qrst waveforms. *Heart*, 90(2):165–8, —2004—.
- [33] A. van Oosterom and J. Strackee. The solid angle of a plane triangle. *IEEE Trans Biomed Eng*, 30(2):125–6, —1983—.
- [34] M. Stenroos and J. Haueisen. Boundary element computations in the forward and inverse problems of electrocardiography: comparison of collocation and galerkin weightings. *IEEE Trans Biomed Eng*, 55(9):2124–33, —2008—.
- [35] M. Stenroos. The transfer matrix for epicardial potential in a piece-wise homogeneous thorax model: the boundary element formulation. *Phys Med Biol*, 54(18):5443–55, —2009—.
- [36] Mario Bertero and Patrizia Boccacci. *Introduction to Inverse Problems in Imaging*. CRC Press, —1998—.
- [37] Richard O. Martin and Theo C. Pilkington. Unconstrained inverse electrocardiography: Epicardial potentials. *Biomedical Engineering, IEEE Transactions on*, BME-19(4):276–285, —1972—.
- [38] C. Ramanathan, P. Jia, R. Ghanem, D. Calvetti, and Y. Rudy. Noninvasive electrocardiographic imaging (ecgi): application of the generalized minimal residual (gmres) method. *Ann Biomed Eng*, 31(8):981–94, —2003—.
- [39] H. S. Oster and Y. Rudy. The use of temporal information in the regularization of the inverse problem of electrocardiography. *IEEE Trans Biomed Eng*, 39(1):65–75, —1992—.
- [40] P. C. Hansen. The l-curve and its use in the numerical treatment of inverse problems, —2000—.
- [41] R. D. Throne and L. G. Olson. A comparison of spatial regularization with zero and first order tikhonov regularization for the inverse problem of electrocardiography. In *Computers in Cardiology 2000*, pages 493–496, —2000—.
- [42] D. Calvetti, B. Lewis, and L. Reichel. Gmres-type methods for inconsistent systems. *Linear Algebra and its Applications*, 316(1-3):157–169, —2000—.
- [43] Youcef Saad and Martin H. Schultz. Gmres: A generalized minimal residual algorithm for solving nonsymmetric linear systems. *SIAM Journal on Scientific and Statistical Computing*, 7(3):856–869, —1986—.

- [44] Per Christian Hansen, Toke Koldborg Jensen, and Giuseppe Rodriguez. An adaptive pruning algorithm for the discrete l-curve criterion. *Journal of Computational and Applied Mathematics*, 198(2):483–492, —2007—.
- [45] Per Hansen. Regularization tools version 4.0 for matlab 7.3. *Numerical Algorithms*, 46(2):189–194, —2007—.
- [46] R. S. MacLeod, C.R. Johnson, and P.R. Ershler. Construction of an inhomogeneous model of the human torso for use in computational electrocardiography. In *IEEE Engineering in Medicine and Biology Society 13th Annual International Conference*, pages 688–689. IEEE Press, —1991—.
- [47] C. Ramanathan, P. Jia, R. Ghanem, K. Ryu, and Y. Rudy. Activation and repolarization of the normal human heart under complete physiological conditions. *Proc Natl Acad Sci U S A*, 103(16):6309–14, —2006—.
- [48] EDWARD J. BERBARI, RALPH LAZZARA, PHILIP SAMET, and BENJAMIN J. SCHERLAG. Noninvasive technique for detection of electrical activity during the p-r segment. *Circulation*, 48(5):1005–1013, —1973—.
- [49] Mihai Popescu, Paul Cristea, and Anastasios Bezerianos. Multiresolutional distributed filtering: A novel technique that reduces the amount of data required in high resolution electrocardiography. *Future Generation Computer Systems*, 15(2):195–209, —1999—.
- [50] Donghui Zhang. *Wavelet Approach for ECG Baseline Wander Correction and Noise Reduction*, volume 2. —2005—.
- [51] F. Greensite and G. Huiskamp. An improved method for estimating epicardial potentials from the body surface. *Biomedical Engineering, IEEE Transactions on*, 45(1):98–104, —1998—.
- [52] B. Messnarz, B. Tilg, R. Modre, G. Fischer, and F. Hanser. A new spatiotemporal regularization approach for reconstruction of cardiac transmembrane potential patterns. *Biomedical Engineering, IEEE Transactions on*, 51(2):273–281, —2004—.
- [53] D. S. Khoury. Use of current density in the regularization of the inverse problem of electrocardiography. In *Engineering in Medicine and Biology Society, 1994. Engineering Advances: New Opportunities for Biomedical Engineers. Proceedings of the 16th Annual International Conference of the IEEE*, pages 133–134 vol.1, —1994—.
- [54] Subham Ghosh and Yoram Rudy. Application of l1-norm regularization to epicardial potential solution of the inverse electrocardiography problem. *Annals of Biomedical Engineering*, 37(5):902–912, —2009—.

-
- [55] Ghandi F. Ahmad, Dana H. Brooks, and Robert S. MacLeod. An admissible solution approach to inverse electrocardiography. *Annals of Biomedical Engineering*, 26(2):278–292, —1998—.